Synthesis, Characterization, and Optimization of Superconductor-Dielectric Interfaces

by

Cameron Kopas

A Dissertation Presented in Partial Fulfillment
of the Requirements for the Degree
Doctor of Philosophy

Approved April 2020 by the
Graduate Supervisory Committee:

Nathan Newman, Chair
Terry Alford
Ray Carpenter
Peter Williams

ARIZONA STATE UNIVERSITY
May 2020

ABSTRACT

The chemical, structural, and electrical properties of niobium-silicon, niobium-germanium, and YBCO-dielectric interfaces are characterized. Reduction in the concentration of interfacial defects in these structures can improve the performance of (i) many devices including low-loss coplanar, microstrip, and stripline microwave resonators used in next-generation cryogenic communication, sensor, and quantum information technologies and (ii) layers used in device isolation, inter-wiring dielectrics, and passivation in microwave and Josephson junction circuit fabrication.

Methods were developed to synthesize amorphous-Ge (*a*-Ge) and homoepitaxial-Si dielectric thin-films with loss tangents of $1–2\times10^{-6}$ and $0.6–2\times10^{-5}$ at near single-photon powers and sub-Kelvin temperatures (≈40 mK), making them potentially a better choice over undoped silicon and sapphire substrates used in quantum devices.

The Nb/Ge interface has 20 nm of chemical intermixing, which is reduced by a factor of four using 10 nm Ta diffusion layers. Niobium coplanar resonators using this structure exhibit reduced microwave losses.

The nature and concentration of defects near Nb-Si interfaces prepared with commonly-used Si surface treatments were characterized. All samples have H, C, O, F, and Cl in the Si within 50 nm of the interface, and electrically active defects with activation energies of 0.147, 0.194, 0.247, 0.339, and 0.556 eV above the valence band maximum (E_{vbm}), with concentrations dominated by a hole trap at E_{vbm}+0.556 eV (presumably Nb_{Si}). The optimum surface treatment is an HF etch followed by an in-situ

100 eV Ar ion mill. RCA etches, and higher energy ion milling processes increase the concentration of electrically active defects.

A thin $SrTiO_3$ buffer layer used in $YBa_2Cu_3O_{7-\delta}$ superconductor/high-performance $Ba(Zn_{1/3}Ta_{2/3})O_3$ and $Ba(Cd_{1/3}Ta_{2/3})O_3$ microwave dielectric trilayers improves the structural quality of the layers and results in 90 K superconductor critical temperatures. This advance enables the production of more compact high-temperature superconductor capacitors, inductors, and microwave microstrip and stripline devices.

ACKNOWLEDGMENTS

Thank you to my friends and family for their support, and to my cats for helping keep this dissertation succinct by deleting almost as many words as were typed. My sincerest gratitude to my advisor, Professor Nathan Newman, for his guidance and continued support through my studies. Thank you for your help over the years and for providing me with the opportunity to learn and develop my scientific skills in such a broadly capable laboratory environment and for encouraging constant improvement. Additional thanks to Dr. Daniel Queen and committee members Professor Alford, Professor Carpenter, and Professor Williams.

I would also like to acknowledge collaborators and lab-mates Dr. Lei Yu, Dr. Shengke Zhang, Professor Rakesh Singh, Ximo Chu, Kaiwen Zhang, Justin Gonzales, Madhu Krishna Murthy, Siddhesh Gajare, Chris Gregory, and Bryan Ibarra Mercado, as well as former high-school interns from the SCENE program, Joseph Park, and Praveen Balaji.

Thank you to Professor Ray Carpenter for guidance and collaboration on transmission electron microscopy work, which was performed with the assistance of the LeRoy Eyring Center for Solid State Sciences and Dr. Shery Chang.

TABLE OF CONTENTS

LIST OF TABLES

TABLE Page

LIST OF FIGURES

FIGURE Page

FIGURE Page

CHAPTER 1

INTRODUCTION

1.1 Background

Superconducting resonators are found in a number of low-temperature high-performance devices, including microwave kinetic inductance detectors, single-photon energy resolving photon detectors, and parametric amplifiers used in quantum sensing, quantum information, and quantum computers. These devices can operate efficiently down to single-photon power levels.

While resonator devices are optimized to minimize geometric, radiation, and coupling losses [1] and are fabricated with high-quality materials, the performance of these devices is often limited by microwave loss and noise in the dielectric. Loss and noise are typically dependent on thermally-activated processes expected to be inconsequentially small at mK temperatures [2]. However, at near-single-photon powers and low temperatures (i.e., <1 K), additional losses arise that degrade performance, an effect first observed in anomalous low-temperature heat capacity of amorphous glasses [3][4]. These anomalous power-and-temperature-dependent losses are labeled “Two-Level Systems” (TLS).

In superconducting coplanar waveguide resonators, researchers find that the choice of materials and the fabrication methods play an important role in TLS losses[5][6][7][1][8]. Considerable variations in loss between devices with the same resonator configuration and dimensions, but made with different fabrication methods, suggest that the Q of the device is limited by extrinsic defect mechanisms. Furthermore, experiments coupled with electromagnetic simulations of resonator devices have led

researchers to conclude that the TLS are concentrated at metal-air, metal-dielectric, and the dielectric-air interfaces [9][10].

This work focuses on characterizing Nb-dielectric interfaces, and their influence on the properties of microwave resonators. Niobium-dielectric structures are fabricated with varying chemical and ion beam surface cleaning methods, followed by the deposition of dielectric and superconductor layers. Controlling fabrication and advanced solid-state methods to characterize the interfaces will identify the chemical species, concentration, and physical character of the defects present at those interfaces.

1.2 Microwave Device Performance: Quality and Loss

The performance of microwave devices is dependent on the quality factor (Q) of the resonators in the devices. The quality factor, Q, of a microwave device is defined as:

$$Q \approx 2\pi \frac{energy\ stored\ per\ cycle}{average\ energy\ dissipated\ per\ cycle} \quad (1)$$

The Q sets a limit on device performance since it is inversely proportional to the time constant of the rate that the resonator's stored energy is lost. The sources of microwave loss include coupling and radiation, conduction losses, and dielectric losses. The device Q is determined with the following relation.

$$\frac{1}{Q} = \frac{1}{Q_{dielectric}} + \frac{1}{Q_{Coupling}} + \frac{1}{Q_{conduction}} + \frac{1}{Q_{radiation}} \quad (2)$$

External losses such as coupling and radiation loss are well understood and can be optimized through the proper design of the coupling impedance, the geometry of the device, and the experimental setup. Conduction loss is managed through materials selection; by choosing a dielectric with minimal electronic carriers [11], a highly-conductive low surface resistance metal such as gold or, better yet, a superconductor.

The dielectric loss is the sum of intrinsic and extrinsic losses [12]. Intrinsic losses are those associated with an ideal crystal structure and originate from anharmonic phonon absorption [13]. Extrinsic dielectric losses arise from the motion of electrons or atoms within the lattice or from spin excitations—all of which are defect-related [14][12].

The dielectric loss tangent can be determined using the following equation,

$$tan\delta = \frac{\omega\epsilon'' + \sigma}{\omega\epsilon'} \tag{3}$$

where ω is the frequency, σ is the dielectric conduction loss, and ϵ‘ and ϵ“ are the real and imaginary parts of the dielectric constant, $\tan\delta = \epsilon''/\epsilon'$.

Since high-performance dielectric devices are designed to minimize losses from all other mechanisms, so that dielectric loss dominates, the following formula applies:

$$\tan\delta = \frac{1}{Q_{dielectric}} \approx \frac{1}{Q} \tag{4}$$

1.3 Defects in Silicon

The semiconductor community has extensively studied defects in silicon, and in general, their electronic and structural energetic properties are well understood down to the meV range. Crystalline defects are categorized as extended (i.e. stacking faults, dislocations, and grain boundaries) or point defects (i.e. interstitials, substitutional defects, or anti-sites). When resonators are fabricated on high-quality single-crystal substrates such as silicon and germanium, the concentration of extended defects is negligible; however, some point defects will be present due to contamination and those generated during synthesis and processing.

The nature of and activation energies associated with intrinsic defects in silicon have been studied by Watkins et al. [15][16][17][18][19], often using electron or

α-particle irradiation to induce point defects in nearly defect-free material. These intrinsic defects in Si take on several forms within the lattice. Silicon vacancies (V_{Si}) exist with charge states $V^{--}, V^{-}, V^{0}, V^{+}$, and V^{++} and anneal out at temperatures near 200 K [18]. Above the annealing temperature, the vacancies often recombine with an interstitial atom or form vacancy clusters such as the divacancy, 3-vacancy, and 4-vacancy, or clusters with impurity atoms. These vacancy-impurity clusters include the A-center (a $V_{Si} \cdot O_{Si}$ pair) [15], and the E-center (a $V_{Si} \cdot P_{Si}$ pair)[20]. Additional defects include the Si interstitial, which often captures and forms clusters with other impurity interstitials such as H, B, C, and Al[16].

The electronic energy levels on the order of 0.01–0.1 eV are far too large to be the source of TLS losses, since thermal energies at 50 mK ≈ 4×10^{-6} eV, and a 10 GHz microwave of ≈4×10^{-5} eV. However, the small energy absorption associated with TLS may be associated with small structural rearrangements of atoms [21], or movement between energetically close defect levels. These possibly are caused by tunneling assisted by a microwave, as is observed with hydrogen TLS in glasses and metals[3] [22]. Further evidence for the association with hydrogen comes from Martinis' [7] investigation of loss in CPW, which found that hydrogenated materials at low temperatures generally contain increased TLS losses. It follows that a more general study characterizing and identifying several different native and impurity defects in high-quality material, such as pure Si and Ge, will be useful.

While defect levels created by many dopant and contaminant atoms in silicon and other common semiconductors have been extensively studied, there are only a few studies [23] [24][25], on electronically active point and extended defects on Nb in, particularly at or near the Nb/Si interface. This omission is particularly surprising considering niobium's prevalence in superconducting electronic devices.

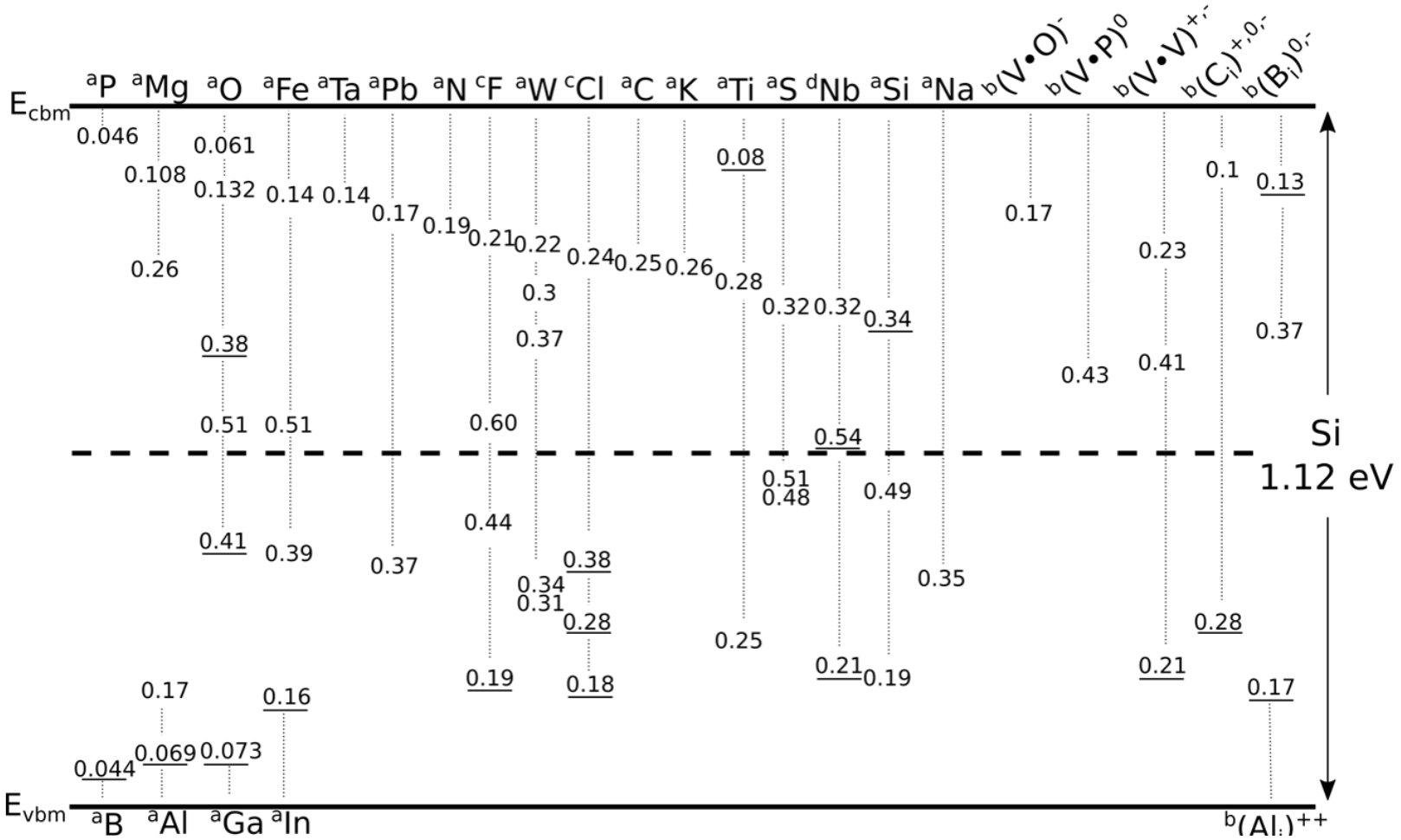

Figure 1: Selected defects and Si vacancy traps, and their associated activation energies in silicon as reported in **a**: Sze (2008) [40], **b**: includes vacancy clusters and trapped interstitials from Watkins (2000) [18], **c**: Chen et. al. (1980) [23], and **d**: from Polignano et. al. (2010) [24]. Underlined values are acceptors, while numbers without underlines are donors.

1.4 The Niobium/Silicon Interface

Niobium is widely used on silicon substrates in superconducting electronics, including Josephson junctions and microwave resonators [5] [26]. Niobium is chosen for its low cost, relatively high superconducting transition temperature, Tc, of 9.2 K, and the ability to be sputter-deposited easily with low levels of contamination [27].

Silicon is known to react with metals at relatively low temperatures [28]. Based on the phase diagrams for the Nb-Si system, the compounds $NbSi_2$ and Nb_5Si_3 are expected to be stable at 200 °C or lower [29]. As a result of kinetic barriers, most Nb-Si reactions occur at higher temperatures. Multiple investigations find Nb films and other refractory metals such as Ti and V deposited onto Si, begin to form a compound when annealed at 500-650 °C [30][31]. Rubloff also reports that below the temperatures for silicide reactions, other material reaction types such as grain boundary and bulk diffusion dominate, observable at ~250-350 °C in the refractory metals [32]. Based on concerns for forming interfacial compounds and interface diffusion, Nb deposition on Si should be performed at temperatures below 250 °C.

The Hume-Rothery rules for solid solubility predict that bulk niobium would act as a solvent for silicon because of Si's lower valence. Hume-Rothery also predicts a low maximum limit of solid solubility, based on the difference in atomic radius and difference in crystal structure between Nb and Si. This has been experimentally confirmed in Ref. [33], where they measure intermixing and diffusion of Nb sputter-deposited with relatively high power of 300 W onto Si substrates. They measure 30-40 nm of intermixing and calculate the diffusivity at room temperature to be $D_{Nb \rightarrow Si}=1\times10^{-15}$

cm^2/s and $D_{Si \rightarrow Nb}=0$. They also find that sputtering In or Sn on top of the 300 nm Nb film can stimulate further reactions, including Si into Nb.

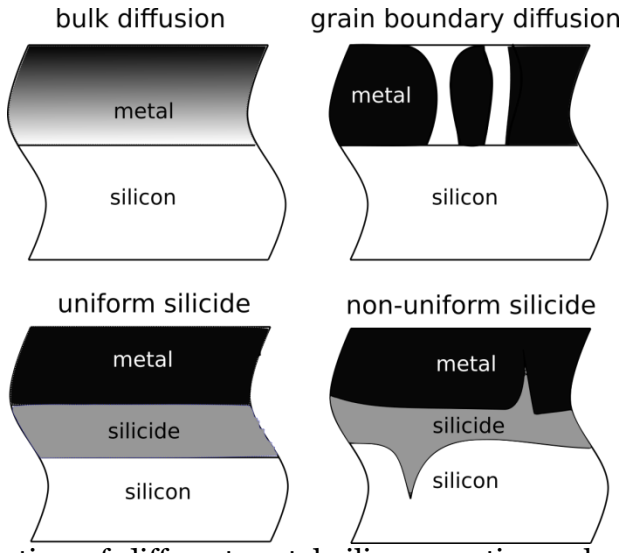

Figure 2: Representation of different metal-silicon reactions, showing bulk diffusion, grain boundary diffusion of Si into the metal, a uniform silicide reaction, and a non-uniform silicide reaction with preferential reactions occurring at defects or grain boundaries. Figure is based on Rubloff [32].

Typically, a metal reaction with silicon occurs in one of the methods shown in Figure 2; a uniform reaction, non-uniform reaction, bulk diffusion, or grain boundary diffusion. In some instances where the grain boundary or surface diffusion of silicon onto the metal is faster than the deposition rate, it is possible for a layer of silicon to "float" on the top surface of the metal [32]. Within this manuscript, the metal is deposited onto a single-crystal Si 100-oriented substrates using magnetron sputtering at power <200 W. This results in tall textured niobium grains, preferentially oriented with (110) perpendicular to the surface, and a diameter about 50 nm in the plane of the surface. This geometry may allow Si to move up Nb grain boundaries, as represented by the grain boundary diffusion in Figure 2.

CHAPTER 2

EXPERIMENTAL TECHNIQUES AND METHODS

2.1 Introduction

The effects and properties of devices and materials probed within this manuscript exist outside the traditional range of human perception. Atomic length scales, cryogenic temperatures, low-pressures, and electromagnetic interactions require the use of sophisticated instrumentation to identify and quantify. This chapter will describe the basic theory behind the methods used to create the structures investigated, and the techniques for characterizing the structural, chemical, and electronic properties of these structures.

2.2 Deposition Methods

Vacuum deposition methods are critical to precisely control the composition and thickness of the materials used in this investigation. The three vacuum film deposition methods used in this investigation are magnetron sputtering, Molecular Beam Epitaxy (MBE), and Pulsed Laser Deposition (PLD). Each excels at depositing different types of materials under different conditions, but all techniques are performed in cryo-pumped Ultra High Vacuum (UHV) chambers with base pressures of 10^{-9}–10^{-10} Torr to minimize impurity concentration.

Excluding contamination from surface residue and the deposition material itself, the residual pressure in the vacuum chamber and the rate of deposition affect the density of impurity contamination in deposited films. In addition to elements that are gasses at room temperature, each element has a temperature-dependent vapor pressure, many

described in Ref. [34]. The contamination rate is related to the flux of impurity atoms impinging on the specimen surface during deposition, calculated from the ideal gas law and the mean free path and the sticking coefficient, S, as described by the following equation:

$$F = \frac{1}{4} S \rho \bar{v} \tag{5}$$

where F is the incident flux, ρ is the molecular density of the gas, and $\bar{v}$ is the average molecular velocity. Expanding this equation leads to:

$$F = \frac{1}{4}\left(\frac{P}{kT}\right)\sqrt{\left(\frac{8kT}{m\pi}\right)} = \frac{PS}{\sqrt{2\pi mkT}} \tag{6}$$

Based on this, an MBE system operating at a base pressure of 10^{-10} Torr (1.333×10^{-8} Pa) would have an impingement rate of 5×10^{10} $cm^{-2}sec^{-1}$ corresponding to nearly 1/1000 of a monolayer per second. For semiconductor surfaces, the sticking coefficient of atmospheric gasses can be as low as 10^{-5}, while in metals it is often close to one. For growth rates of monolayers per second, the level of contamination when growing a semiconductor can be kept to parts per million and even parts per billion. Depending on the sticking coefficient, impurity concentrations in metals and reactive semiconductors, like $Al_xGa_{1-x}As$, can be higher, which can be estimated to be parts per million.

Magnetron sputter deposition is used to deposit thin-films at a high rate. In this study, deposition is performed in a UHV chamber with base pressure less than 2×10^{-9} Torr, with a load-lock to avoid exposing the chamber to atmospheric contaminants. After loading the substrate and evacuating the chamber to the base pressure, high-purity (99.9999%) Ar is introduced into the chamber to a total pressure of 4 mTorr, enough to create an ionized plasma that sputters atoms off the target to deposit onto the substrate.

Molecular beam Epitaxy (MBE) is a thermal evaporation based deposition technique that was initially developed for the deposition of epitaxial films. MBE involves precisely heating a crucible with a small opening to evaporate the source material. The evaporated atoms land on the surface with low energy and experimenters can control the surface mobility and crystal growth regime by adjusting the arrival rate and substrate temperature. Even at high source temperatures, the deposition rates are traditionally very low, and MBE subsequently requires very low background pressure to minimize contamination.

Pulsed Laser Deposition (PLD) or laser ablation, is a convenient technique to deposit thin films of complex structured materials; in this study, perovskites and oxides such as $Y_1Ba_2Cu_3O_7$, and $Ba(Zn_{1/3}Ta_{2/3})O_3$. The PLD technique works using high powered focused laser pulses to ablate material from a target, forming a plasma plume that condenses onto the substrate. In this study, the laser used is a KrF excimer laser (Lambda Physik model Compex 201, Germany) with incident wavelength 248 nm, and energy density of ~40 J/cm^2. Because of the very high energy density of the incident laser, multi-element targets with widely varying masses and sputter yield are all vaporized at the same rate. The laser energy can be tuned to deposit a single monolayer or less per pulse, allowing precise thickness control and deposition rate. This leaves only the kinetic decomposition and desorption on the sample surface as the dominant barrier to the stoichiometric deposition of high vapor pressure materials [35]. Additionally, PLD can be performed under a wide range of gaseous environments, from UHV conditions to very high pressures. In the following experiments, the chamber is evacuated to UHV pressures after loading the substrates to remove contaminants before introducing oxygen during deposition.

2.3.1 X-ray Diffraction

X-ray Diffraction (XRD) results from the scattering of X-rays by the atoms of a specimen material, with resulting diffracted beams at angles and intensities characteristic of the material structure. The X-ray wavelengths are on similar dimensions as the atomic spacing and distance between lattice planes, so interference between the diffracted beams creates Bragg diffraction peaks that yield information about the long-range order of the target specimen. This technique can identify crystal structure information such as symmetry, strain, and crystallinity, and is a useful tool to identify phases based on a library of known lattice spacings and calculated structures.

For analysis of thin films, XRD primarily uses a geometry referred to as the "coupled θ-2θ" geometry, which sweeps the angle between source and detector (2θ) while keeping the angle between the specimen surface and the source (ω) constant, as described in Figure 3. For crystallographic orientations perpendicular to the sample surface, ω=θ, but even a small offset can significantly affect diffraction conditions. The Bragg equation describes the angles of diffracted photons for the Bragg condition,

$$n\lambda = 2d_{hkl}\sin(\theta) \tag{7}$$

where n is an integer multiplier, λ is the wavelength of incoming photons (when $Cu_{K\alpha}$ radiation is used, λ=1.54 Å), d_{hkl} is the distance between lattice planes and θ is half of the angle between the incident and diffracted beam, as in Figure 3. In reciprocal space, where families of planes are condensed to a point, the Ewald sphere is used to describe X-ray diffraction. The incident beam (K_i) has a fixed magnitude $|K_i| = 2\pi/\lambda$ and the diffracted beam K_d scans across the surface of the sphere. Where the surface of the

sphere intersects a family of planes, diffraction occurs, and the scattering vector is defined $\Delta K = K_d - K_i$.

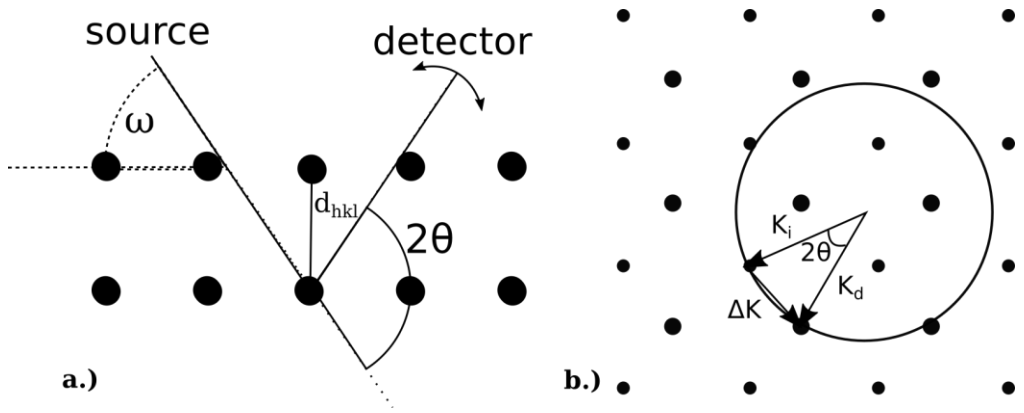

Figure 3: 2-Dimensional representations of the X-ray diffraction scan configuration for (a) real-space and (b) reciprocal (K-space). In (a), the black dots represent specimen lattice atoms, and the lines from the source to the detector represent the path of x-rays. In (b), the black dots represent families of lattice planes and points that intersect the circle meeting the Bragg condition for diffraction.

A typical coupled θ-2θ X-ray diffraction measurement for this geometry is interpreted using diffracted beam intensity vs. 2θ angle, directly yielding information about the distribution of interlayer lattice spacing perpendicular to the surface. Estimates of relative peak intensity are derived from the structure factor, and by comparing the relative measured yields to the calculated yields, preferential orientation or texture can be inferred. Even more information about specimen structure can be learned through the application of additional XRD techniques [36].

The X-ray diffractometer instrument used throughout this investigation is a PANalytical X'Pert MRD Pro. X-rays are Cu-K_α wavelength (λ=1.54 Å), and the angles and X-ray optics are modified depending on the experiment. For analysis of thick high-crystalline-quality films, the incident beam passes through an X-ray monochromator, which limits the wavelength to a very narrow range for high-resolution diffraction. The diffracted beam then travels through a second monochromator, attached to a triple-axis

detector. This configuration has the advantage of the highest angular resolution, but filtering through two monochromators significantly reduces the beam intensity and, subsequently, the detected yield. The preferred optics for measuring thin films, especially for thicknesses below 100 nm, are an incident x-ray mirror and receiving parallel plate collimator (PPC) [37]. These sacrifice some angular resolution in exchange for much higher diffracted beam intensity. The mirror/PPC optics create a parallel beam condition, where a wide beam can probe a larger sample area with minimal deconstructive interference, different from the conditions achieved with point source or X-ray slits.

2.3.2 **Transmission Electron Microscopy**

Transmission Electron Microscopy (TEM) uses the interaction of an electron beam with a thin electron transparent specimen to study the chemical and structural properties of thin specimens with very high resolution, which is as low as ~0.5 Å in the instruments used here. This technique is useful for high-resolution imaging and analytical analysis techniques such as diffraction and spectrometry. This section will explain only the TEM techniques used for this study.

Different experiments require different experimental configurations, but the basic geometry of a TEM transmits a beam of electrons through a very thin specimen, typically 100 nm or less, onto a detector on the opposite side. Some microscopes operate in a Scanning Transmission Electron Microscope (STEM) mode, which uses a very small incident beam that is rastered across the specimen to build an image pixel by pixel. A Bright Field (BF) image records information about the center transmitted spot, which primarily results in a reduction in the intensity in the position of the atom, with heavier atoms appearing darker than light atoms because of the enhanced scattering. The Dark

Field (DF) image obscures the direct beam, and with an objective aperture placed around a diffraction spot can yield an image with diffraction contrast, or for High-Angle Annular Dark Field (HAADF), high mass contrast.

The Scanning TEM (STEM) technique is especially useful for spatially resolved analytical techniques, including EDX. Energy-Dispersive X-ray Spectroscopy (EDX) records secondary electrons emitted by the specimen as a result of excitation from the electron beam. These characteristic x-rays are used for high-resolution elemental mapping or identification of precipitates.

Precession diffraction is a STEM technique used to extract highly spatially-resolved structural information about a specimen. A measurement area is selected based on the STEM image, then at each pixel within that image, the specimen is rotated in a circle, and a diffraction pattern is recorded for each angle. After computer analysis of each diffraction pattern in the image, structural information can be visualized with reconstructed real-space images. Precession diffraction allows for the spatial mapping of different phases or grains within a specimen.

Careful specimen preparation is essential for reliable TEM analysis and can be much more complicated than specimen preparation requirements for other characterization techniques. Two methods of specimen preparation are used in this study, Focused Ion Beam (FIB) lift-out and rod-and-tube “manual” sample fabrication. Focused Ion Beam is commonly used in the semiconductor device industry for its quick ability to create specimens from specific areas of electronic devices in cross-section for failure analysis. The specimen is typically created using a Ga ion beam to mill trenches into a sample surface, leaving a “V” shape wedge specimen. A lift-off arm is then affixed to the thick top part of the wedge with e-beam deposited platinum, then the remaining sides of the wedge are milled away, and the cross-section can be “lifted” out of the

sample. Once the wedge specimen is free of the bulk sample, it is thinned to electron transparent thicknesses using lower energy Ga milling. The disadvantages of FIB lift-out are that the milling beam can cause damage to the specimen, including interfacial intermixing and amorphization, and it can be challenging to make a specimen uniformly electron transparent, especially at interfaces of dissimilar materials with different mill rates. In the manual "rod-and-tube" sample preparation, specimens are bonded with epoxy inside a brass and steel support tube and then diced into thin cross-sections. Cross-section discs are mechanically polished down to less than 100 μm thickness, thinned to a few μm thick in the center using a dimple grinder, and finally polished to electron transparent thicknesses using a low energy Ar ion milling Precision Ion Polishing System (PIPS) mill.

Two TEM instruments are used here, the aberration-corrected Jeol ARM200F with in-situ Energy Dispersive X-ray Spectroscopy (EDS), and an attached AppFive precession electron diffraction system, and the aberration-corrected NION UltraSTEM 100.

2.3.3 **Raman Spectroscopy**

Raman spectroscopy measures the energy of vibration and rotation modes in crystals and molecules by measuring the energy shift of inelastically scattered photons. For this technique, a monochromated laser impinges on a specimen surface. Most photons are reflected through the reflection or elastic scattering processes; however, some photons are absorbed and re-emitted at different energies due to interaction with low-energy phonons and excitation of molecules into higher vibrational or rotational modes corresponding to the degrees of freedom for the target molecule. Observations of emission at these energies can be used to identify defects and different phased in solids.

2.4.1 **Rutherford Backscattering Spectroscopy**

Rutherford Backscattering Spectrometry (RBS) is a non-destructive technique used to determine composition as a function of the thickness of thin-film specimens to within at least 0.1 at% and a few Å. This technique measures the energy of α-particles (He^{2+} ions) after backscattering from specimen atoms through the Rutherford scattering process. The energy change is determined by the mass of the target atom, and the target atom depth can be determined based on predictable columbic losses as α-particles travel through the target matrix.

Specimens for RBS are placed in a vacuum chamber with a base pressure of less than 10^{-8} Torr, to minimize scattering from atmospheric molecules. Incident ions are accelerated to an energy 2 MeV or higher using a linear accelerator. A 1.7 MV Tandetron accelerator is used to accelerate the α-particles used for this investigation, with maximum accelerating voltage of ~5.1 MeV. The incident energy well-controlled by the acceleration voltage, and after backscattering, the energy of the scattered ion is measured using a silicon surface barrier detector. The mass of specimen atoms are calculated by comparing the energy ratio of incident and scattered ions, which is determined by the kinematic factor, κ. [36]

$$\frac{E_1}{E_0} = \kappa = \left(\frac{M_1 \cos(\theta) + \sqrt{M_2^2 - M_1^2 \sin^2(\theta)}}{M_2 + M_1} \right)^2 \qquad (8)$$

with E_1 as the energy of the scattered particle, E_0 is the energy of the incident particle; M_1 is mass of the incident particle, M_2 mass of the target atom, and θ the scattering angle in the lab frame of reference. The detector is typically set at 170°. The probability of a

scattering event depends on the statistical probability of the incident particle coming close to a target atom and the angular-dependent scattering cross-section, σ, is

$$\sigma(\theta) = \frac{(d/4)^2}{\sin^4 \theta/2} \tag{9}$$

Where d is the distance of closest approach for scattering given by

$$d = \frac{Z_1 Z_2 e^2}{E_0} \tag{10}$$

Where Z_1 and Z_2 are the atomic numbers of the incident and sample atoms, and e the incident charge. The scattering cross-section is typically normalized to the solid angle of the detector, $d\sigma/d\Omega$. By integrating the yield-vs-energy peak associated with a particular element, the total atomic count can be determined in aerial units of atoms/cm^2. The thickness is calculated by assuming a film density and multiplying that by the measured aerial density. RBS does not require the use of a standard to determine the composition or the total number of atoms. However, to determine the thickness, the density of the material needs to either be available from the literature or measured. The accuracy of RBS determinations can be to nearly a single monolayer (~5×10^{15} atoms/cm^2) in thickness and ~0.1 atomic percent in composition. Its probe depth is about one μm. RBS has limited detection of light elements, typically lighter than O, and there can be difficulties in resolving small percent-differences in target element mass, especially at high masses. However, the complementary analysis techniques Elastic Recoil Detection (ERD), Nuclear Reaction Analysis (NRA), and helium/proton-induced X-ray emission (HeIXE/PIXE) can be used to make up for the deficiencies of RBS, given that they are based on different detection mechanisms. Nuclear reaction analysis (NRA) is useful for measuring concentrations of light atoms which have a low probability of back-scattering ions in the direction of the detector, with a $\theta_{detector}$ of 170°. In NRA, the incident energy is selected to maximize the probability of a reaction with a particular target nucleus. These

reactions typically involve the absorption of the incident particle into the target nucleus, creating an unstable nucleus that then decays to a stable form.

RBS and ERD analysis performed in this investigation use incident α-particles with energy 2.0 MeV for most scans, including HeIXE and ERD. The beam spot size is ~3×3 mm², the sample is kept 8° off the beam normal, and rotated slowly to minimize ion channeling. Higher energies are used to resolve higher mass target atoms and for NRA. The reaction $^{16}O(\alpha,\alpha_0)^{16}O$ at 3.05 MeV is used for oxygen-resonance NRA, where the incident α-particle reacts with the oxygen nucleus to emit a different α-particle, and $^{12}C(\alpha,\alpha_0)^{12}C$ at 3.58 MeV for carbon-resonance NRA.

2.4.2 **Proton/Helium Induced X-Ray Emission Spectroscopy**

Proton and Helium induced X-Ray Emission Spectroscopy use the same accelerator as RBS, but instead measures the energy of characteristic X-rays emitted. It can measure several orders of magnitude lower concentrations of atoms and discriminate between elements with the same or similar atomic mass. Incident particles with MeV energies can ionize inner shell electrons of target atoms, and then electrons from outer shells fall to replace the hole, releasing an X-ray of energy characteristic of the particular transition and atom. These transitions are characteristic of the element, based on the quantization of electron energy levels in an atom, where $E_{X-ray} = h\nu = E_2 - E_1$. Probe dimensions are up to 1 μm deep, limited by incident ion depth, dependent on incident energy and target mass, with a probe diameter on the order of a few mm, so these techniques are typically used to probe large areas of thin films or bulk specimens. PIXE and HeIXE have limited detection of light elements, typically emissions from elements fluorine and lighter. PIXE has the advantage that it can be performed in the

atmosphere, on samples of large size outside the confines of the metal vacuum chamber, as shown in Figure 4. Determining quantitative composition requires a standard with a similar matrix composition, but positive identifications and relative concentrations can be measured without standards. Neither PIXE nor HeIXE detectors are sensitive to secondary electron emission, and the heavier incident ions at MeV energies are less affected by charge buildup than keV electrons, meaning specimens do not need a coating of conducting material to avoid charge buildup as with scanning electron microscope coupled techniques such as EDS.

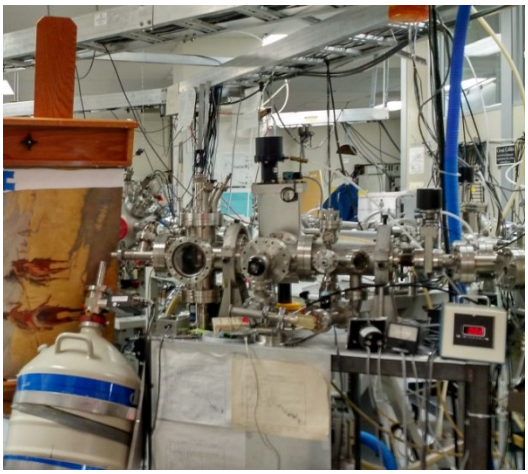

Figure 4: PIXE is a non-destructive technique that can be performed on sensitive and arbitrarily large samples in a standard atmosphere.

In this investigation, PIXE and HeIXE use protons and α-particles. HeIXE was performed in a vacuum chamber in pressures of $<10^{-8}$ Torr, and PIXE was performed at standard atmospheric pressure. Different incident energies 2.0 and 3.0 MeV are used to excite different X-ray energy levels, and detector filters are mylar and aluminum. The PIXE detector is cooled with liquid nitrogen, and the HeIXE detector is cooled with a thermo-electric chiller.

2.5 Time of Flight Secondary Ion Mass Spectrometry

Time of Flight Secondary Ion Mass Spectrometry (TOF-SIMS) is a technique for measuring atomic concentrations with spatial and depth resolution, commonly used in the semiconductor industry to identify impurities. The TOF-SIMS instrument used can identify atoms and molecules with masses from 1 to 10,000 amu, with a sensitivity as low as 10^{14} cm^{-3} and a mass resolution, m/δm, of 1 part in 8000. Time of flight differs from traditional SIMS by accelerating all secondary ions from the specimen up a column, where they are then reflected and hit a detector at different times based on their atomic masses. A heavier ion requires more time to travel the large ~2 m distance than a lighter ion, so the mass resolution is based on detection time. The biased extraction tip increases the collection efficiency, so more sputtered ions are collected, and time-of-flight allows a full mass-spectrum to be recorded for each pulse. This means that hydrogen ions, compounds, and large molecules can be measured simultaneously without changing the instrument configuration.

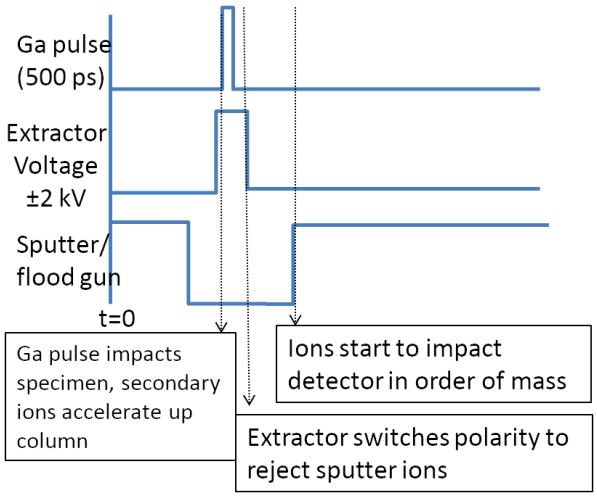

Figure 5 representative diagram of the pulse timings for a single cycle of the interlaced Ga analysis beams, sputter source, and extractor voltage in an “interlaced” sputter depth profile mode.

The analysis beam consists of pulsed isotopically enriched ^{69}Ga ions that, upon collision with the surface, creates both positive and negative secondary ions. The primary Ga analysis ion at 2.5 kV only interacts with the top monolayer of specimen atoms, so in order to measure anything deeper, this analysis beam is used along with a sputter beam of either Cs or O ions (see Figure 5), depending on what elements are being investigated and whether positive or negative secondary ions are desired.

In sputter depth profiling, it is important to consider the effects of the incident particles on the specimen. The incident sputter ions will cause some broadening in the depth profile, reducing depth resolution, so experimental parameters must be optimized to minimize these effects. In this case, both the incident ion and the target recoil atom are scattered, with some surface atoms potentially moved further into the target matrix in a knock-on reaction.

Sputter and analysis beams will cause changes to both surface topography and surface composition. As a result, it is vital to choose appropriate sputter and analysis areas and to have a uniform raster across the area in order to avoid measuring secondary ions from unintended regions of the sample. A sputter trench must be much larger than the analysis area, to avoid analyzing ions from the trench sides. The trench must also have a flat bottom, and induce minimal roughness, or the depth will be poorly defined, reducing depth resolution. Furthermore, the incident sputter ions should cause minimal intermixing or knock-ons within the specimen, reducing the effective depth profile. SRIM/TRIM[38]. Simulations of intermixing near a Nb-Si interface caused by a Cs sputter beam at 1 kV estimate about 2-3 nm of intermixing.

In addition to concerns about intermixing, the sputter ion species can affect the SIMS results. Many sputter ion species are available, and because some sputter ions

become embedded in the sample, the selection of polarity and species affects the charge of the specimen surface and the ionization potentials of the secondary atoms. Because of this, both the matrix and desired secondary ions must be carefully considered. Two common sputter ions as used for this analysis include O_2^+ and Cs^+, where positive secondary ions will be preferentially created by O_2^+ ions and negative secondary ions by Cs^+.

The TOF-SIMS used for this investigation is an ION TOF model TOF-SIMS IV (Muenster, Germany), with an un-baked base pressure of 8×10^{-10} Torr. A Ga primary beam and a Cs sputter beam are used. In order to characterize the Nb-semiconductor interfaces in this investigation, negative secondary ions are recorded, since most elements of interest (H, C, N, O, F, Cl) more readily form negative ions. Sputtering is performed at a low enough acceleration voltage, typically of ≈1 kV, to minimize the sputter rate and maximize depth resolution. However, this slow sputter rate reduces the background sensitivity due to re-deposition on the sample surface.

2.6 Electrical Characterization Methods

The electrical properties of materials and devices can provide important information about contamination and defects in materials with higher sensitivity than nearly any other technique. Specimens were measured with current-voltage profiling (I-V), and Deep Level Transient Spectroscopy (DLTS). These techniques offer insight into the interface and device properties of the semiconductor layer and can measure properties of defects that can be used to determine their concentration and identify their physical nature.

2.6.1 **Current-Voltage Characterization**

Current-Voltage (I-V) and Capacitance Voltage (C-V) profiling can detect small concentrations of contaminants and structural changes in the material [39]. I-V is performed by applying a voltage across a device and measuring the resulting current. The applied voltage is swept across forward and reverse bias, and the resulting current response is measured. For a metal-semiconductor-metal device with ohmic contacts, the I-V slope is linear with the slope describing the resistance (R=I/V). For a Schottky diode the current will increase exponentially with voltage with the equation

$$I = SA^*T^2 \exp\left(-\frac{q\phi_B}{k_B T}\right)\left[\exp\left(\frac{qV - IR_S}{nk_B T}\right)\right] \tag{11}$$

where S is the device area, A^* the Richardson constant (8.1 $AK^{-2}cm^{-2}$ for Si), T the measurement temperature, k_B the Boltzmann constant, q the carrier charge, ϕ_B is the barrier height, R_S the series resistance, and n is the ideality factor [40]. The I-V data are expressed in terms of a semi-log plot for ease of interpretation for the exponential terms. The first term, $SA^*T^2 \exp\left(-\frac{q\phi_B}{k_B T}\right)$, is often referred to as the saturation current, I_S. For thermionic emission, the ideality factor (n) will be one. Values in high-quality devices are near 1.02 because of the additional presence of image force lowering and tunneling [41]. When defect levels exist between the electron and hole quasi-Fermi levels in forward bias, then Shockley, Read, Hall recombination results in the ideality factor approaching n=2. When multiple barriers exist across a device, as a result of pinholes, surface conduction, or non-uniform contact formation, the lowest barrier will dominate until the current density of those paths saturates. This surface conduction effect is illustrated in Ref. [41], where they find a mesa etch removes the excess current.

Current-Voltage measurements are performed using a picoammeter with built-in D-C bias (Hewlett-Packard Model 4140B, Palo Alto, CA) on the cold stage of a closed-

cycle cryogenic refrigerator (Cryosystems model LTS-21, Westerville, Ohio). Because this is a 2-point measurement, contact resistance plays a large part in the total series resistance of the device, so procedures must be developed to form reliable, repeatable contacts across the entire range of measurement temperatures. High-precision I-V profiling measurements require temperature stability within a few Kelvin during the ~2-mintue measurement. A temperature controller (Lakeshore Model 331, Westerville, Ohio) with a cartridge heater on the cryo-stage is used along with the cryo-cooler to keep the temperature constant during each I-V measurement. To further ensure the temperature of the sample is the same as is measured on the stage, an indium foil is placed between the specimen and cryo-stage to maximize thermal contact, and the temperature is held at the measurement temperature for ~5 minutes before recording data.

2.6.2 **Deep Level Transient Spectroscopy**

Deep Level Transient Spectroscopy (DLTS) studies are used to identify the nature, energy, concentration, and emission cross-section of electrically active defects within the depletion region of semiconductors. DLTS has the advantage of a very low defect density detection limit ~10^9 cm^{-3}, significantly lower than detection limits for any chemical characterization techniques. DLTS works by measuring the time-dependent change in capacitance while applying a pulsed bias to a Schottky diode. First, a reverse-bias is applied to empty defects in the gap, and then short forward-bias pulses fill defect levels. When the device returns to a reverse-bias condition, these filled defects/traps emit back to the nearest band, E_{cbm} or E_{vbm}, over time, resulting in a capacitance change that can be amplified with a lock-in amplifier and measured. This capacitance measurement is limited to a “rate window” after removing the forward pulse between 0.1 Hz and many

kHz and is repeated while sweeping the sample temperature. Multiple temperature sweeps are performed with different measurement rate windows, resulting in a series of frequency-dependent temperature spectra, δC-vs-T. In these temperature profiles, peaks correspond to defects, with negative changes, referred to as "peaks" here, in capacitance corresponding to majority carrier defects, and positive changes corresponding to minority carrier defects, these peaks shift in temperature position and intensity across measurements performed with different rate windows. An Arrhenius plot is formed for peak temperature T position and emission rate τ_e intensity, then fit to the equation relating emission rate to temperature.

$$\tau_e T^2 = \frac{\exp\left(E_T/k_B T\right)}{\gamma\sigma} \tag{12}$$

This fit yields the energy level from the nearest band, E_T, and the capture cross-section, σ, using the coefficient $\gamma = 1.78\times10^{21}\ cm^{-2}s^{-1}K^{-2}$ for p-type Si. This γ value is based on the thermal velocity and the effective density of states in the semiconductor [39 p. 262].

Depth profiling is possible using DLTS, sometimes called double-correlation DLTS. This technique fixes the temperature and rate window, then applies two pulses of different forward biases on alternating cycles. The difference in δC between the two pulses corresponds to the defect concentration that resides in the difference between space charge regions defined by the different voltages. By keeping the voltage difference constant, then scanning the forward pulse voltage, a depth profile can be constructed. Selecting parameters for this depth profiling technique requires already performing temperature DLTS at multiple rate windows, then selecting the appropriate values for each particular defect.

CHAPTER 3

MICROWAVE PROPERTIES OF DEPOSITED DIELECTRICS

3.1 Abstract

This study finds that deposited Ge and Si dielectric thin-films can exhibit low microwave losses at near single-photon powers and sub-Kelvin temperatures. The low loss enables these materials to use in a wide range of devices, including low-loss coplanar, microstrip, and stripline resonators, as well as layers for device isolation, inter-wiring dielectrics, and passivation in microwave and Josephson junction circuit fabrication. The investigation uses coplanar microwave resonator structures with narrow trace widths of 2-5 μm to maximize the sensitivity to the interface and properties of the deposited dielectrics, rather than to optimize the quality factor. In this configuration, thermally-evaporated approximately one-μm thick amorphous germanium, *a*-Ge, films deposited on Si (100) have a single photon loss tangent of $1\text{-}2\times10^{-6}$ and, nine-μm thick chemical vapor deposited (CVD) homoepitaxial Si has a single photon loss tangent of $0.6\text{–}2\times10^{-5}$. Simulations indicate that interface losses are non-negligible.

3.2 Introduction

Microwave resonators fabricated for use in superconducting quantum computing and sensing applications are almost always fabricated in the co-planar configuration on bulk, high-purity single-crystal Si and sapphire, Al_2O_3, dielectrics [42][43][6][44]. The resonator performance at low temperatures and near single-photon powers is limited by

dielectric and two-level system losses in the dielectric material, and at the metal-air, metal-dielectric, and dielectric-air interfaces[45][46][47][48].

Several-micron-thick high-purity CVD homoepitaxial silicon is a viable alternative dielectric for co-planar structures for the following reasons. These deposited films are available in very pure form with uncompensated carrier concentrations as low as 10^{12} cm^{-3} and structural defect densities less than 1 cm^{-2}. Epitaxial Si layers have proven to have better performance in high-power Si device applications over their bulk Si counterparts. Such layers are believed to have a different defect composition than float-zone Si wafers, which have of order 5×10^{15} cm^{-3} oxygen and carbon contaminants and a significantly higher number of electrically inactive defects that do not degrade performance at room temperature[49]. Such bulk Si defects could undergo multi-atom configuration changes at low temperatures and thus could contribute to loss and noise in quantum-based computing and sensing applications.

While the favored substrates for these low-temperature applications are single crystal material, other dielectrics, including SiO_2, Si_3N_4, and SiO_xN_y, are used as isolation, inter-wiring, and passivation layers in microwave device and Josephson junction circuit processes. Unfortunately, these materials have high loss tangents[50] of $0.1–3\times10^{-3}$. The most used materials are made with plasma-enhanced chemical vapor deposition (PECVD), which requires temperatures of ~350–400 °C to produce electrically-insulating low-defect density material. However, for superconductor device fabrication, temperature limits [51] of ~150-175 °C are imposed to prevent thermally induced changes in the Josephson junction and microwave devices. Such temperature limits result in dielectric films with high performance-degrading defect densities.

High-purity germanium substrates and deposited films are viable candidates for dielectric layers in multi-layer superconductor circuits. Germanium can be obtained in

an even higher purity [52] form than Si, with impurity concentrations as low as 10^8 cm^{-3}. High-resistivity germanium films can be deposited via evaporation at low substrate temperatures, including down to room temperature. If no additional contamination is added during the deposition process, only a few tens of impurity defects would be present in the entire active region of coplanar, microstrip, or stripline structures. It could also potentially replace commonly-used deposited dielectrics with high-loss in microwave and Josephson junction circuit fabrication.

This study documents the microwave and two-level system losses in Nb-based coplanar microwave resonators synthesized on molecular-beam evaporated 1 μm-thick Ge thin-films and on chemical vapor deposited (CVD) 9 μm-thick homoepitaxial Si thin-films. To enhance the measurement sensitivity to the interface and properties of the deposited dielectrics, the resonators for this study have been intentionally designed with narrow trace width, defined as the width of the center superconductor in the device, and minimal, less than~20 nm over-etch. This is in contrast to other studies that focus on maximizing the quality factors by designing resonators with large trace widths of over 10 μm and significant over-etch [53][54].

3.3 Experimental Procedures

Amorphous germanium, *a*-Ge, films are evaporated onto undoped float-zone Si (100) substrates with resistivities greater than 10 kOhm-cm. Undoped crystalline Ge wafers were broken up into small pieces for use as evaporation material. The Si substrate surface is cleaned in ultrasonic baths of USP-grade acetone, then ethanol for ten minutes, followed by etching for 5 minutes in aqueous 2% HF solution. For Ge

deposition, the chamber is evacuated to a base pressure of less than 5×10^{-9} Torr before slowly warming the Ge evaporation source (SVT High Temperature Effusion Cell) to 1400 °C. The Ge is deposited at ~0.25 nm/sec to a total film thickness of ~1 μm.

X-ray diffraction of Ge films is performed using a PANalytical X'Pert MRD Pro high-resolution diffractometer in the θ-2θ configuration, and Raman spectroscopy uses a 532 nm laser operating at 0.75 mW with 0.5 μm spot size.

Epitaxial Si films are prepared in a commercial foundry at Lawrence Semiconductor Research Laboratories (Tempe, AZ). The substrate is a (100) orientation CZ-grown Si wafer with resistivity, ρ, from 1000-25,000 Ω-cm, cleaned using an in-situ high purity HCl etch. The ~9 μm thick epitaxial-layer was deposited at 900° C, using 2% silane in H_2, with a deposition rate of ~300 nm/minute. Prior to insertion into the Nb metal layer deposition system, the Si film surface is cleaned in ultrasonic baths for 10 minutes—first in semiconductor-grade acetone, then ethanol. To remove residual surface contamination from the epi Si/Si, the film is flash-heated in vacuum [55] at less than 5×10^{-9} Torr to 850 °C, and then held at 650 °C for 1 hour before cooling for about 1 hour to room temperature before Nb sputter deposition.

Nb metal films are sputter-deposited onto the substrates or deposited layers without breaking vacuum in the case of *a*-Ge to minimize surface contamination. Sputter deposition is performed at room temperature and 4 mTorr of Ar in a UHV system with an unbaked base pressure $<5\times10^{-9}$ Torr using a 2" diameter magnetron sputter source with 99.95%-pure Nb targets. The sputter power is 225 W with a source-film distance of 15 cm, resulting in a sputter rate of ~0.6 nm/sec.

Chemical depth profiles are obtained using Time of Flight Secondary Ion Mass Spectrometry (TOF-SIMS). The analysis beam uses Ga^+ ions with a 1 kV Cs sputter ion

beam for depth profiling. Because SIMS sensitivity factors are only available for the bulk, and differ significantly from these values for the disordered atomic structures near these Nb/semiconductor junctions, all near-interfacial data presented here will be in raw counts normalized to the relative count rate of the host matrix Nb or Ge and are not accurate estimates of atomic concentration.

Coplanar-waveguide, CPW, resonators are prepared using standard photolithography and reactive ion etching, RIE, in a CF_4 plasma. Devices are patterned into the stripline resonator configuration with 2-5 μm trace width and gap width, and less than 20 nm over-etch to maximize electric field interaction with the interface and dielectric films under study. The quarter-wave CPW resonators are capacitively coupled to the microwave feed line. Transmission measurements of the S_{21} parameter are made at ~40 mK as a function of applied power. The resonance is fit using the diameter correction method to extract Q_i the internal quality factor of the resonator and thus the loss tangent [56] $\tan\delta_i \sim Q_i^{-1}$. The power dependent loss tangents are then fit to the two level system model [57].

3.4 Results and Discussion

Carrier concentrations determined using room-temperature Hall Effect measurements find the deposited Ge film is n-type with 6×10^{12} cm^{-3} net carriers, essentially identical to the original wafer. Electron Paramagnetic Resonance, EPR, measurements on these *a*-Ge films performed using the in-situ parallel plate EPR technique described in earlier work[14], find the paramagnetic defect concentration is below the detection limit of $\approx10^{17}$ cm^{-3}. X-ray diffraction data on the *a*-Ge films do not exhibit any sharp Bragg diffraction peaks, characteristic of amorphous material. Raman

spectroscopy data, illustrated in Figure 6, exhibits broad transverse optical peaks, similar to those found for electrolytically deposited [58] *a*-Ge.

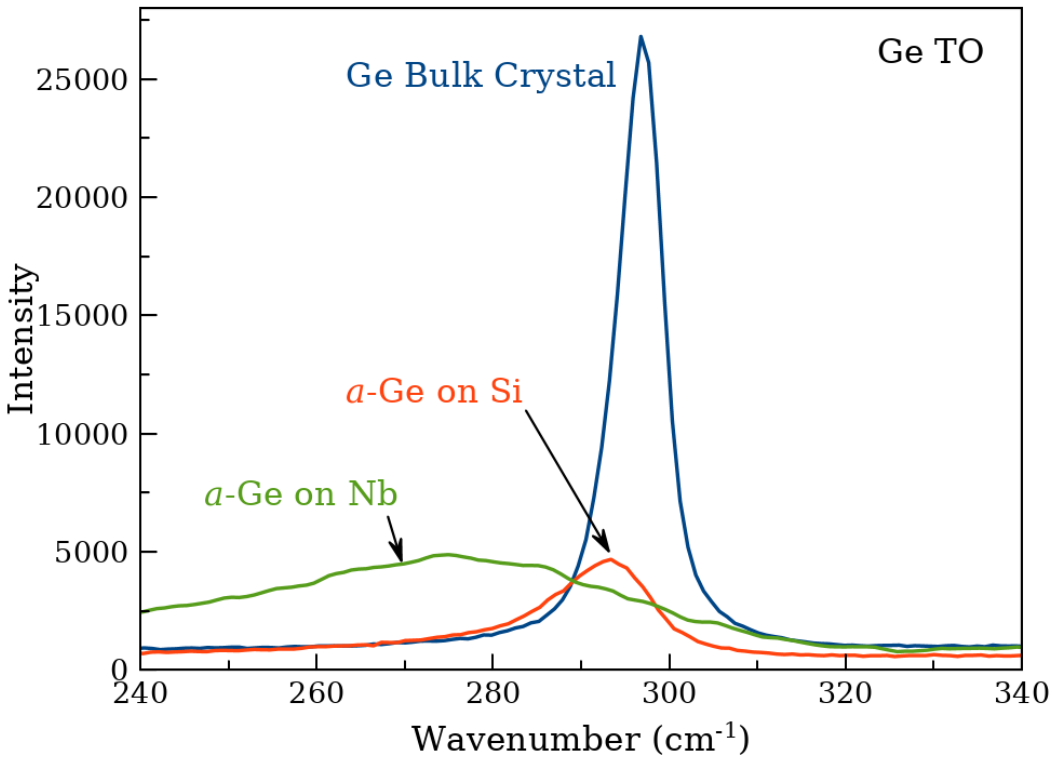

Figure 6: Raman spectroscopy for Ge transverse optical (TO) mode comparing a single crystalline bulk substrate (blue), Amorphous Ge deposited at room temperature on a Si substrate (red) has been shifted to, and (green) Amorphous Ge deposited at room temperature onto a 200 nm Nb film on Si.

Si films deposited under the same conditions as used in this study have been measured with spreading probe resistance to be slightly n-type, with net carrier concentrations less than 10^{12} cm^{-3} at room temperature. SIMS measurements find that the impurity concentration is below the detection limit of $\approx 10^{14}$ cm^{-3}.

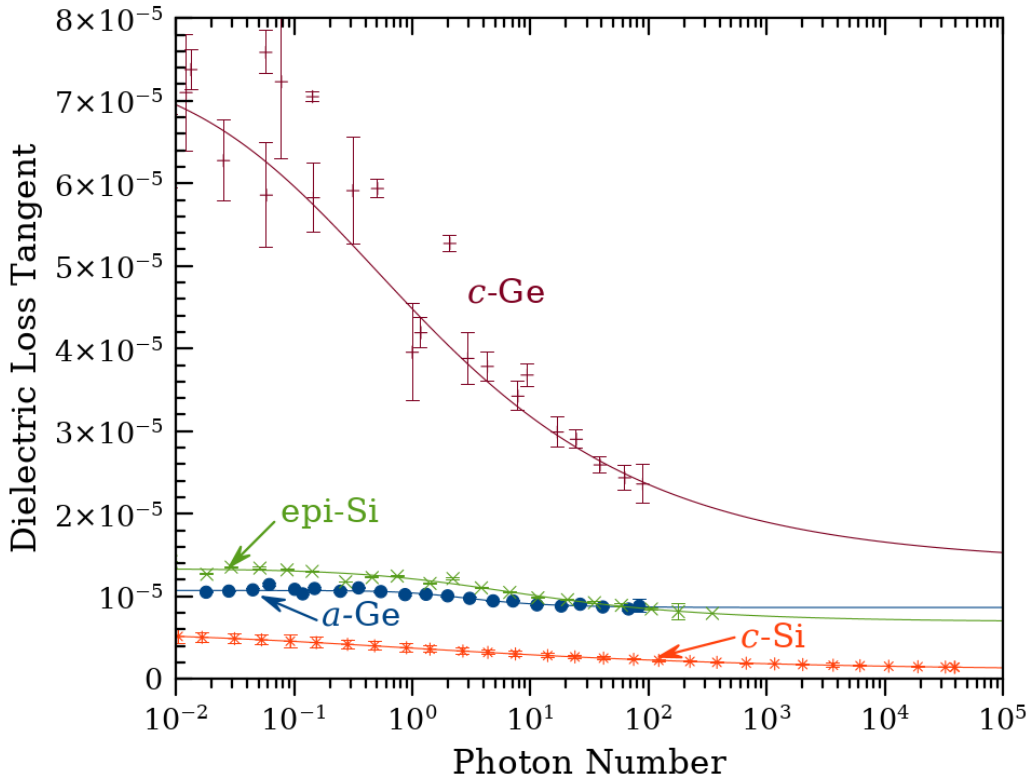

Figure 7: Dielectric loss tangents for niobium CPW 1, 4, 8, 11 devices measured at ≈40 mK shown as a function of photon number. The lines are fits to the two-level system model, and the power-dependent loss tangent from the fit are given in Table 1. Measurements performed in collaboration with Daniel Queen.

Table 1 and Figure 7 summarize results from low power, low-temperature microwave measurements on Nb-based CPW resonators on float-zone silicon, homoepitaxial Si films, a high-resistivity Ge wafer, and room-temperature deposited *a*-Ge. The resonator with room-temperature deposited *a*-Ge dielectric exhibits a total dielectric loss comparable to Nb/epi-Si wafer, and the lowest single-photon loss in a deposited amorphous dielectric reported to date. Low two-level system loss densities have also been reported in acoustic and thermal measurements on deposited amorphous dielectrics [59][60][61][62]. The *a*-Ge films deposited at room temperature without any post-processing exhibit single loss 6 times lower than reported values of internal friction

on e-beam and sputtered *a*-Ge films by Liu[60], and 2 times lower than those films reported with post-process annealing 5 for hours at 350 °C. The authors of those studies report that low energy excitations of *a*-Ge are highly dependent on the preparation method, which they attribute to structural differences in the films. Further enhancement may be possible based on later studies by Liu [61], where they report *a*-Si films that do not exhibit two-level system loss even without hydrogen passivation by using the optimized 400 °C substrate growth temperature, achieving $Q = 5 \times 10^5$ and thus $\tan\delta < 2 \times 10^{-6}$.

Dielectric Material	Sample	Two Level System Fit $\tan\delta_0$	Single Photon Loss Tangent	Effective Loss Tangent	Trace Width (μm)
a-Ge film (1 μm)	1	2.1×10^{-6}	1.1×10^{-5}	8×10^{-6}	2
	2	1.3×10^{-6}	1.3×10^{-5}	1×10^{-5}	16
Bulk *c*-Ge (Substrate)	3	6.6×10^{-5}	2.7×10^{-4}	3×10^{-4}	2
	4	6.1×10^{-5}	7.5×10^{-5}	4×10^{-5}	4
	5	2.4×10^{-4}	5.94×10^{-5}	6×10^{-5}	8
CVD Epi-Si film (9 μm)	6	9.2×10^{-6}	1.81×10^{-5}	2×10^{-5}	2
	7	1.1×10^{-6}	1.27×10^{-5}	1×10^{-5}	2
	8	6.5×10^{-6}	1.24×10^{-5}	1×10^{-5}	4
	9	3.9×10^{-6}	6.02×10^{-6}	3×10^{-6}	8
	10	1.2×10^{-5}	8.18×10^{-6}	6×10^{-6}	8
Si substrate	11	4.8×10^{-6}	3.5×10^{-6}	5×10^{-7}	5

Table 1: Summary of results for coplanar microwave resonators measured at near single-photon power and 40 K. Power-dependent losses of samples 1, 4, 8, 11, which have the lowest effective loss of each material system, are shown in Figure 7.

Comparing these results to those in the surveys of superconducting coplanar resonators[50][43][44], the high-purity deposited *a*-Ge films measured here exhibit loss much lower than has been reported for *a*-Si:H, sputtered *a*-Si, and lumped element *a*-SiN_x resonators [47]. The loss in the *a*-Ge film is similar in magnitude to early reports of high-quality resonators on Si or sapphire, but higher loss than more recent reports, including the CPW resonators on float-zone Si reported here. The loss in a superconducting resonator is sensitive to the cleanliness of the interfaces, and the devices presented here are no exception. The effective loss tangents shown in Table 1 have been estimated for each device by simulating the filling factor of the material of interest and assuming interfaces with a loss tangent of 1.5×10^{-3} and a filling factor of 2% based on the CPW geometry [48]. More reliable determination of the material and interface losses requires measuring a large number of resonators with varying geometries [10].

Time of flight SIMS depth profiles of the Nb/*a*-Ge and the Nb/crystalline Ge wafer interfaces identify H, C, O, F, and Cl at the interfaces, while the bulk of the Ge layer has very low contamination levels, as shown in Figure 8. The *a*-Ge which was deposited in-situ has fewer contaminants near the interface when compared to the Nb deposited directly on the air-exposed, chemically cleaned bulk Ge wafer. On the bulk Ge wafer, SIMS measures contamination C, F, and Cl peaks extending about 20, 20, and 40 nm into the Ge, respectively. Based on these results, the low losses in the deposited *a*-Ge and homoepitaxial Si resonators are not unexpected, given the high chemical purity of the deposited films and interfaces. In contrast, the crystalline Ge wafers have a much higher loss and much higher contamination at the interface, as determined by the TOF-SIMS depth profile in Figure 8. These TOF-SIMS data are shown with relative yield instead of

concentration to avoid problems with matrix effects near the metal/semiconductor interface.

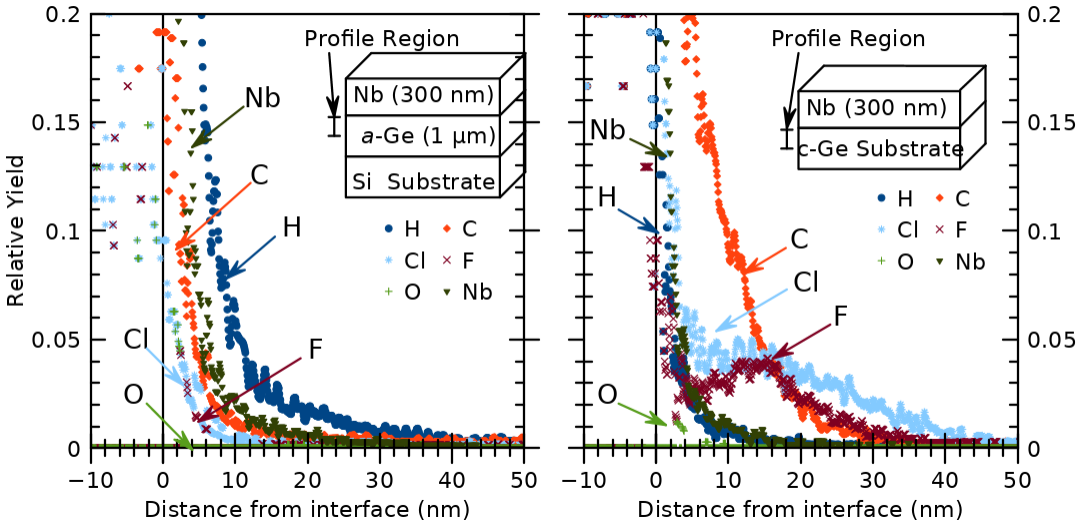

Figure 8: TOF-SIMS depth profiles showing uncorrected relative intensity for elements detected near the Nb/Ge interface (H, C, O, F, and Cl) beginning at 300 nm from the top surface (the depth of the Nb/Ge interface). The room-temperature deposited amorphous Ge (left) has very little interface contamination, with H the only other significant detection past 20 nm. The specimen deposited on single-crystal Ge wafer (right) has a significant interface C peak, F extending about 30 nm deep, with Cl extending about 45-50 nm into the Ge layer.

The 1 µm thick Ge layers evaporated onto Si (100) have an RMS roughness of 1.02 Å, measured by atomic force microscopy. Such low roughness topographies are necessary for strict device dimensioning and processing in multi-layer structures. These Ge films have another advantage for such applications. They have sufficient conductivity at room temperature to protect electronic devices, such as transistors and Josephson Junctions, from electrostatic discharge during fabrication and storage. Room-temperature deposited Ge films exhibit low loss and do not require elevated temperature thermal processing, enabling multi-layer resonator geometries for use microstrip and stripline microwave devices, as well as inter-wiring, isolation, and passivation layers. Although the magnetic properties of Ge have many advantages for all the applications discussed here, the natural form does contain a 7.8% abundance of ^{73}Ge, with 9/2

nuclear spin, which could potentially contribute to loss and noise in devices. Isotopically enriched ^{74}Ge is available and could be used to make thin films if the nuclear spin loss would contribute significantly to loss [63].

3.5 Conclusions

This investigation has demonstrated that deposited dielectrics in CPW resonators exhibit low loss when operated near single-photon powers and low temperatures of ~40 mK. CPW resonators on amorphous germanium films deposited at room-temperature have single-photon loss tangents of $1–2 \times 10^{-6}$, and CPW resonators on 9 μm thick high-purity CVD homoepitaxial silicon films have single-photon loss tangents of less than $0.6–2 \times 10^{-5}$. Interface losses presumably dominate the resonator performance in these devices.

These results show that room-temperature deposited amorphous Ge layers and CVD Si films exhibit microwave properties suitable for incorporation in quantum computing and sensing applications. The room-temperature deposited amorphous Ge layers could also be used to make co-planar, microstrip and stripline resonators, and could be utilized in place of the currently-used SiO_x and Si_xN_y for dielectric isolation, wiring, and passivation layers.

CHAPTER 4

SURVEY OF DIELECTRIC SUBSTRATES

Selecting germanium and high-purity epitaxial Si films for the investigation above began with a survey of available dielectric substrates to find those that exhibit low contamination and microwave loss. Each material was measured using the parallel plate resonator technique described by Taber [26], which was expanded in work by Shengke Zhang, et. al. [14]. This technique is performed by sandwiching a dielectric between two superconducting films of known surface resistance. This study uses Nb on Al_2O_3 films with known Rs~30 μΩ/□. The Nb/dielectric substrate/Nb film sandwich is then loaded into a microwave cavity with two coaxial probes near the edge. The microwave is sent into the structure through one probe and measured by the other probe. This entire cavity can be cooled by dipping into liquid helium to 4.2 K, or into a Quantum Design Physical Property Measurement System (QD-PPMS, San Diego, California), allowing for temperature control from 1.8 to 400 K with the possibility of applying field up to 9 Tesla for EPR.

The results of the PPR survey are described in Table 2, and find the substrates with the highest measured Q×f to be *a*-Ge deposited on Si and high-purity epitaxial Si on Si, as reported above, followed by $LaAlO_3$, MgO, GaAs, and Al_2O_3.

	0-1 Mode		1-1 Mode		0-2 Mode		2-2 Mode			
	Freq (GHz)	Q	Freq (GHz)	Q	Freq (GHz)	Q	Freq (GHz)	Q	**Avg ε**	Highest Q*f
MgO	5.24	20,300	7.61	35,430	10.3	8,010	14.9	56,950	8.1 ± 0.2	848,555
Quartz (SiO_2)	7.32	6,500	10.5	7,330	14.4	41,370			4.2 ± 0.1	595,728
CaF_2	6.28	16,420	9.15	30,750	12.23	9,940			5.7 ± 0.3	281,363
$CaCO_3$	5.65	25,690	8.25	5,390	11.23	15,120	16.14	18,120	6.9 ± 0.2	292,457
SiC			8.20	1,860	10.83	1,380	15.7	4,660	7.2 ± 0.5	93,713
$LaAlO_3$	5.48	54,570	7.27	45,280	10.7	43,480	14.1	84,830	8.2 ± 0.7	1,196,103
GaAs; n=10E+16					9.31	26,610	13.5	61,510	10.2 ± 0.3	830,385
12.5 micron Teflon	12.5	4,470	17.6	5,120					1.44 ± 0.01	90,112
Al_2O_3	4.96	48,380	7.23	26,080	11.95	6,461	14.09	64,330	8.3 ± 1.3	906,410
YSZ	5.52	7264	8.41	2596	10.43	5897	14.97	4533	7.5 ± 0.9	67,860
TiO_2	2.51	62990	3.83	56720	4.73	62440	5.53	96020	41±12	531,269
$KTaO_3$	4.54	2,653	4.88	3,184	5.03	3,428				17,243
a-Si/ FZ Si	4.85	46,150	7.09	20,600	10.9	21,500	15.42	57,500	8.4 ± 1.0	886,765
a –Ge / FZ Si							10.8	130,000		1,404,000

Table 2: PPR results for dielectric substrates. This table documents the resonant frequencies, measured dielectric constant, and QF factor for each material. Some materials showing high loss in these preliminary measurements were omitted from further study to avoid unnecessary patterning and device fabrication steps. Microwave PPR measurements here performed in collaboration with Shengke Zhang (unpublished work, 2014, printed with permission).

All substrates 1×1 cm^2. MgO (100) from MTI crystal. Quartz (SiO_2) (0001) from KJMT. C aF_2 (100) from MTI. $CaCO_3$ (001) from MTI. SiC 6-H, orientation unknown. $LaAlO_3$ (100) from MTI. GaAs semi-insulating from Wacker, 12.5 micron Teflon Taber [26]. $Al2O_3$ (0001) from Valley Design, YSZ (100) is Y_2O_3 stabilized ZrO_2, 8 % mole Y_2O_3 from MTI. TiO_2 (110) from MTI, $KTaO_3$ (100) from MTI. *a*-Si/FZ Si and *a*-Ge/FZ Si refer, respectively, to Si and Ge evaporated onto high-resistivity undoped float-zone refined Si at room temperature for this study.

Following the PPR survey, the *a*-Ge on Si film was measured at 6 K in magnetic fields up to 5000 Oe. No absorption peaks are visible, and field dependence is due to the niobium layers. The measurements of the *a*-Ge/Si and the Si standard show the same trends, indicating that measured losses in this region are due to magnetic field dependence of the Nb film, and not a result of paramagnetic loss in the *a*-Ge film.

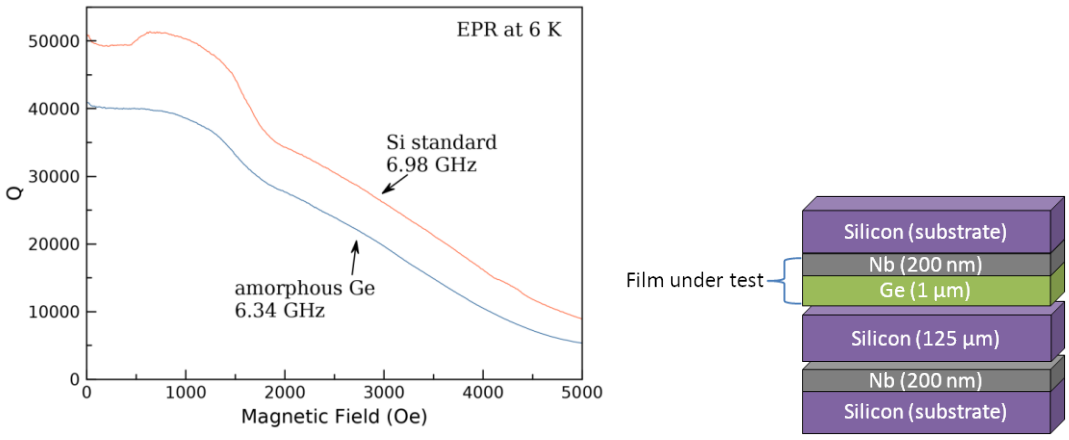

Figure 9: (left) Electron paramagnetic resonance (EPR) measurement for amorphous deposited Ge film at the T_{01} resonance mode, compared to undoped Si between two Nb films. (right) film stack diagram for electron paramagnetic resonance measurements. This work was performed in collaboration with Justin Gonzales, unpublished work, 2020, and included with permission.

Identification of chemical contaminants in dielectric substrates was also performed using PIXE and HeIXE, with results documented in Table 3. Specimens were analyzed using incident α—particle and proton beams at 2.0 and 3.0 MeV to detect a wide range of light and heavy contaminants. PIXE was performed at atmospheric pressure, with a Mylar window over the x-ray detector, while HeIXE is performed in the 10^{-8} Torr range without any x-ray attenuation window.

HeIXE and PIXE do not find any contaminants in Si, Ge, or GaAs, but find evidence of impurities in Al_2O_3, MgO, and $LaAlO_3$.

Substrate Measured	PIXE detection	HeIXE detection	comment
MgO (100)		Ca (<700 ppm)	
Quartz (SiO_2) (0001)	-	K (1700 ppm)	
CaF_2 (100)	-	N (<300 ppm)	
$CaCO_3$ (001)	P	-	
SiC (6-H)	-	-	
$LaAlO_3$ (100)	Cr <3000 ppm	Na	
GaAs		-	
Al_2O_3 (0001)	-		*purple/red fluorescence could indicate Cr impurity
YSZ from MTI		Hf (7500 ppm)	
TiO_2		*	*unidentified peak
$KTaO_3$ (MTI)		Mg (1300 ppm)	
Ge (100)	-	-	
High-purity Epi Si on FZ Si	-	-	
Epi Graded Si-Ge on FZ Si	-		
GaN (CVD GaN on Al_2O_3)	-	-	*yellow/green fluorescence could indicate Ga vacancy or C
Si (FZ high-ρ Substrate)		-	

Table 3: Table of results for PIXE and HeIXE scans of dielectric substrates. A dash indicates no detection (other than the expected substrate elements) was observed, blank cells indicate no measurement was performed.
All substrates 1×1 cm^2. MgO (100) from MTI crystal. Quartz (SiO_2) (0001) from KJMT. C aF_2 (100) from MTI. $CaCO_3$ (001) from MTI. SiC 6-H, orientation unknown. $LaAlO_3$ (100) from MTI. GaAs semi-insulating from Wacker. $Al2O_3$ (0001) from Valley Design, YSZ (100) is Y_2O_3 stabilized ZrO_2, 8 % mole Y_2O_3 from MTI. TiO_2 (110) from MTI, $KTaO_3$ (100) from MTI.

X-ray Topography, XRT, was performed on two interesting commercial substrates from this investigation, high-purity epitaxial Si on float-zone Si, and a graded concentration Si→$SiGe_x$ film on Si where the concentration of Ge is varied from 0 to 30%

over the 3 μm thickness, shown in Figure 10. These are expected to be very chemically pure, but potentially may have extended defects because of strain or non-ideal deposition techniques. These specimens were measured in XRT transmission mode, where the technique has a resolution of ~50 μm. A high-quality crystalline Si substrate is also scanned as a control.

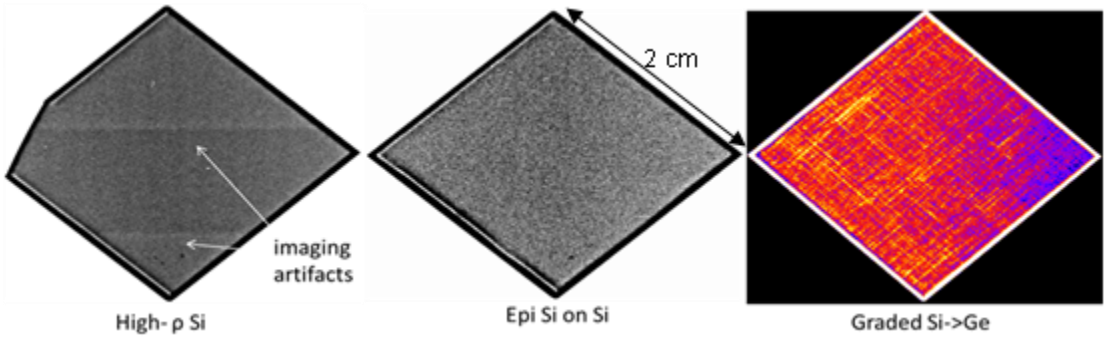

Figure 10: XRT scans for 2x2 cm specimens (left) high-resistivity float-zone Si substrate, (center) epitaxial Si/Si, and (right) graded Si→SiGe on Si. The bare substrate (left) shows two horizontal lines that are a result of imaging artifacts on the film. This specimen was also taken from the edge of a wafer, so it is not a full square. The image (right) is a false-color image to better show contrast on threading dislocations.

The XRT results, do not detect any extended defects either in the control silicon substrate or in the epi Si/Si. The graded Si→SiGe specimen shows a high concentration of dislocations in the {010} directions. These show up as bright lines in the inverted false-color image. From the high concentration of defects in this specimen, poor microwave properties are expected, so no further investigation of the graded Si→SiGe films were made.

The amorphous Ge films used in the study above were measured electrically to determine electronic carrier concentrations. Indium contacts were formed at the four corners and annealed in Ar at 260 °C for 20 minutes to form a van der Pauw

configuration. Figure 11 shows the measured resistivity vs. temperature. The room-temperature resistivity of ~5 Ω-cm corresponds to a carrier concentration less than 10^{15} cm^{-3}, and this resistivity quickly increases with decreased temperature. Hall measurements performed at room-temperature measure a carrier concentration of $\approx 10^{14}$ cm^{-3}, but with high uncertainty due to small Hall voltages near the measurement limit.

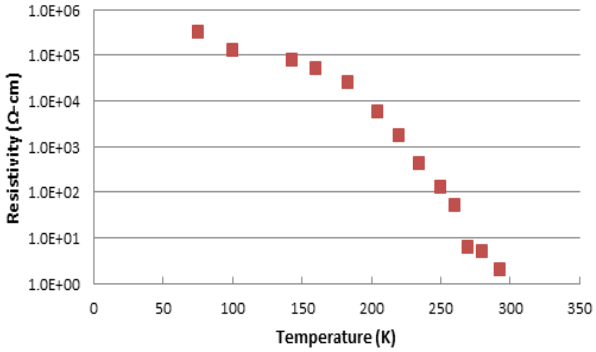

Figure 11: Measured resistivity vs. temperature for a ~1 μm thick *a*-Ge on Si film deposited at room-temperature, corresponding to a net carrier concentration $<10^{15}$ cm^{-3}.

X-ray diffraction is used to identify the structure of Ge films deposited on Si substrates. The XRD patterns in Figure 12 compare Ge on Si films deposited without substrate heating, and with substrate heated to 400° C. In the low temperature deposited *a*-Ge film, a small, unidentified diffraction peak is observed near 44°, likely attributed to the substrate, and broad peaks appear below 30°, characteristic of amorphous films. Once the deposition substrate temperature is increased to 400° C, the deposited Ge film exhibits polycrystalline characteristics with grains oriented with the (220) and (111) perpendicular to the film surface.

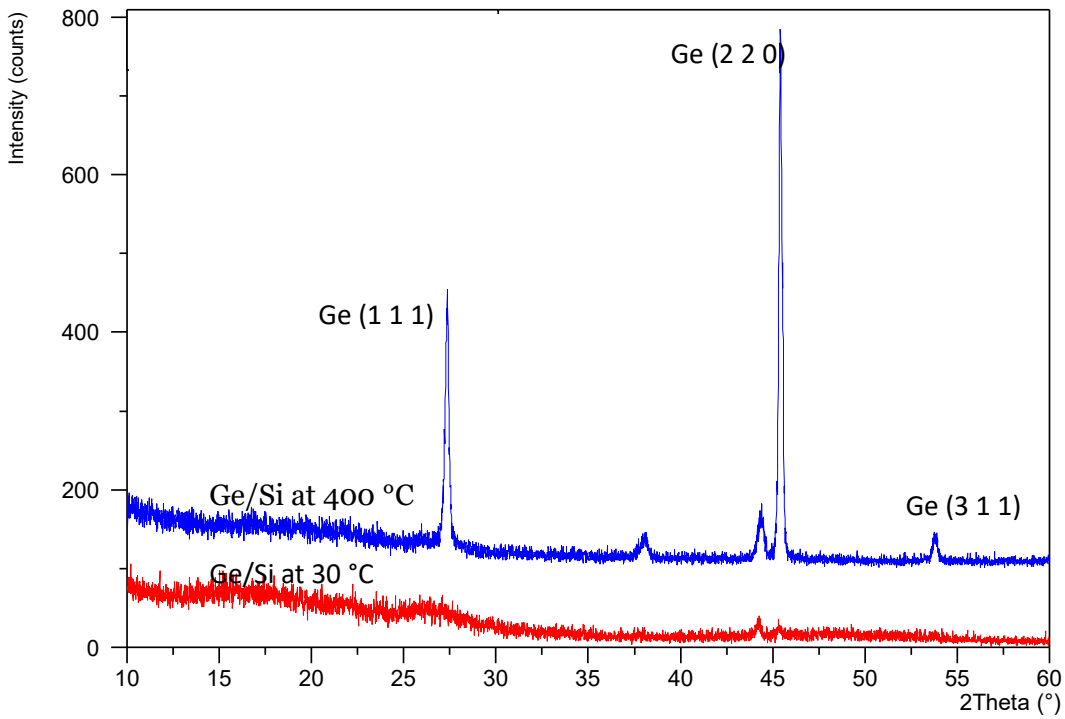

Figure 12 X-ray diffraction of Ge on Si evaporated onto an un-heated substrate (bottom curve, red line), and a substrate with temperature of ~400° C (upper curve, blue line). The high temperature deposition shows polycrystalline behavior, while room-temperature deposition appears to be mostly amorphous with only some weak evidence of crystalline peaks.

CHAPTER 4

TANTALUM DIFFUSION BARRIER LAYERS

4.1 Abstract

Germanium thin films are an excellent candidate for use as a low-loss dielectric in superconducting microwave resonators, and as low-loss device isolation, inter-layer metal wiring dielectric, and passivation layers in microwave and Josephson junction devices. In Ge/Nb structures deposited at 400 °C, interface intermixing occurs over as much as 20 nm. The addition of a 10 nm Ta diffusion barrier layer reduces superconductor/dielectric intermixing to less than 5 nm and enhances the structural properties of deposited Ge layers, as judged by Raman spectroscopy measurement results. Additionally, superconducting microwave resonators fabricated at room-temperature on crystalline Ge substrates with a Ta barrier layer show marked improvement in total and two-level system power-dependent, microwave losses.

4.2 Introduction

Germanium has many properties that make it appealing for use as an insulating dielectric for low-temperature superconductor devices. Germanium can be produced with impurity concentrations as low as 10^8 cm^{-3}, lower even than silicon. Room temperature deposition yields amorphous Ge films, while deposition at elevated temperatures can form polycrystalline and epitaxial films. While undoped Ge has immeasurably low conduction below 50 K, Ge has sufficient conductivity at room

temperature to protect against electrostatic discharge during device fabrication and storage. It can be deposited via evaporation, sputtering, or vapor techniques.

At low temperatures of 40 mK and near single-photon microwave flux, power-dependent, two-Level System losses at the metal-air, metal-dielectric, and dielectric-air interfaces[9][7] limit the performance of superconducting microwave devices such as Co-Planar Waveguides, CPW, and Kinetic Inductance Detectors, KIDs. The losses observed under these conditions are termed Two Level System or TLS losses.

In Chapter 3, very low Two-Level System losses with a tan δ_o of 1.3×10^{-6} were measured for Nb/amorphous-Ge thin-film resonators produced without substrate heating. Further investigations of Nb/Ge indicate that device properties can be improved by growing at temperatures that promote crystallization of ~400 °C for Ge on Si [64], but only when the effects of interfacial intermixing could be reduced or eliminated. The use of the compound superconductors TiN and NbTiN when deposited on Si or Al_2O_3 [65][66] were found to reduce interdiffusion into the substrate. A search of the literature did not return any studies involving diffusion barriers for Nb-layers fabricated on Si or Ge.

Tantalum is often used as a diffusion barrier in semiconductor technology and should be considered for use in the Nb/Si system for the following reasons. It is refractory in nature, has the same body-centered cubic crystal structure as Nb, and has a 0.03% lattice mismatch to niobium (i.e., a_{Nb}= 330.04 pm, a_{Ta}= 330.13 pm). The 4.4 K Ta superconducting transition temperature is lower than that for Nb, 9.2 K, but a 10 nm barrier layer with a thickness thinner than the coherence length for ξ_{Ta}~95 nm and ξ_{Nb}=38 nm will not significantly degrade the T_C of a Nb/Ta bilayer. In the clean limit and assuming no reflection at the interface, the expected T_C of a Nb(200 nm)/Ta(10 nm) bilayer is higher than 8.6 K [67]. Furthermore, microwave device studies of Nb and Ta

coplanar microwave resonators indicate that similarly prepared devices do not differ in phase noise when measured at the same relative temperature, T/T_C [68].

Chemical intermixing of 10-20 nm occurs when niobium is sputtered onto crystalline silicon at room-temperature. Similar levels of intermixing occur at the Nb/Ge interface. This study aims to reduce diffusion at the niobium-germanium interface, and compare relative structural qualities of amorphous and polycrystalline Ge layers deposited on Nb and Ta layers.

4.3 Experimental Parameters

All film depositions for this study take place in a cryopumped (CTI Cryogenics, CTI-8, Austin, TX) unbaked UHV vacuum system with a base pressure of less than 2×10^{-9} Torr. Substrates used in this study are float-zone Si (100) cleaned ultrasonically for 10 minutes each in USP-grade acetone and then ethanol. The solvent clean is then followed by a 5 minute etch in 2% HF. Niobium and tantalum are deposited via magnetron sputtering from 2" targets with 99.95% purity. Germanium substrates and source for evaporation material are undoped zone-refined Ge (100) with stated resistivity higher than 40 Ω-cm. Germanium is evaporated from a Knudsen-type effusion cell. Sputter deposition is performed after evacuating the chamber to the base pressure, which is then backfilled to 4 mTorr of 99.9999% Ar. Source-substrate distances are about 15 cm; the deposition rate is ~6 Å/second for Nb to a thickness of ≈300 nm and ≈4 Å/second for Ta to at thickness of 10–15 nm. After sputtering, germanium film deposition starts after evacuating the chamber to below 8×10^{-9} Torr, and the germanium film is deposited with a Knudsen cell heated to 1400 °C at a rate of 2 °C/minute. This results in a deposition rate of ~2.4 Å/s and a total Ge thickness of 1 μm.

Transmission Electron Microscopy, TEM, specimens are prepared by manual "rod and tube" preparation to avoid intermixing associated with Focused Ion Beam, FIB, techniques. Specimens are bonded with epoxy inside a brass support structure, diced into thin cross-sections, mechanically polished down to less than 100 μm thickness, thinned to a few μm thick in the center using a dimple grinder, and polished to electron transparent thicknesses using a Precision Ion Polishing System, PIPS, mill. High-resolution TEM uses an aberration-corrected Jeol ARM-200F with in-situ Energy Dispersive X-ray Spectroscopy, EDS, and an attached AppFive precession electron diffraction system.

Raman spectroscopy was performed with a 532 nm laser operating at 0.75 mW, with a 0.5 μm spot size. X-ray Diffraction was carried out using a PANalytical X'pert MRD Pro with Cu-K_α radiation.

Superconducting Co-Planar Microwave Waveguide resonator, SCPW, were fabricated with standard photolithography techniques and CF_4 reactive ion etching. The SCPW was designed for 5.8 GHz resonance using 4-μm trace widths, and a 2-μm gap. These narrow trace widths and minimal over etch of less than ~20 nm increase interface sensitivity of the measurements so that interface properties can be investigated. Wider widths and gaps are used to maximize the quality factor of practical devices. Resonator measurements identify the total microwave loss, tan δ_i, and the power-dependent TLS losses, tan δ_o.

4.4 Results and Discussion

Ge films were evaporated onto 300 nm on sputter-deposited Nb on Si substrates at 400 °C to determine the depth of the temperature-induced intermixing. The bright-field TEM micrograph in Figure 13-a shows the interface between Ge evaporated at 400

°C and the Nb film underneath. Niobium films sputtered at room temperature onto Si substrates typically exhibit tall columnar grains through the entire 300 nm thickness with a diameter of ≈50 nm. Lattice planes extending across the interface, as illustrated with the with light-colored Ge on the top and dark Nb on the bottom, indicate regions of intermixing. This intermixing is visible over at least 5-10 nm and shows that the interface is not atomically abrupt as. Precession diffraction (Figure 13-b) measurement results show that the film is comprised of ≈50 nm wide, 150 nm tall Ge grains, on the average. This is determined using the lineal intercept method, with n=11. Smaller grains are consistently observed near the interfaces and finds an average grain diameter 49 Å. Analysis of XRD and TEM results both find that the deposited Ge layer is polycrystalline with Ge (111), (220), and (311) planes oriented perpendicular to the (110)-textured Nb surface.

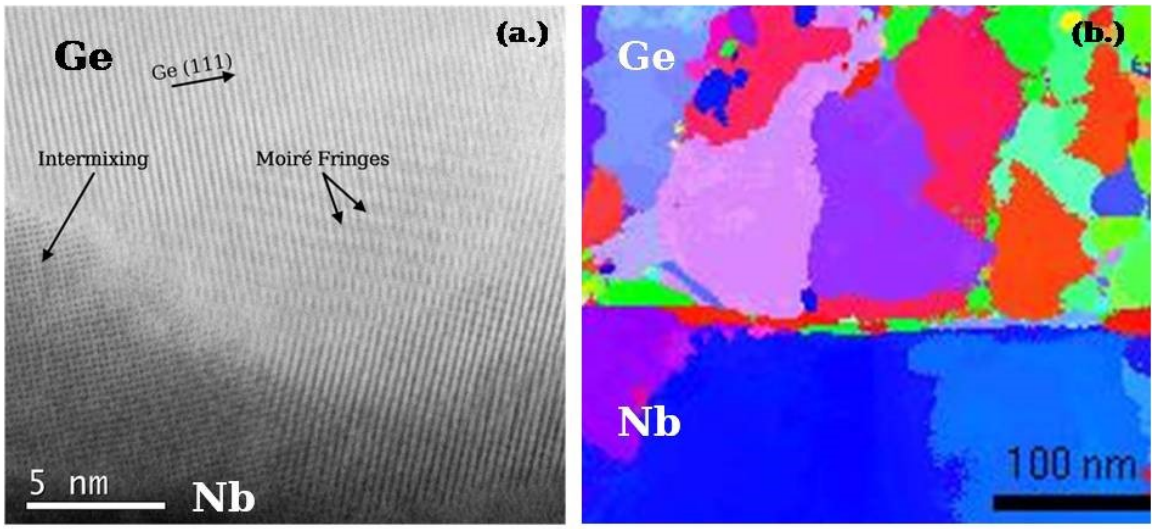

Figure 13 **(a.):** High-resolution bright-field STEM image showing the Ge-Nb interface for Ge (400 °C) on Nb sputter-deposited on Silicon substrate. This figure shows intermixing and alloying at the interface over at least 5-10 nm. Multiple grains through the specimen thickness cause the Moiré fringes in the center of the image. **(b.):** Precession diffraction across the Nb/Ge interface showing a colorized grain contrast of the Ge layer deposited onto Nb at 400° C. The Ge grains exhibit a "tall" 1:2 shape factor and are preferentially oriented with Ge (111), (220), and (311) perpendicular to the surface.

The extent of intermixing is quantified using Energy-Dispersive X-ray Spectroscopy, EDS, line profiles shown in Figure 14, which find that the Ge evaporated at 400 °C directly onto Nb at 400 °C exhibits as much as 20 nm of intermixing between the Nb and Ge layers. In contrast, a Ge layer deposited onto a 10 nm Ta-buffered 300 nm Nb on Si structure at 400 °C has less than 5 nm of intermixing at the Ge/Ta interface. This is approximately the EDS spatial resolution due to estimated beam broadening. This result shows that Ta is an effective diffusion barrier in other niobium-dielectric material systems. The TEM images in Figure 14-b also show that Ta has a surface roughness of about 5 nm, which is not significantly different from that observed for Nb/Ge samples prepared without a buffer layer.

The relative structural quality of amorphous room-temperature grown and 400 °C grown polycrystalline Ge films is inferred by comparing the Raman peak shift and Full-Width Half Maximum, FWHM, of the Ge T_{2g} TO mode shown in to a reference Raman spectra of undoped single-crystal Ge (100), as shown in Figure 15. Germanium deposited on a Ta diffusion barrier has smaller strain-induced [69] Raman energy shifts from the reference peak value and FWHM in both amorphous and polycrystalline films. The narrower FWHM of the Ge layers deposited on Ta buffer layers is indicative of a higher structural quality film with a longer phonon lifetime. Based on these results, Ge films deposited on Nb with a Ta diffusion barrier layer are of relatively higher crystalline quality. The lower-intensity broad Raman peaks observed for the amorphous films are similar to those found in electrolytically deposited *a*-Ge [58].

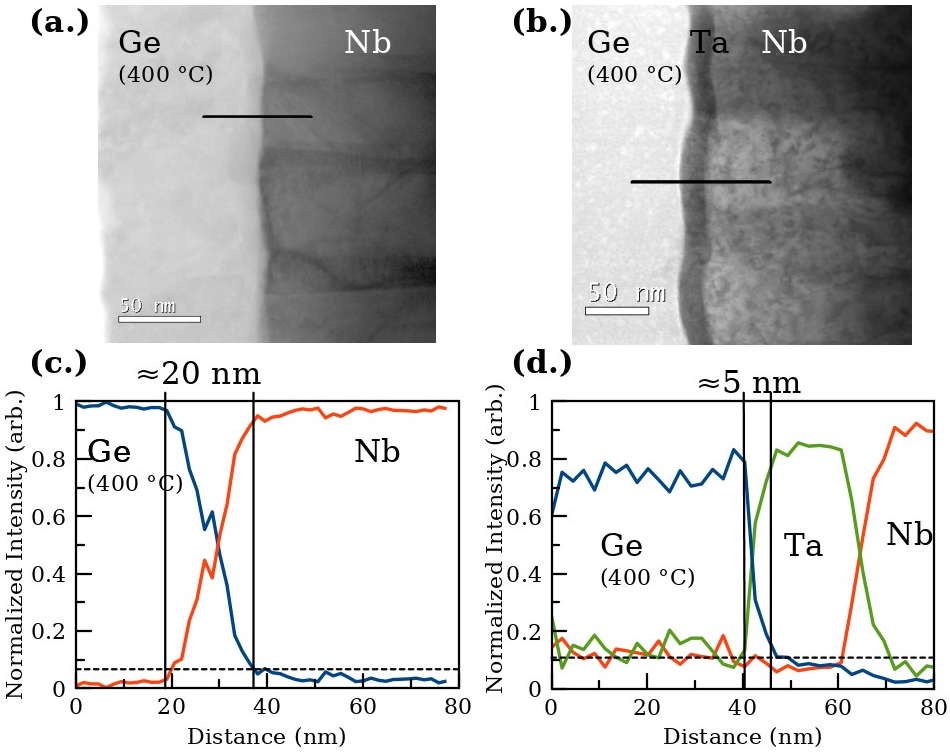

Figure 14 **(a.)** Ge/Nb interface for Ge evaporated onto Nb at 400 °C, showing an area of different contrast near the interface related to intermixing. The black line corresponds to approximately the region of the EDS Line profile. **(b.)** The Ge/Nb/Ta interface where Ge was evaporated onto a Ta/Nb film at 400 °C. The tall columnar grain structure of the niobium and tantalum is visible, and contrast differences from the bottom to the top of the Nb grains are due to variable specimen thickness. Ta grows with grain structure matching that of Nb, without enhanced surface roughness. The black line corresponds to approximately the region of the EDS Line profile. **(c.)** The results of an EDS line profile across the Ge/Nb interface, marked by the line in (a.) and showing ~20 nm of Ge/Nb intermixing. **(d.)** The results of an EDS line profile across the Ge/Ta/Nb interface, from the region marked by the line in (b.), showing ~5 nm of Ge/Ta intermixing, near the EDS probe resolution of 1.5 nm. The dotted lines correspond approximately to the EDS background.

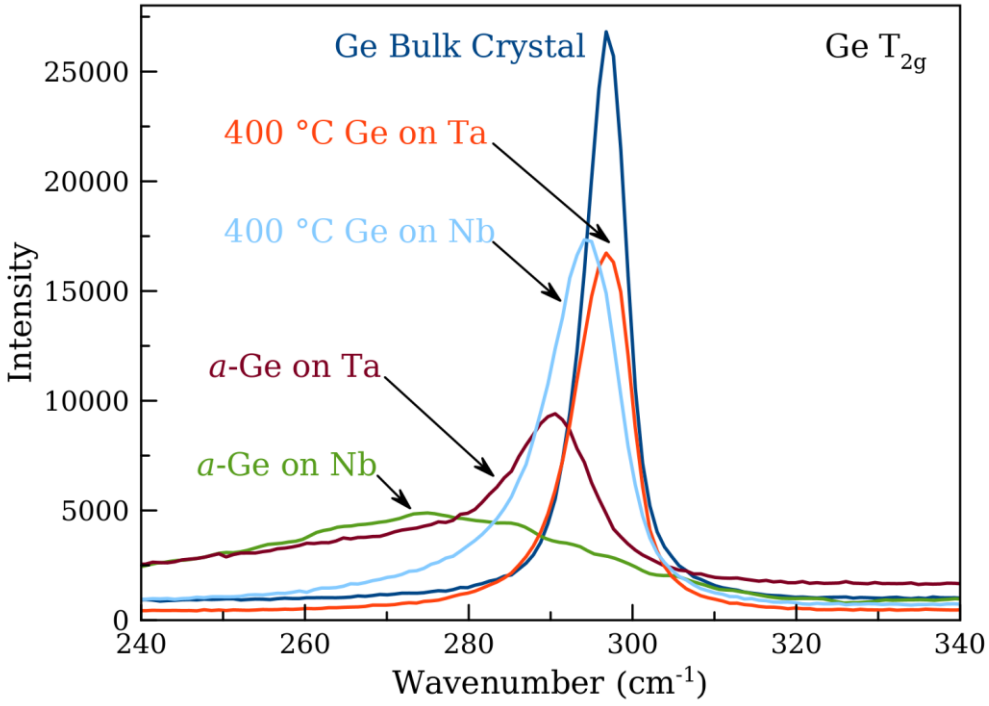

Figure 15: Raman Spectroscopy of Ge TO mode for Ge deposited on superconductor films compared with a crystalline (100) Ge substrate. The Ge on Ta film deposited at 400 C exhibits a peak position closest to that of bulk single-crystal material.

The temperature dependence of the Nb resistivity is strongly affected by scattering from both native and impurity defects. The resistivity vs. temperature characteristics of a Nb/Ta/Ge(400 °C)/Ta/Nb/Si, as shown in Figure 16, are dominated by the resistance of the top Nb layer. We find a T_C of 9.2 K and a Residual Resistivity Ratio, RRR, of 6.6. From this, we can infer a mean free path, λ, of 70 Å at 10 K using the Sommerfeld model, indicating a low defect concentration and no depression in T_C from the Ta layer.

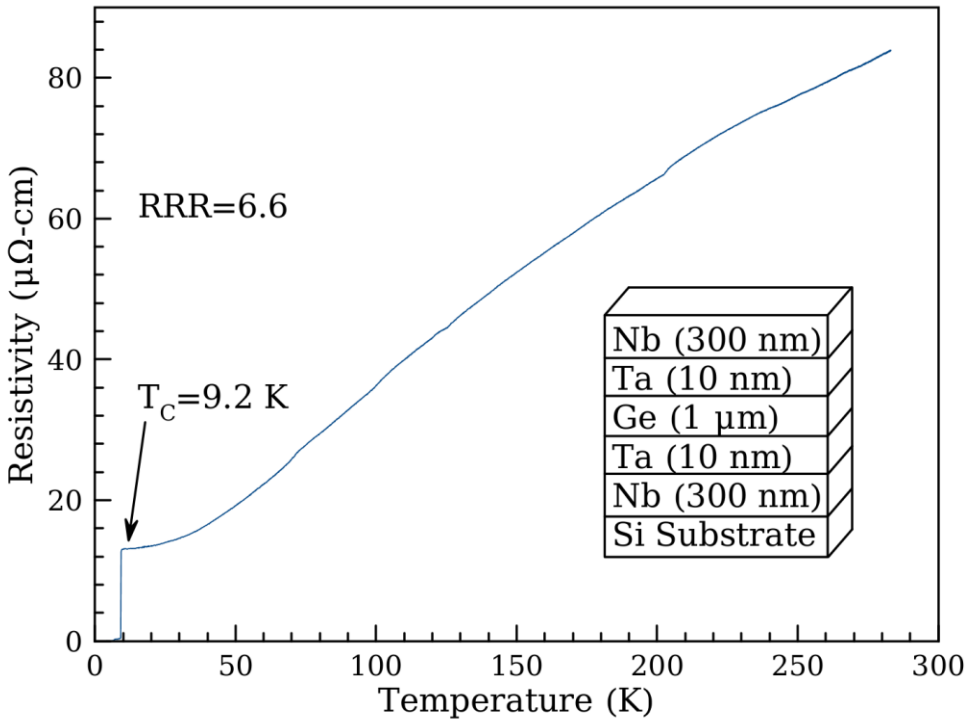

Figure 16: Resistivity vs. temperature measurements measured via 4-point probe on the top surface of a Nb(300 nm)/Ta (10 nm)/Ge (1 μm)/Ta (10 nm)/Nb (300 nm)/Si substrate structure with Ge deposited at 400° C. Superconducting transition temperature for the stack is T_C=9.2 K, and RRR=6.6.

Microwave results illustrated in Figure 17 measured at 40 mK and near single-photon powers of Nb (200 nm)/Ta (10 nm)/undoped single-crystal Ge resonators exhibit total loss tan δ_i of 4.92×10^{-5} and power-dependent two-level system, TLS, tan δ_o of 4.92×10^{-5}. Each loss value is lower than corresponding loss values for Nb directly on crystalline Ge, as reported for similarly prepared devices in Chapter 3, of tan δ_i of 7.53×10^{-5} and tan δ_o of 6.1×10^{-5}. These measurements suggest that reduced intermixing improves the performance of microwave resonators.

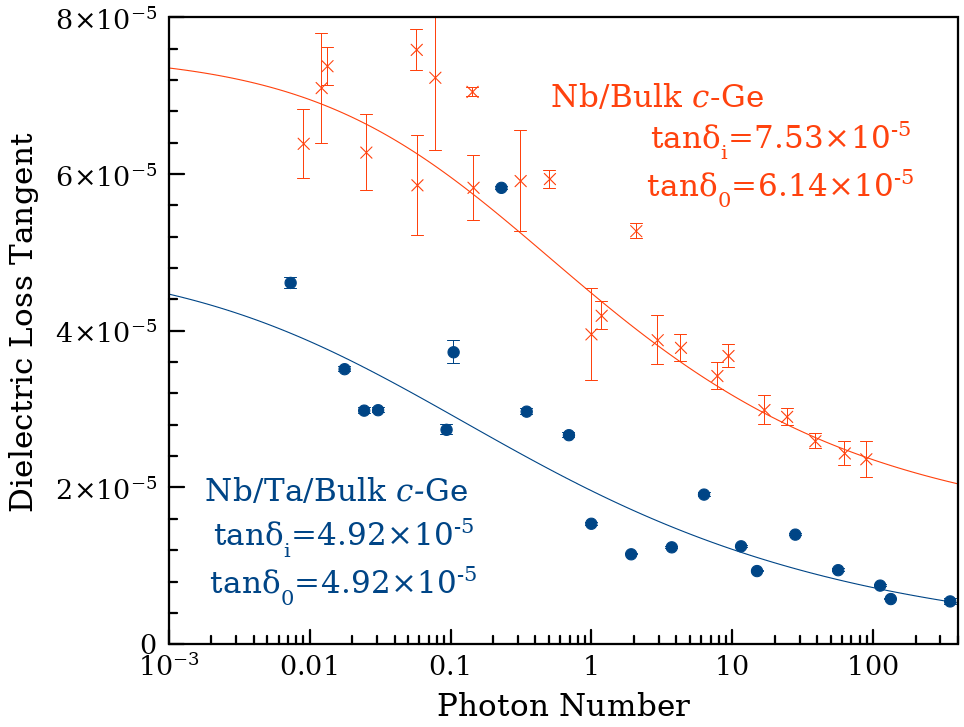

Figure 17: Total dielectric loss tangents (tan δ) measured at low temperature and low power for patterned SCPW devices of niobium on undoped single-crystal Ge wafers with and without Ta diffusion barriers. The Nb (200 nm)/ Ta (10 nm) structure on has total loss tan δ_i=4.92×10^{-5} and power-dependent loss tan δ_o=4.92×10^{-5}. The Nb (200 nm) directly on single-crystal Ge (presented earlier in Chapter 3**)** has total loss tan δ_i=7.53×10^{-5} and power-dependent loss tan δ_o=6.14×10^{-5}

4.5 Conclusions

This study has demonstrated that a Ta diffusion barrier between Nb and Ge decreases intermixing, improves microwave loss properties, and improves the structural quality of deposited Ge films. The Ta diffusion barrier reduces interface intermixing between Ge and Nb from ~20 nm to less than 5 nm in structures fabricated at temperatures at 400 °C. Low-temperature of 50 mK and low power measurements of SCPW resonators deposited on crystalline Ge wafers have a tan δ_o of 4.92×10^{-5} and tan δ_i of 4.92×10^{-5} with Ta-diffusion barrier, and without a barrier tan δ_i of 7.53×10^{-5} and tan δ_o of 6.14×10^{-5}. This indicates that the improved TLS and total microwave loss properties can be attained with the use of a Ta diffusion barrier layer. The amorphous high-purity Ge layers deposited at room temperature have a small surface roughness of 1.02 Å RMS. The results of this study suggest that the use of Ge layers with a Ta barrier layer can enable the production of improved high-Q, low TLS loss coplanar, microstrip, and stripline resonators, as well as low-loss device isolation, inter-wiring dielectrics, and surface passivation layers in passive microwave and Josephson junction circuit fabrication.

CHAPTER 5

CHARACTERIZATION OF THE CHEMICAL AND ELECTRICAL PROPERTIES OF DEFECTS AT THE NIOBIUM-SILICON INTERFACE

5.1 Abstract

The nature and concentration of defects near niobium-silicon interfaces prepared with different silicon surface treatments have been characterized using current-voltage (I-V), Deep Level Transient Spectroscopy (DLTS), and Secondary Ion Mass Spectroscopy (SIMS). All samples have H, C, O, F, and Cl chemical contamination in the Si within 50 nm of the interface and electrically active defects with activation energies of 0.147, 0.194, 0.247, 0.339, and 0.556 eV above the valence band maximum, E_{vbm}. In all cases, the deep level defect concentration is dominated by the hole trap at E_{vbm}+0.556 eV, which can be associated with a Nb point defect in Si, presumably Nb_{Si}. This defect is present with a concentration of 7×10^{13} cm^{-3} for the HF etch and 100 eV ion mill surface clean to the highest density of 5×10^{14} cm^{-3} for the RCA surface clean.

The optimum surface treatment used in this study is an HF surface etch followed by an in-situ 100 eV Ar-gas ion milling process. Higher energy ion milling is found to increase the electrically active Nb defect concentration in the Si, and increase concentration of defects at E_{vbm}+0.339 and E_{vbm} +0.247 eV. The HF etch alone removes O from the interface, but results in significant H and F contamination, electrically-active point defect concentrations, and levels of Shockley-Reed-Hall recombination (i.e., Nb/Si Schottky diodes with an ideality factor, n, of ≈1.6). The RCA clean increases the depth and concentration of H, F, C, and Nb contamination.

5.2 Introduction

Superconducting electronic devices circuits and systems commonly use niobium as the superconductor because of its relatively high 9.2 K superconducting transition temperature and relative ease in depositing high-quality thin-films. For applications that require ultra-low noise, including quantum computing, sensing, and information systems, undoped zone-refined Si substrates are most commonly used because of their wide availability and purity. Superconducting coplanar microwave resonators are an example of a device that uses this system at sub-Kelvin temperatures and single-photon levels to achieve minimal noise. However, in these devices, defect-induced microwave loss at the metal-dielectric interface is often the dominant "two-level-systems" noise source [48][53] [10]. While surface engineering [70][71] and removal of residue from microfabrication [72] can decrease this loss, the physical nature of the defects responsible for these losses is still unknown. This chapter will identify the chemical and electrical properties of defects present at niobium-silicon interfaces, and identify their physical nature when possible, using characterization techniques developed by the semiconductor industry.

In this study, time-of-flight secondary ion mass spectrometry, SIMS, has been used to measure the depth profile of contaminants and the level of intermixing at and near the Nb-Si interface. Rutherford Backscattering Spectrometry, RBS, and nuclear reaction analysis, NRA, are performed to determine layer thicknesses and concentrations. Current-voltage, I-V, and capacitance-voltage, C-V, profiling techniques identify changes in doping profile, barrier heights, the presence of Shockley-Reed-Hall recombination, interfacial oxide layers, and surface leakage currents. Deep level transient spectroscopy, DLTS, further adds to these techniques, identifying

concentrations, energy levels, capture cross-sections, and depth profiles of defects within the depletion region, and has the ability to determine the physical nature of the electronic defect by comparing to known electronic levels and capture cross-sections.

5.3 Experimental Parameters

1 × 1 cm^2 p-type Si with 7-8 μm epitaxial B-doped (8×10^{16} cm^{-3}) on 500 μm B-doped 5×10^{19} cm^{-3} substrates were used. The top epitaxial Si layer is chosen with low enough doping concentration to make a low-leakage Schottky junction, while the base substrate is highly doped to reduce series resistance. Sequential substrate cleaning procedures were performed, and then the specimens were loaded into the vacuum deposition chamber within 180 seconds to minimize contamination and oxidation of the surfaces.

The “solvent only” cleaned substrates are immersed in acetone in an ultrasonic bath for 9 minutes, then in USP-grade anhydrous undenatured ethanol for 9 minutes. “HF etch” sample processing follows the solvent clean with a 5-minute immersion in HF (2 vol% aqueous), after which the HF is shaken off the sample without rinsing the surface to minimize organic contaminants. An ion milling process using a5-cm Kauffman ion source at 60 eV Ar ion energy, 2 mA current for 2 minutes is then performed in-situ before the final Nb deposition for “ion mill” specimens. For the “RCA cleaned” specimens, RCA clean “SC-1” and “SC-2” steps [73] are inserted before HF etch and ion milling; these consist of 10-minute immersion at 70 °C in $NH_4OH + H_2O_2$ to remove organic residue, followed by 10-minute immersion at 70 °C in $HCl + H_2O_2$ to remove metal contaminants and form an oxide layer. The RCA clean procedure is followed by the

same 5-minute HF etch (2 vol% aqueous) to remove the oxide layer, then 2-minute in-situ ion milling process with Ar ions, 60 eV, 2 mA before Nb deposition.

Niobium is deposited via magnetron sputtering in an un-baked cryo-pumped Ultra-High Vacuum (UHV) chamber with base pressure less than 2×10^{-9} Torr. Source to substrate distance is ≈15 cm, with the Nb deposition rate ~0.6 nm/second and a total film thickness of typically ≈200 nm. The device area is defined using a metal shadow mask to minimize confounding experimental effects such as etch damage or contamination from photolithographic processing. The device areas include 1 × 1 mm^2 squares for I-V and DLTS measurements, and a 2 mm diameter circle for the TOF-SIMS depth profile. This sample configuration meets experimental requirements for both chemical and electrical characterization on the same specimen to avoid run-to-run variation.

Ohmic contacts are prepared on the back-side of the 5×10^{19} cm^{-3} boron-doped substrate immediately after removing the sample from vacuum by scratching the rough side of the film with a diamond scribe to break through the silicon oxide layer, then applying two pads of silver paint (SPI, Model Silver Conductive Paint, West Chester, PA) on an approximately 3 × 8 mm^2 area. The silver paint is then cured at room temperature overnight. Room-temperature I-V measurements across the two back-side contacts are performed to confirm the contacts are Ohmic (i.e., linear and non-rectifying), and the large back-side contact areas are used to ensure that the device capacitance is limited by the size of the 1 x 1 mm^2 Nb-Si Schottky barrier on the top surface.

TOF-SIMS depth profiling is performed with a Time of Flight Secondary Ion Mass Spectrometer (ION-TOF USA, Inc., Chestnut Ridge, NY). Negative secondary ions are monitored using a ^{69}Ga primary analysis beam and Cs sputter beam at 1 kV, in an un-

baked vacuum chamber with base pressure less than 2×10^{-9} Torr. The relatively low 1 kV sputter energy minimizes beam intermixing and increases depth resolution; however, the low sputter rate (1.5 seconds/Å) increases the background signal from re-deposition. TRIM [38] simulation estimates about 2 nm of intermixing induced by the Cs beam at this energy, ignoring cascade effects from repeated sputtering; the experimentally-realized interface resolution is about 5 nm. SIMS sensitivity factors are only available for bulk Si [74], and since ionization potentials and charged-particle sputter yields can differ by orders of magnitude from those values in the highly intermixed interfacial Nb/Si region, all SIMS data in this volume are presented as secondary ion yield values normalized to the relative count rate of the host matrix (Nb or Si).

Rutherford Backscattering Spectrometry and nuclear reaction analysis (NRA) use a 1.7 MV Tandetron accelerator (5.1 MeV maximum energy) with α-particles at 2.0 MeV (for RBS), 3.05 MeV for oxygen NRA, and 3.58 MeV for carbon NRA. Both RBS and NRA have a sensitivity of ~0.01 at% in a thick layer, and a depth resolution of ~5 Å.

In this investigation, devices are electrically characterized using Current-Voltage (I-V) measurements using a picoammeter with internal voltage source (Hewlett-Packard Model 4140B, Palo Alto, CA), and Deep Level Transient Spectroscopy (DLTS) using a Semilab time-resolved capacitance meter (DLTS Model DLS-83, Budapest, Hungary). DLTS measurements were performed using a 20 μs filling pulse time, with rate windows ranging from 25-125 Hz, a reverse bias of 1 V and a forward bias of +1.1 V to fill defects near the Nb/Si interface. A cryogenic cold stage refrigerator with a 50-350 K temperature range (Cryosystems Model LTS-21, Westerville, Ohio) cools the specimens for temperature profiling. For the DLTS measurements, the diodes are driven into reverse bias to empty traps, then a forward bias pulse fills traps, and the time-dependent

change in capacitance is measured and related to the emission rate of the activated traps. Temperature spectrums are recorded at different rate windows (measurement frequencies), generating frequency-temperature data for each peak with the intensity corresponding to the emission rate and concentration. An Arrhenius plot of these peak positions in Temperature, T, and emission rate, τ_e, is fit to the equation $\tau_e T^2 = \frac{\exp\left(E_T/k_B T\right)}{\gamma\sigma}$ to obtain the energy level from the band (E_T) and capture cross-section (σ) using the constant $\gamma = 1.78\times10^{21}$ $cm^{-2}s^{-1}K^{-2}$ for p-type Si [39]. After identifying frequency-temperature pairs for specific energy levels, depth profiles are performed by setting the temperature and frequency to a constant value and then apply two excitation pulses with varying periods a set time apart to define the width of the space charge region. When possible, the physical origin of the defect is determined by comparing measured activation energies and capture cross-sections to those in the literature, keeping in mind what chemical species are present in the region as measured by the TOF-SIMS measurements.

5.4.1 Chemical Characterization of Interfaces

The Time-Of-Flight Secondary Ion Mass Spectrometry (TOF-SIMS) profiles in Figure 18 provide high depth and mass-resolution chemical depth profiles across the niobium-silicon interfaces. This investigation focuses primarily on the contaminants near the interface in the Si layer since they are presumed to be responsible for the microwave losses [48]. In all specimens, TOF-SIMS identifies interfacial and near-interfacial contamination from hydrogen, carbon, oxygen, fluorine, and chlorine, likely remaining from substrate processing. TOF-SIMS reports only chemical contaminants and does not distinguish those that may be electrically inactive in Si. However, identifying chemical species can help identify sources of contamination, and help identify the origin of electrical defects measured with DLTS.

Because TOF-SIMS does not allow for easy quantification of interface contaminants, RBS and NRA were used to set an upper limit for interface contamination. In the "solvent only" specimen, RBS finds about 10 nm of SiO_2 at the interface, but all subsequent surface clean techniques remove SiO_2. For all other samples, there are not any contaminants observed in the Nb layer or the Si substrates to within the 0.01 at% detection limit of RBS. Since RBS and NRA have been established to be highly accurate and do not require a standard, it sets an upper limit to the level of impurities that can be present in the sample.

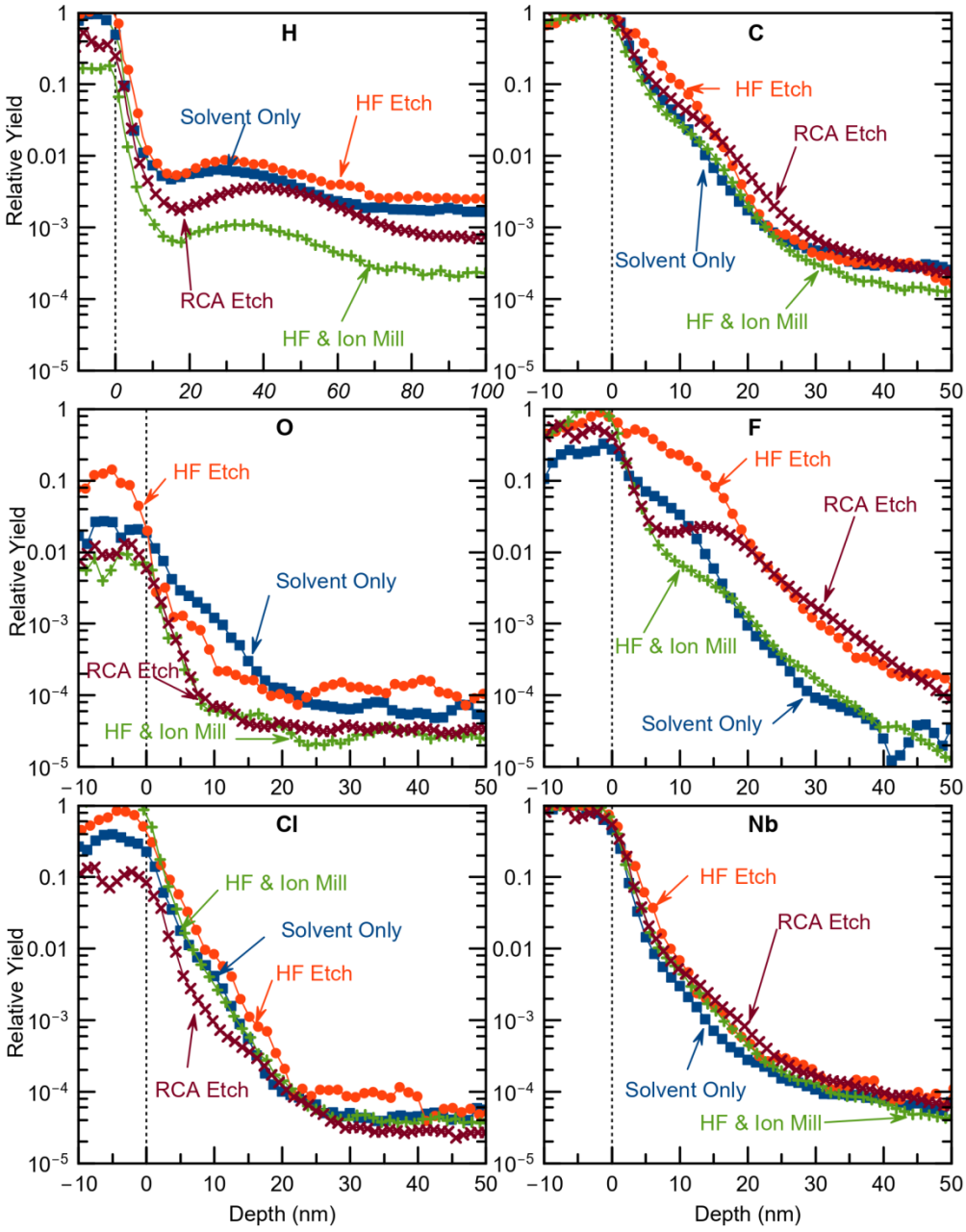

Figure 18: TOF-SIMS depth profiles comparing Nb/Si interface contaminants between Si surface preparation experiments. Each depth profile is performed using a 1 kV Cs sputter, Ga+ analysis beam, and collecting negative secondary ions. Yield is relative to the sum of Nb and Si counts to minimize matrix effects. The depth where Nb and Si yields are equal define the x-axis zero for the depth. Hydrogen is displayed to 100 nm in depth while all other elements are shown from -10 to 50 nm. The HF & Ion Mill specimen has the lowest interface impurity density in the Si.

Figure 18 shows TOF-SIMS depth profiling near the Nb/Si interfaces, beginning 10 nm from the Si surface. We detect H, C, O, F, and Cl in all specimens. In the "Solvent Only" specimen the H concentration drops off near the interface, with a 2nd peak about 25 nm from the interface and reaching a minimum ~60 nm into the Si, while the F, O, C, and Cl reach their background yields within 20–30 nm. After performing an HF Etch intended to remove surface SiO_2, we see a decrease in oxygen at the interface, as expected, but with additional C, H, and F in the silicon, indicating some contamination or residue from the HF clean process. Following an HF etch, the addition of the 60 eV in-situ ion mill ("HF & Ion Mill") decreases interfacial H and F, with Cl and F peaks concentrated on the Nb-side of the interface, resulting in the least contaminated sample in this series. In the RCA & HF & Ion Mill specimen, the width of the Nb/Si interface broadens by about 5 nm, there is increased C in the Si, and most significantly, there is a 2nd peak of F concentration about 20 nm into the Si. This 2nd peak suggests that instead of passivating a flat Si surface, the F is migrating some distance into the substrate, either due to roughness or reaction with the substrate. From these data we conclude that the interface with the lowest measured levels of contamination is produced by an HF etch followed by an in-situ ion mill at 60 eV. An RCA etch can introduce additional contamination to the Nb/Si interface that is not removed by the HF etch or ion mill.

Based on the observations that surface impurities on the Nb-side of the interface, it is likely that some mobile contaminants on the surface will preferentially accumulate in the Nb layer due to a gettering effect. Gettering on the metal side can be beneficial to devices which rely on a clean dielectric material (assuming the "dirty" metal near the interface does not cause a large drop in the superconducting order parameter), and has been used to remove defects such as iron from Si wafers[75]. This effect may be further enhanced by annealing or the introduction of other materials such as Ta and Al [76]. In

addition to gettering, the concentration of electrically active defects can be reduced by annealing Nb/Si structures, as many simple defects anneal out of silicon at temperatures between 200 and 400 °C [18].

5.4.2 **Electrical Characterization: I-V and DLTS**

Current-Voltage characteristics of a Schottky diode are sensitive to small changes in the atomic structure and contamination at the interface [77], where electronically active defects can increase the ideality factor (n) by acting as recombination centers and alter the barrier height by contributing to interface trapped charge (ϕ_B). Forward-bias current is fit to the thermionic emission equation $I = SA^*T^2e^{-\phi_B/V_t}e^{(V-IR)/nV_t}$, where S is the area of the device, A* is the Richardson constant (8.1 A/K^{2}cm^2 for Si), T is the measurement temperature, ϕ_B is the effective barrier height, V_t the thermal voltage (k_BT), R the series resistance, and n is the ideality factor. Ideality factors, n, of 1 are characteristic of thermionic emission transport while ideality factors above that correspond to prevalence of defect assisted Shockley-Reed-Hall recombination, surface leakage currents, or an interfacial oxide layer. Even in the most-ideal diodes made, the ideality factors fall slightly above one, typically 1.02-1.05, as a result of barrier-lowering effects at higher voltages from image force and tunneling [41]. As is commonly encountered, the defect levels fall between the electron and hole quasi-Fermi levels in forward bias and then the Shockley, Reed, Hall recombination results in an ideality factor of ≈2. In the case of diodes with pinholes or surface conduction, the lowest barrier will dominate until current density of the path saturates from the local spreading resistance, and the net current acts as multiple diodes in parallel, as discussed in ref [41]. Leakage from peripheral surface conduction is often linear in voltage and can be

removed by the application of a mesa etch. There is no strong evidence of such peripheral surface conduction in the devices measured here.

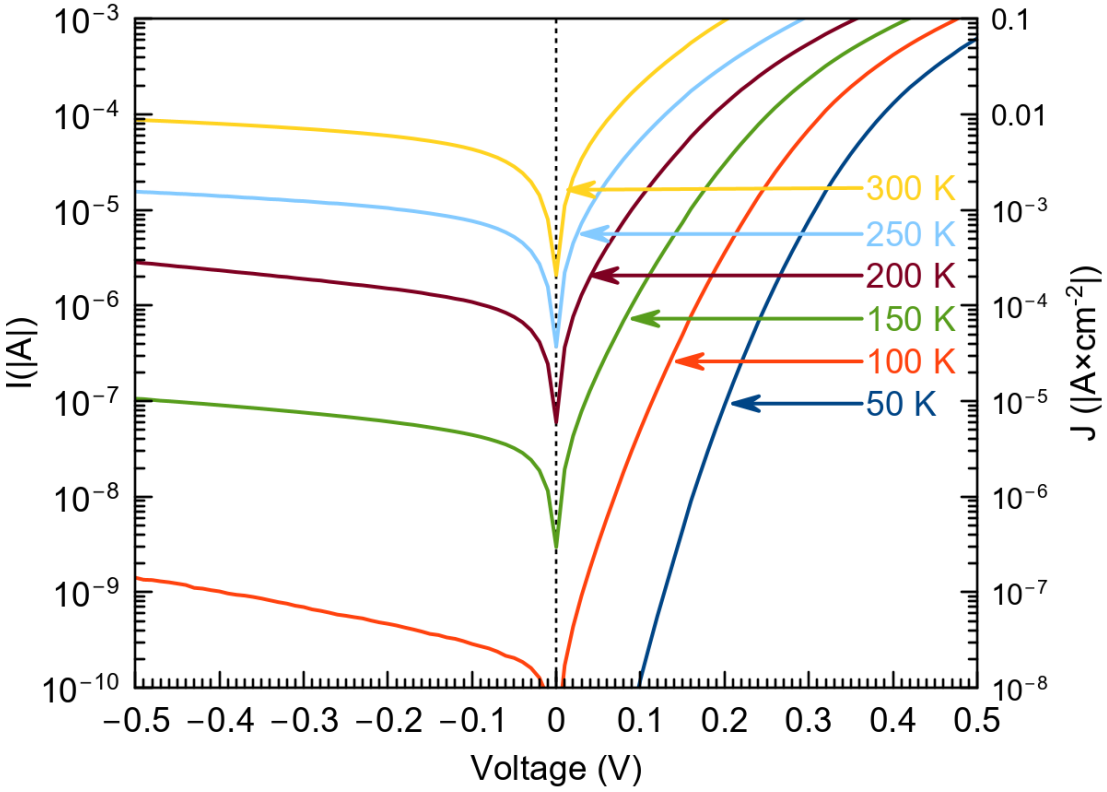

Figure 19: Representative I-V plot for an Nb/Si Schottky diode measured at different temperatures. This Si surface was cleaned with solvent only; its ideality factor at 200 K is n=2.3, indicating a dominance of Shockley-Reed-Hall recombination and/or the presence of an interfacial oxide layer.

Figure 19 shows representative I-V scans of a single Nb/Si Schottky diode at temperatures ranging from 50–300 K. At high temperatures, series resistance dominates the device properties at relatively low voltages, while at low temperatures, recombination currents dominate. For these reasons, following analyzes will focus on the I-V properties measured only at 200 K.

Figure 20 shows I-V characteristics for each of the Si-surface cleaning procedures along with the inferred ideality factor and barrier heights. The data are expressed in a semi-Log plot to visualize the slope of the graph being inversely proportional to the ideality factor. An ideality factor of n=1 corresponds to ~60 mV per decade. The "most ideal" (i.e. with lowest ideality factor of n=1.17) occurs in Nb/Si samples prepared with an HF etch and in-situ ion mill, followed by the specimen which received only an HF etch (n=1.6), while the "solvent only" and RCA etched samples exhibit n>2. Nb/Si samples that have undergone the RCA clean have a higher ideality factor than the other surface preparation methods produce.

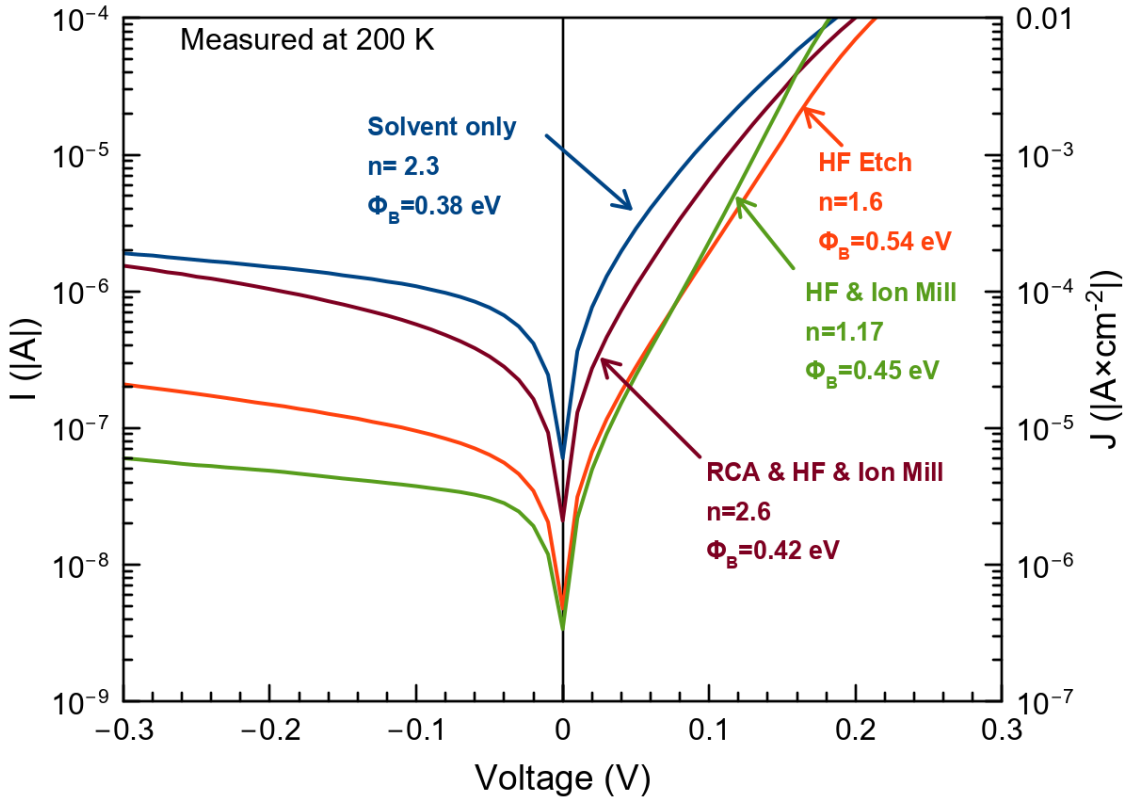

Figure 20 I-V measurements performed at 200 K comparing Nb/Si structures prepared with different Si surface treatments. Curves are labeled with the Si surface treatment performed before Nb deposition and their corresponding ideality factor and barrier height. The Ar ion mill energy used in the studies illustrated in this figure is 60 eV. The curves are: "solvent only" (n=2.3, ϕ_B=0.38 eV), "HF Etch" (n=1.6, ϕ_B=0.54 eV), "HF Etch and Ion Mill" (n= 1.17, ϕ_B=0.45 eV), and "RCA & HF & Ion Mill" (n=2.6, ϕ_B=0.42 eV)

Figure 21 shows representative DLTS temperature spectra for the specimen cleaned with an HF etch and 60 eV ion mill, and the associated Arrhenius plot is in Figure 22. All specimens display similar DLTS spectra, dominated by a negative peak near T_{peak} = 250K, followed by four additional defects at lower temperature and much lower intensity. All resolved defect peaks are negative, corresponding to majority carrier hole traps.

Table 4 summarizes the fitted activation energies and capture cross sections observed in every specimen with their possible identifications, while Table 5 compares the defect concentrations of these defects between surface treatments. Defect activation energies will be referred to by the common shorthand notation H (for hole) followed by parentheses with the energy above E_{vbm} in eV. The dominant defect H(0.556) (at T_{peak}=250 K)–which refers to a hole trap at E_{vbm}+0.556 eV—is most likely associated with a niobium defect in p-type silicon, as reported in [24]. Interestingly, this defect changes activation energy and capture cross section before and after the addition of an HF etch. This may correspond to the presence of a nearby "spectator" defect or other forms or a change in environment. In the "solvent only" sample, the energy of this peak is E_V+0.447 eV and its capture cross section $\sigma=2.62\times10^{-15}$ cm², while all subsequent surface treatments this defect occurs at E_V+0.556 eV with $\sigma=3.72\times10^{-13}$ cm², but both activation energies correspond to reported energy levels for niobium in p-type silicon [24] [23]. The large ~10^{-13} cm² capture cross section observed for H(0.556) suggests its origin may be associated with a defect complex involving niobium, but present literature reports do not speculate on the exact nature of this defect. The H(0.194) defect matches energy levels for a silicon divacancy with a +1 charge, $(V_{Si}\text{-}V_{Si})^+$ [18], and also matches reported energy levels associated with F and Cl in Si [23]. The H(0.339) defect matches the energy for a thermally-activated V_{Si}^{2+} migration, and a V_{Si}^0 migration [18], and is close to both the

energy and capture cross section reported for a C_s-C_i pair [78]. However, vacancies in silicon are highly mobile, and expected to anneal out at temperatures above 200 K [18], so these are unlikely to survive except if trapped by another defect. While the listed origins represent some possibilities, confidently determining the physical origin of energy levels is requires further investigations.

The ideality factor inferred from the I-V characteristics (Figure 20) correlates reasonably well with the total defect concentration measured by DLTS, as shown in Table 5. This is consistent with expectations from the Shockley-Read-Hall recombination theory [79][80]. However, there does not appear to be prior work that has documented this important relationship. In terms of both chemical and electrical properties, the HF etch and 60 eV ion milled Si surface yields diodes with the lowest contamination levels and best electrical properties found among the different cleaning methods.

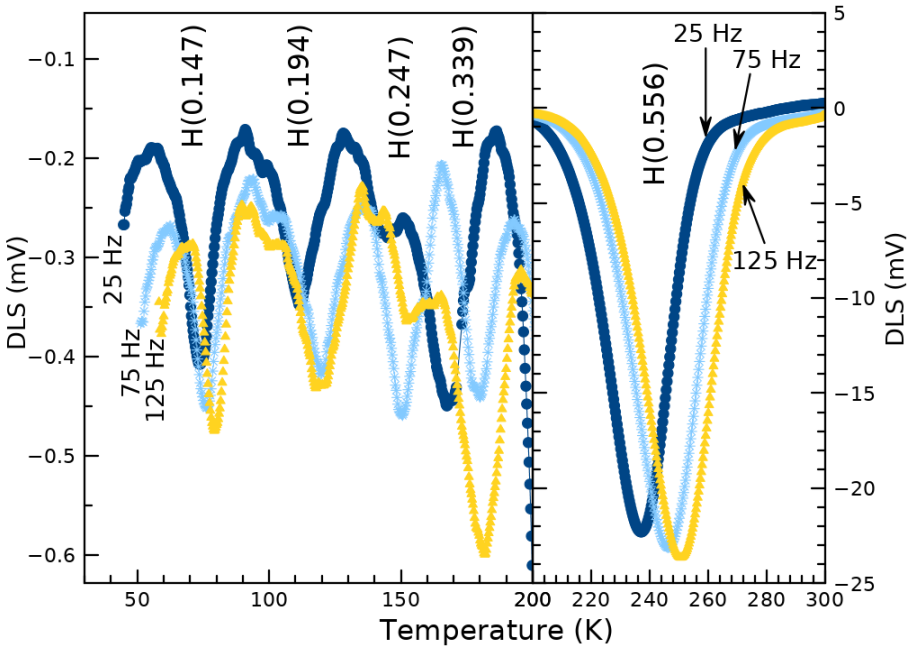

Figure 21: Representative DLTS spectra for Nb/Si diode prepared with HF etch and 60 eV ion mill performed at 25, 75, and 125 Hz. The spectra are dominated by the peak identified as H(0.556) (right), attributed to a Nb defect [24][23].

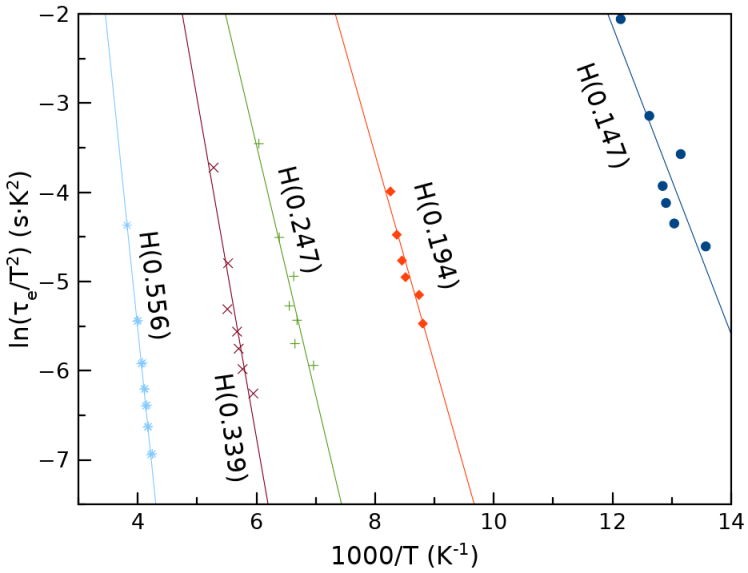

Figure 22: Representative Arrhenius plot of the DLTS peaks for the diode prepared with a HF and 60 eV ion milled surface clean measured with rate windows 25, 35, 45, 55, 75, 125, and 400 Hz. Each point corresponds to the temperature and emission rate of a peak measured in DLTS-temperature spectra at different frequencies. Linear least-mean-square error fits are drawn through points corresponding to the same peak measured at different frequencies. The slope of each line corresponds to the energy level of the trap, and the capture cross-section is inferred from the y-intercept.

Designation	Energy Level (meV)	σ (cm²)	T^{a}_{peak} (K)	Possible origins
H(0.147)	E_v+147 (±2)	6.7×10^{-14} ($\pm0.3\times10^{-14}$)	75	
H(0.194)	E_v+194 (±7)	6.2×10^{-15} ($\pm5.8\times10^{-14}$)	120	$(V_{Si}\text{-}V_{Si})^{+}$ [18], F [23], Cl [23]
H(0.247)	E_v+247 (±5)	1.4×10^{-15} ($\pm1.5\times10^{-15}$)	150	
H(0.339)	E_v+339 (±15)	2.1×10^{-14} ($\pm1.3\times10^{-14}$)	180	C_s-C_i pair [78], V_{Si}^{2+}, or V_{Si}^{o} migration[18]
H(0.556)[b]	E_v+556 (±12)	3.72×10^{-13} ($\pm1.5\times10^{-13}$)	250	Nb [24] or inter-Nb[23]

Table 4: Average defect energy levels, their capture cross sections, temperatures, and potential defect identifications. All defects measured are majority carriers (hole traps). The assignment of possible origins come from using both the information on the potential species in the area obtained from the SIMS measurements and from comparing energy level and capture cross section to the literature. Reported capture cross sections are calculated from Arrhenius plots, and may have large error.
[a] Nominal peak temperature with rate window set to 75 Hz.
[b] The values for the defect at T_{peak}=250 K in the minimally-processed "solvent only" sample deviate from the others and are not included in these averages. Its values are $E=E_V+447$ meV, and $\sigma=2.62\times10^{-15}$ cm².

	H(.147) (cm^{-3})	H(0.194) (cm^{-3})	H(0.247) (cm^{-3})	H(0.339) (cm^{-3})	H(0.556) (cm^{-3})
Possible Origins		$(V_{Si}\text{-}V_{Si})^{+}$ [18], F [23], Cl [23]		C_s-C_i pair [78], V_{Si}^{2+} migration[18]	Nb [24] or inter-Nb [23]
Solvent only	*>7.4×10^{12}	*>6.4×10^{12}	*>6.3×10^{12}	7.2×10^{12}	2.50×10^{14}
HF Etch	*>6.5×10^{12}	*>1.3×10^{12}	*>2.4×10^{12}	6.6×10^{12}	1.73×10^{14}
RCA & HF & Ion Mill	1.1×10^{13}	6.7×10^{12}	6.4×10^{12}	6.6×10^{12}	4.86×10^{14}
HF & Ion Mill (60 eV)	1.9×10^{12}	3.1×10^{12}	1.3×10^{12}	2.8×10^{12}	1.66×10^{14}
HF & Ion Mill (100 eV)	*>1.92×10^{12}	*>2.72×10^{12}	8.1×10^{12}	1.1×10^{13}	7.4×10^{13}
HF & Ion Mill (150 eV)	1.4×10^{13}	3.0×10^{13}	1.8×10^{13}	3.1×10^{13}	1.96×10^{14}

Table 5: Comparison of defect concentrations for each specimen. All values are minimum values. The symbol *> refers to lower-bound values. In these cases, the peaks are not well defined as a result of the small signal being on the order of the measurement noise.

5.4.3 **Optimization of Ion Mill Energy**

This section compares the interfaces of Nb on p-type Si where the Si was cleaned with an HF etch followed by an Ar ion mill at 60, 100, or 150 eV, with the same total ion dose. Higher energy incident ions are expected to remove more interface contamination, but with a higher probability of introducing Si vacancy, interstitials and other native defects.

Figure 23 shows TOF-SIMS depth profiles for Si cleaned with an HF etch followed by in-situ ion milling at 60, 100, and 150 eV. Interestingly, there does not appear to be any change in Nb/Si intermixing as a result of higher ion mill energy (within the approximately 5 nm resolution for these sputter depth profiles). The nature and level of chemical contamination observed in the Si layer is nearly identical between all three samples.

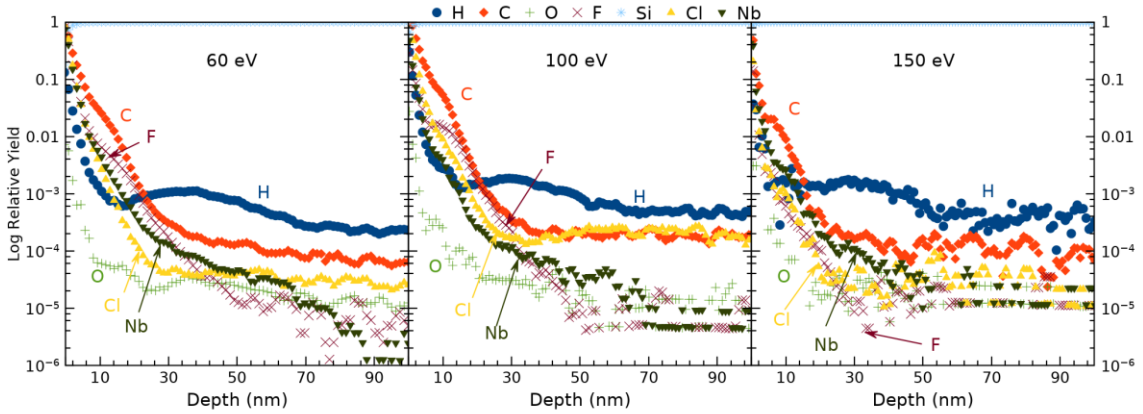

Figure 23: TOF-SIMS depth profiles showing contaminants measured near the Nb/Si interface for Si substrates cleaned with HF etch followed by a 2-minute in-situ ion mill at **(a)** 60 eV, **(b)** 100 eV, and **(c)** 150 eV. The zero of the x-axis scale is set at the depth where the Nb and Si yields are equal.

I-V measurements performed at 200 K are shown in Figure 24. Increasing the ion mill energy from 60 eV to 100 eV reduces the current in reverse bias by almost 2 orders

of magnitude, and decreases the ideality factor from n=1.17 to n=1.07. Increasing the ion mill energy to 150 eV results in nearly the same curve as the 100 eV-cleaned specimens, with slightly improved ideality factor n=1.06. These results indicate that ion milling with energy greater than 100 eV can improve the Schottky barrier properties of the Nb/Si interface.

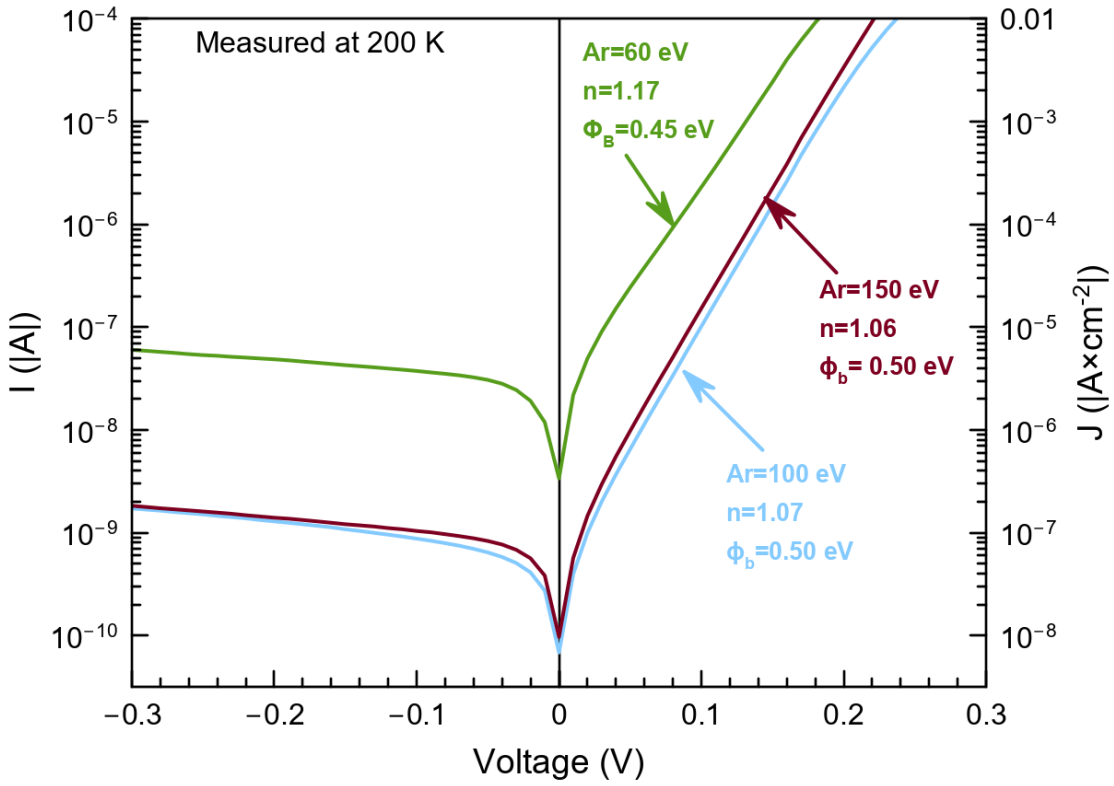

Figure 24: I-V measurements performed at 200 K comparing Nb/Si structures prepared with an HF etch followed by an in-situ Ar ion mill, with varying mill energies. Curves are labeled with the energy of incident Ar ions and their corresponding ideality factor and barrier height. They are: "Ar=60 eV" (n=1.17, ϕ_B=0.45 eV), "Ar=100 eV" (n=1.07, ϕ_B=0.50 eV), and "Ar=150 eV" (n=1.06, ϕ_B=0.50 eV).

Table 5 includes the defect concentrations for each activation energy determined by DLTS for the HF and ion milled Schottky diodes. The concentration of the dominant defect, H(0.556), is lowest in the specimen ion milled with 100 eV Ar ions, approximately half the concentration observed in the 60 eV and 150 eV ion milled specimens. The increase in concentration of the H(0.339) and H(0.247) with higher energy ion milling indicates that these are ion-induced defects. The 100 eV ion milled specimen has the lowest total deep level defect concentration of any measurements, with $N<10^{14}$ cm^{-3}. These data confirm that surface cleaning procedures must be optimized to minimize the total defect concentration near the interface without introducing additional defects from substrate cleaning processes.

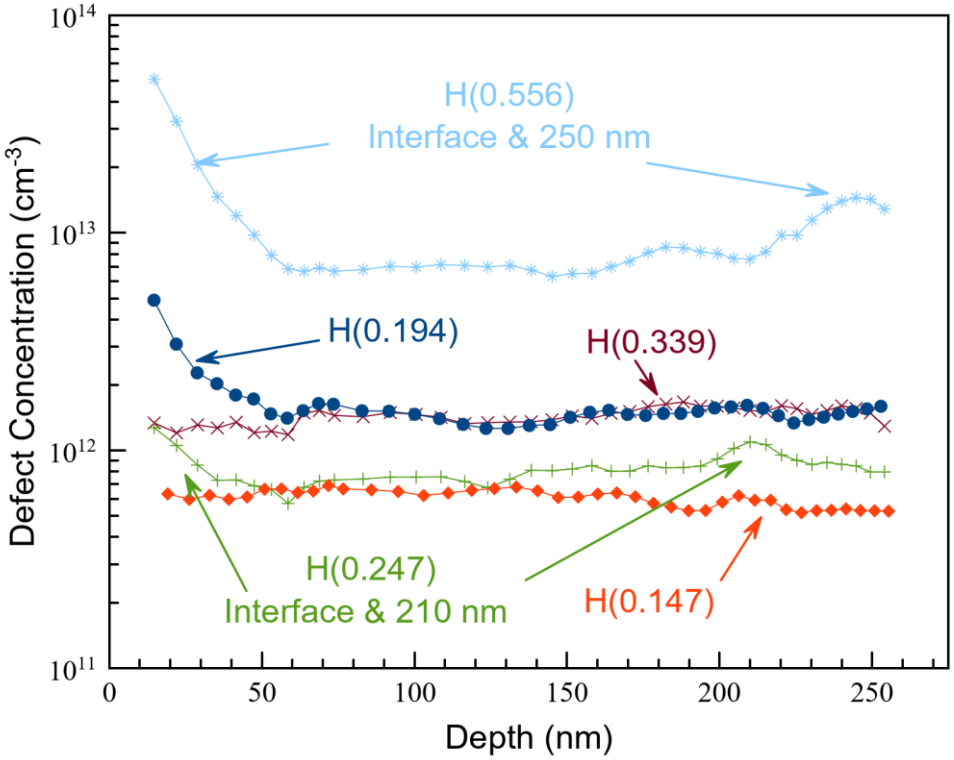

Figure 25: Representative defect depth profiles for HF etched and 150 eV ion milled specimen. Defects are primarily concentrated at the interface, within the first 50 nm, while the DLTS measurements of defects H(0.556) and H(0.247) have a second peak between 200 and 250 nm.

DLTS was used to perform depth profiles of electrically active defects, shown in Figure 25. DLTS depth profiling techniques can probe within ~10 nm of the interface. These measurements find that the majority of defects are concentrated within the first 50 nm from the interface, matching the range of interface contamination observed with TOF-SIMS. The defects H(0.147) and H(0.339) have nearly constant concentration across the measurement range. Two defects, H(0.247) and H(0.556) exhibit a second peak in concentration at approximately 210 and 240 nm deep, respectively. This deep accumulation near the edge of the depletion region suggests that these are mobile defects and have some charge that drives them into the substrate.

5.5 Annealing of Nb/Si structures

Annealing will affect superconductor/dielectric intermixing, distribution of contaminants, and point defect concentration in the dielectric. Annealing has the potential to reduce TLS loss through a number of mechanisms; gettering mobile contaminants from the dielectric into the Nb [81], to recombine vacancy/interstitial pairs, and to form a strongly reacted compound at the interface (like a silicide). In some strongly reacting layered structures, this kind of self-limiting reaction may be desirable to prevent further intermixing. However, at lower temperatures Nb/Si interdiffusion is more likely to occur than a silicide reaction.

Preliminary annealing studies were performed on Nb/Si Schottky diode structures cleaned with the "HF etch" process described above (5 minutes in HF 2 vol% aqueous). Film structures were annealed in forming gas (95 % Ar, 5% H_2) at each 150, 250, 350, or 450° C for 15 minutes. TOF-SIMS depth profiles measured across the interface (Ga primary ions, negative ions recorded, with Cs sputter at 3 kV) did not find any difference in interface intermixing as a result of annealing up to 450 °C.

Interestingly, the concentration and distribution of interface contaminants changes significantly after annealing. Oxygen at the Nb/Si interface (Figure 26, bottom right) is originally concentrated on the "silicon-side" of the Nb/Si interface. Following a 450 °C anneal in forming gas, the oxygen on the Si side decreases, and appears to have migrated onto the niobium side, resulting in higher concentrations of oxygen in the niobium layer. The mechanism typically responsible for SiO_2 decomposition ($Si+SiO_2 \rightarrow 2SiO$) typically requires high temperatures >1200° C [82]. The movement of

this oxygen after a 450 °C anneal suggests either that the O at the Si surface is not in the SiO_2 form, or that sputtered Nb lowers the energy barrier for O movement. Furthermore, this indicates that the Niobium is a strong getter for oxygen.

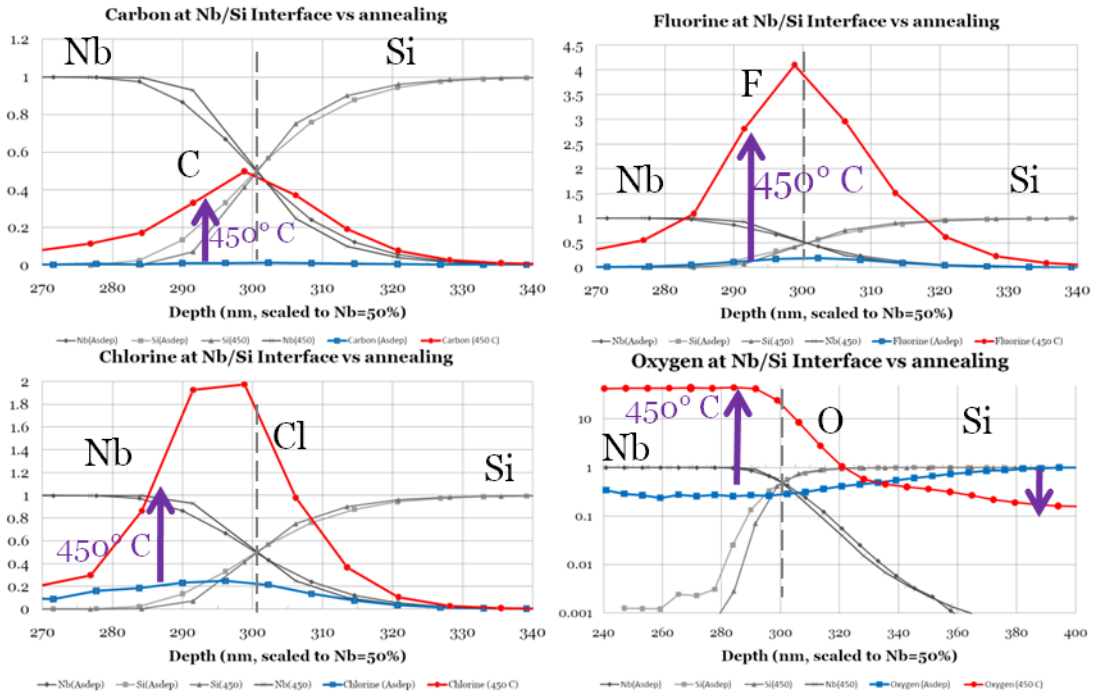

Figure 26: Selected element depth profiles comparing as-deposited and specimens annealed in forming gas at 450° C. Grey background lines correspond do Nb and Si before and after annealing. Intensity is normalized to the sum of niobium and silicon intensity at that depth. (a-top left) shows carbon, (b-top right) shows fluorine distribution, (c- bottom left) shows chlorine, and (d-bottom right, semi-log scale) shows oxygen distribution. X-axis is depth in nm from the top Nb surface, and Y-axis is normalized intensity.

The measured concentrations of C, F, and Cl (Figure 26) also show a significant increase at the Nb/Si interface in annealed specimens, even when initial compositions were very low. These increases may be attributed to gettering and trapping at defects near the interface. Otherwise, the larger incorporation of oxygen in that region may significantly decrease the ionization energy of other species in that region, resulting in an anomalously high measurement of these elements.

Electrical characterization of these annealed Nb/Si Schottky barriers finds that annealing can improve the electrical device properties of a device, in this case Si prepared with an HF Etch but without an ion mill. I-V results (Figure 27) find a decrease in reverse bias current, an improvement in ideality factor, and a decreased barrier height upon annealing. DLTS measurements find that the defect concentration decreases after annealing at 100, 150, and 200 °C, with no measurable defects after an anneal of 250 °C. This is presumably a result of trapping mobile defects, "annihilating" Frenkel pairs, "gettering" impurities to the Nb layer.

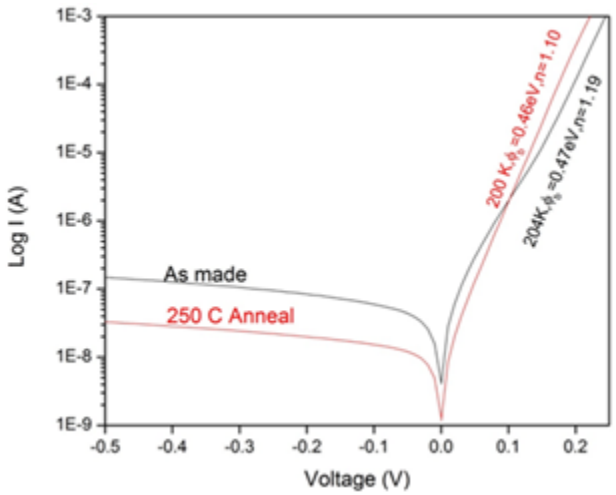

Figure 27: I-V plots of the same Nb/Si Schottky barrier, "as made" and after a 250 °C anneal in forming gas. Before annealing, the ideality factor is n=1.19 with ϕ_B=0.47 eV, after annealing n=1.10 and ϕ_B=0.46 eV. Figure by collaborator Madhu Krishna Murthy, used with permission.

5.6 Conclusions

The sensitive techniques TOF-SIMS, I-V, and DLTS have been used to compare the chemical and electrical properties of defects at the Nb-Si interface. These have identified chemical contamination at the interface from H, C, O, F, and Cl, within the top 50 nm of the Si substrate, and deep level defects at E_{vbm}+0.147, E_{vbm}+0.194, E_{vbm}+0.247, E_{vbm}+0.339, and E_{vbm}+0.556 eV. Based on DLTS depth profiling, most electronic defects are within the 50 nm closest to the Nb/Si interface, with the defects at E_{vbm}+0.556 eV and E_{vbm}+0.247 exhibiting a second, albeit much lower concentration, peak of charged defects 200-250 nm deep. Comparing different surface preparation techniques finds a minimum total defect concentration when the Si surface is cleaned with an HF etch and a 100 eV in-situ Ar ion mill. More aggressive chemical surface treatments (RCA clean) and higher energy ion milling (Ar at 150 eV) result in significantly more defects at the interface.

CHAPTER 6

HIGH-TEMPERATURE SUPERCONDUCTING STRUCTURES

6.1 Abstract

This investigation documents the deposition of thin-film trilayer structures comprised of high-critical temperature $YBa_2Cu_3O_{7-\delta}$ superconductor electrodes and high-performance perovskite $Ba(Zn_{1/3}Ta_{2/3})O_3$ and $Ba(Cd_{1/3}Ta_{2/3})O_3$ microwave dielectric thin-films that have excellent structural and electrical properties. A thin $SrTiO_3$ buffer layer between the superconductor and microwave dielectric thin-films improves the structural quality of the $YBa_2Cu_3O_{7-\delta}$, resulting in transition temperatures, T_C, of 90 K. These advances enable the production of more compact high-temperature superconductor capacitors, inductors, and microwave microstrip and stripline devices.

6.2 Introduction

$YBa_2Cu_3O_{7-\delta}$ in thin-film form has been often chosen to fabricate superconductor devices because of its high superconducting transition temperature of 92 K, high critical current, J_c of ~10^7 A/cm^2 [83], large upper critical field, Hc_2 of over 100 T [84]) and small microwave surface resistance, R_S of~1-2x10^{-5} Ω/□ [85][86]. However, the electrical properties of $YBa_2Cu_3O_{7-\delta}$ films degrade when the material is not epitaxial or at least highly textured. For example, the critical current decreases significantly, and the microwave surface resistance increases when the films contain large-angle grain boundaries [87][86]. These factors make it difficult, but not impossible, to produce useful, high-quality $YBa_2Cu_3O_{7-\delta}$ films on substrates that are chemically reactive and poorly lattice-matched. Soon after the discovery of high-T_C superconductors, several

groups used buffer layers to make high-quality films on dielectric substrates, including MgO on M-plane $(10\bar{1}0)$ sapphire, CeO buffer layers on R-plane $(1\bar{1}02)$sapphire [88], SrTiO3 on $(1\bar{1}02)$ sapphire [89], and yttria-stabilized zirconia, YSZ, on silicon on sapphire substrates [90].

Due to $Ba(Zn_{1/3}Ta_{2/3})O_3$'s high dielectric constant, κ of 29, small loss tangent of $1.6x10^{-5}$ at 2 GHz, and zero or near-zero thermal expansion coefficient when selectively doped with Ni, this compound has been widely used to make high-performance microwave filters and resonators. [91][92]. There is also interest in other similar Ba-based perovskite tantalates, including $Ba(Mg_{1/3}Ta_{2/3})O_3$, and $Ba(Cd_{1/3}Ta_{2/3})O_3$, The integration of these materials into thin-film structures could enable performance improvements in capacitor, inductor, and thin-film microwave technologies [93].
Achieving proper stoichiometry and high-structural quality are needed to attain useful $YBa_2Cu_3O_{7-\delta}$ [94] and dielectric film electrical properties. Earlier research describes methods to deposit epitaxial and stoichiometric $Ba(Cd_{1/3}Ta_{2/3})O_3$ [95] and $Ba(Zn_{1/3}Ta_{2/3})O_3$ thin-films on MgO substrates using Pulsed Laser Deposition (PLD) [96]. High oxygen overpressures increase the formation of the less volatile ZnO and CdO oxides on the surface and were needed to minimize the loss of these elements from the surface during the thin-film growth process.

This investigation aims to combine high-quality superconducting $YBa_2Cu_3O_{7-\delta}$ films and deposited thin film high-κ dielectrics to enable improvements in the performance of future integrated microelectronic devices. This study will show that the use of a buffer layer between the dielectric layer and high T_C superconductor $YBa_2Cu_3O_{7-\delta}$ with lattice constants of a=3.82 Å and b=3.89 Å is necessary to obtain device-quality films. This is needed because this perovskite superconductor has a significantly smaller

in-plane lattice parameter than $Ba(Cd_{1/3}Ta_{2/3})O_3$ with a=4.17 Å and $Ba(Zn_{1/3}Ta_{2/3})O_3$ a=4.09 Å.

6.3 Experimental Procedures

A number of substrates were used, including (100) LaAlO3, (100) MgO, *a*–SiO_2/Si, (100) Si, R-plane $(1\bar{1}02)$ Al2O3, and (100) SrTiO3. Substrates are affixed to a resistive heater [97] with silver paste to ensure intimate thermal contact and then the heater is inserted into a cryo-pumped deposition chamber. This system is then evacuated to a base pressure lower than 5×10^{-8} Torr before backfilling with 200 mTorr oxygen with 99.9999% purity. Films are deposited using Pulsed Laser Deposition (PLD) with an excimer laser (Lambda Physik, Compex 201, λ = 248 nm) operated at 5 Hz with a target-substrate distance of ~7 cm. Targets are 2.5 cm diameter commercially-produced $YBa_2Cu_3O_{7-\delta}$, and in-house manufactured Zn-rich $Ba(Zn_{1/3}Ta_{2/3})O_3$:0.75 ZnO and Cd-rich $Ba(Cd_{1/3}Ta_{2/3})$:0.75 CdO, whose fabrication methods are described below. $YBa_2Cu_3O_{7-\delta}$ layers are deposited at 770 °C, and dielectric layers, $Ba(Zn_{1/3}Ta_{2/3})O_3$ and $Ba(Cd_{1/3}Ta_{2/3})O_3$), and buffer layers, $SrTiO_3$ and MgO, are deposited at 524 °C, the temperature optimized to produce stoichiometric films with these target compositions, as determined in earlier studies [95][96].

The Zn-rich $Ba(Zn_{1/3}Ta_{2/3})O_3$ and Cd-rich $Ba(Cd_{1/3}Ta_{2/3})O_3$ targets are prepared by conventional powder processing methods using reagent grade $BaCO_3$, ZnO, CdO, and Ta_2O_5 powders. The oxide powders were mixed homogenously by ball-milling in an ethanol slurry as per required stoichiometry. The dried slurries were calcined at 1200°C for 8 hours, and then the calcined powder was ball-milled in ethanol slurry along with paraffin wax–stearic acid mix binder. The resulting dried powder from slurry was screened using a 48-mesh sieve. The powder is pressed at 20 KPa/in, yielding a ~60%

theoretical density green body. Then, the target is sintered at 1600 °C for 10 hours while covered in excess powder to compensate the evaporation of volatile elements. The composition of the final target's composition is $Ba(Zn_{1/3}Ta_{2/3})O_3$:0.75 ZnO and $Ba(Cd_{1/3}Ta_{2/3})O_3$:0.75 ZnO, as determined by Particle Induced X-ray emission ,PIXE.

Temperature-dependent electrical measurements are performed by contacting specimens with four-point pogo-pins and dipping into a liquid helium storage dewar. For superconducting transition temperature measurements, the T_{C90} and the ΔT_C are used to indicate the temperatures where the resistivity is 90% of the value before the transition, and the temperature difference between 10% and 90% drop in resistivity, respectively.
To determine crystal structure and orientations, X-ray Diffraction, XRD, is performed using a PANalytical X'pert MRD Pro diffractometer with a 3-bounce Ge X-ray mirror on the incident optics and parallel plate collimator, PPC, on the detector side.

6.4 Results and Discussion

To determine if the high-temperature superconductor could be produced directly on the materials of interest, 200 nm thick $YBa_2Cu_3O_{7-\delta}$ layers were deposited on 200 nm of $Ba(Cd_{1/3}Ta_{2/3})O_3$ on MgO (0.96% mismatch) and lattice-mismatched substrates, Si (100), R-plane (1-102) Al_2O_3, *a*-SiO_2, $SrTiO_3$, $LaAlO_3$. Resistivity vs. temperature measurements (Figure 28-a) find the highest T_C with T_{C90}=86.6 K and T_{C10}=60.7 K and lowest resistivity of $\rho=1.6\times10^{-3}$ Ω-cm for $YBa_2Cu_3O_{7-\delta}$ deposited on $Ba(Cd_{1/3}Ta_{2/3})O_3$ on MgO, which is the closest lattice matched system. Surprisingly, the onset of the superconducting transition is not significantly affected by substrate choice, only the normal resistivity and the width of the transition are adversely affected. X-ray diffraction results for these structures, shown in Figure 28-b, have small diffraction intensity Bragg

peaks and a significant shift in the peak from the bulk value for the $YBa_2Cu_3O_{7-\delta}$ (050) orientation, indicating a low crystalline quality $YBa_2Cu_3O_{7-\delta}$ layer. While earlier studies determined the MgO substrate produces the best $Ba(Cd_{1/3}Ta_{2/3})O_3$ films—which is also observed—note that the intensity of the $YBa_2Cu_3O_{7-\delta}$ (050) Bragg peaks is small and the superconducting electrical transition is wide. The poor quality of the $YBa_2Cu_3O_{7-\delta}$, when deposited directly on these layers, inspired the insertion of a buffer layer between the dielectric and superconductor deposition.

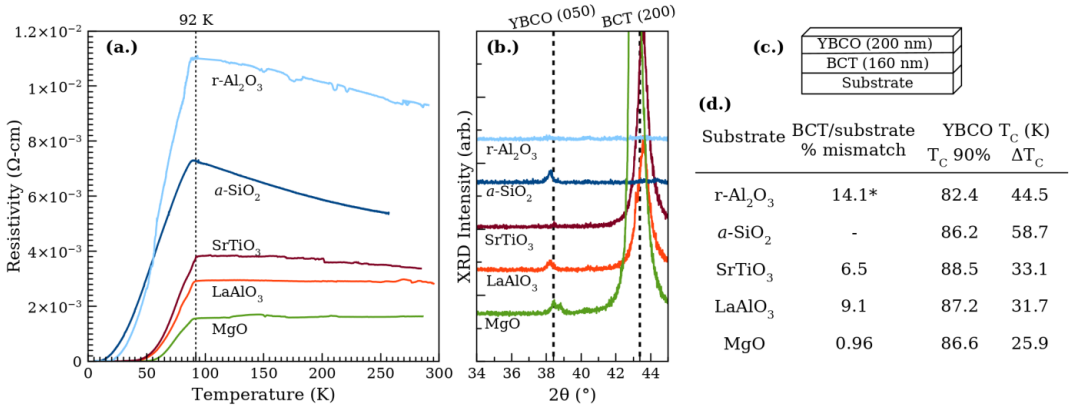

(d.)

Substrate	BCT/substrate % mismatch	YBCO T_C (K) T_C 90%	ΔT_C
$r\text{-}Al_2O_3$	14.1*	82.4	44.5
$a\text{-}SiO_2$	-	86.2	58.7
$SrTiO_3$	6.5	88.5	33.1
$LaAlO_3$	9.1	87.2	31.7
MgO	0.96	86.6	25.9

Figure 28: The schematic diagram of the specimen configuration is shown in (c) for the substrates listed in (d). In (a), Resistivity vs. temperature for the top $YBa_2Cu_3O_{7-\delta}$ layers of $YBa_2Cu_3O_{7-\delta}$ (200 nm)/$Ba(Cd_{1/3}Ta_{2/3})O_3$ (160 nm)/substrate structures, with r-plane Al_2O_3, amorphous *a*-SiO_2, $SrTiO_3$, $LaAlO_3$, or MgO substrates. The dotted line represents the bulk $YBa_2Cu_3O_{7-\delta}$ T_C. In (b), the θ-2θ configuration XRD shown in (b) identifies the $YBa_2Cu_3O_{7-\delta}$ (050) and $Ba(Cd_{1/3}Ta_{2/3})O_3$ (200) diffraction orientations.
*The($\mathbf{1\bar{1}02}$) R-plane of Al2O3 is rectangular, with spacing $d_{[1\bar{2}10]}$=4.76 Å and $\mathbf{d}_{[10\bar{1}1]}$=5.12 Å, so the mismatch is estimated using the lower mismatch $d_{[1\bar{2}10]}$.

300 nm of $Ba(Cd_{1/3}Ta_{2/3})O_3$ were deposited onto MgO substrates, followed by thin 10 nm buffer layers of MgO or $SrTiO_3$, then an upper layer of 300 nm $YBa_2Cu_3O_{7-\delta}$. Resistivity-vs-temperature measurements performed on the top $YBa_2Cu_3O_{7-\delta}$ layer for $YBa_2Cu_3O_{7-\delta}$/buffer/ $Ba(Cd_{1/3}Ta_{2/3})O_3$ structures in Figure 29 show that the $SrTiO_3$ buffer layer produces films with the highest T_Cs, smallest transition widths, and lowest resistivities. Additionally, the extrapolation of the resistivity y-intercept is near zero- a qualitative indicative of high-quality $YBa_2Cu_3O_{7-\delta}$ with low grain-boundary resistance

[98]. These results indicate that a $SrTiO_3$ buffer layer can be used to produce high-quality $YBa_2Cu_3O_{7-\delta}$ films on $Ba(Cd_{1/3}Ta_{2/3})O_3$ dielectric layers.

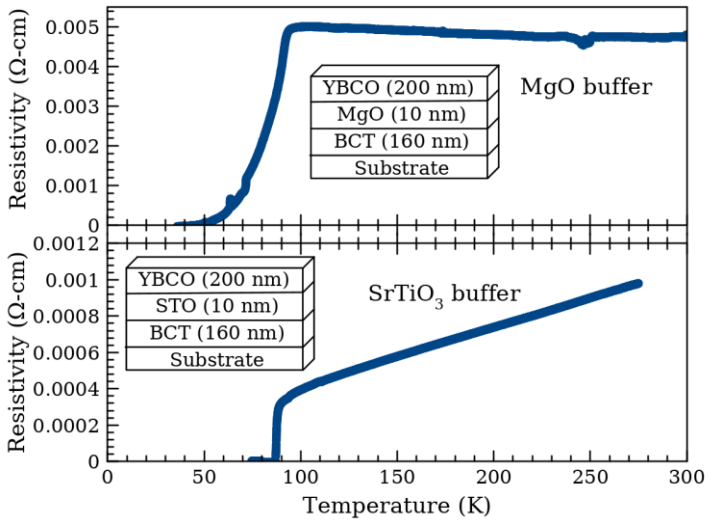

Figure 29: Resistivity-vs-temperature plots for $YBa_2Cu_3O_{7-\delta}$ /buffer/ $Ba(Cd_{1/3}Ta_{2/3})O_3$ structures on MgO substrates. The sample with the $SrTiO_3$ buffer layer shows a higher T_C, lower resistivity, and the extrapolation of the resistivity intercepts to zero-temperature. For the $YBa_2Cu_3O_{7-\delta}$ film on MgO buffer, the T_{C90} and T_{C10} are 91.6 and 64.6 K, respectively. For the $YBa_2Cu_3O_{7-\delta}$ film on $SrTiO_3$ buffer, the T_{C90} and T_{C10} are T_C(90/10) are 88.0 and 87.1 K, respectively.

Figure 30 shows the resistivity versus temperature characteristics of YBCO(100)/STO(10)/BZT(200)/STO(10)/YBCO(100) and YBCO(100)/$SrTiO_3$(1)/BCT(200)/STO(10)/YBCO(100) on $LaAlO_3$ substrates. The numbers in parenthesis are thicknesses in nm and the abbreviations YBCO, STO, BZT, and BCT refer to $YBa_2Cu_3O_{7-\delta}$, $SrTiO_3$, $Ba(Zn_{1/3}Ta_{2/3})O_3$, and $Ba(Cd_{1/3}Ta_{2/3})O_3$ respectively. By probing the dielectric when deposited on the $YBa_2Cu_3O_{7-\delta}$ structures fabricated under the same conditions and finding immeasurably high resistivity, it can be assumed that the bottom layer of $YBa_2Cu_3O_{7-\delta}$ will minimally affect these top resistivity measurements. The top $YBa_2Cu_3O_{7-\delta}$ film on a buffered $Ba(Cd_{1/3}Ta_{2/3})O_3$ dielectric layer exhibits T_{C90}=91.5 K and T_{C10}=89.0 K. The $YBa_2Cu_3O_{7-\delta}$ film on a buffered

$Ba(Zn_{1/3}Ta_{2/3})O_3$ dielectric exhibits a T_{C90}=89.5 K and T_{C10}=87.5 K. The introduction of $SrTiO_3$ buffer layers has successfully resulted in high-quality structures, which will enable the production of higher-performing capacitor, inductor and microwave thin-film device structures.

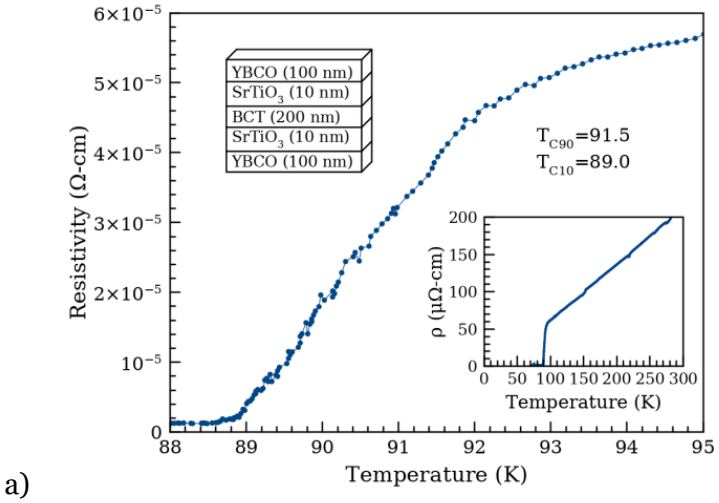

a)

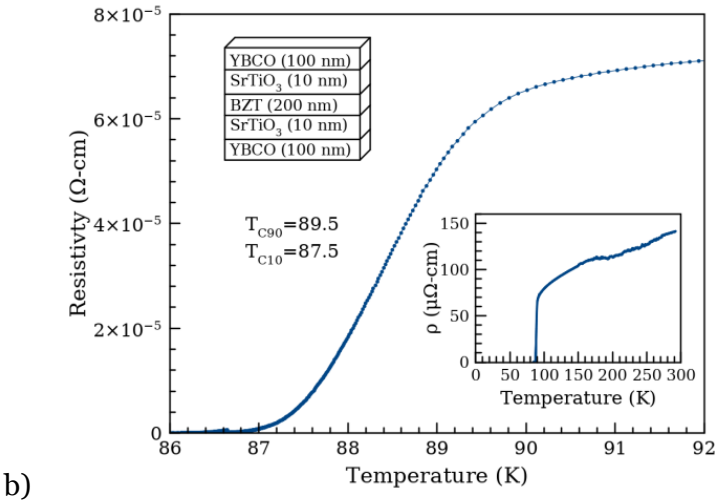

b)

Figure 30: Resistivity versus temperature results on the upper layer of superconductor/dielectric/superconductor structures deposited on $LaAlO_3$ substrates, with the main figures displaying the values near the transition and the insets showing a wider range of temperatures. (a) $YBa_2Cu_3O_{7-\delta}$ /STO/ $Ba(Cd_{1/3}Ta_{2/3})O_3$ /STO/ $YBa_2Cu_3O_{7-\delta}$ structure has a T_{C90} of 91.5 K, and T_{C10} of 89.0 K (b) $YBa_2Cu_3O_{7-\delta}$ /STO/ $Ba(Zn_{1/3}Ta_{2/3})O_3$ /STO/ $YBa_2Cu_3O_{7-\delta}$ structure has a T_{C90} of 89.5 K and T_{C10} of 87.5 K

In-plane and out-of-plane X-ray diffraction illustrated in Figure 31 and Figure 32 are used to determine the structural orientations of layers in the $Ba(Zn_{1/3}Ta_{2/3})O_3$ and $Ba(Cd_{1/3}Ta_{2/3})O_3$ trilayers. The $Ba(Cd_{1/3}Ta_{2/3})O_3$ layer is textured polycrystalline with grains primarily oriented with the {100} family of planes perpendicular to the surface. A $Ba(Cd_{1/3}Ta_{2/3})O_3$ (200) peak is observed with intensity ~22 times higher than the small $Ba(Cd_{1/3}Ta_{2/3})O_3$ (220) peak. Because the (220) and (200) intensities have virtually identical X-ray diffraction structure factors [99], this implies a strong $Ba(Cd_{1/3}Ta_{2/3})O_3$ (200) texture. The $Ba(Zn_{1/3}Ta_{2/3})O_3$ layer is textured polycrystalline primarily in the (202) orientation, with intensity 13 times larger than the (024) peak, relative to the expected intensities for a randomly-oriented powder [100]. Because there are two $YBa_2Cu_3O_{7-\delta}$ layers, and the X-ray probe depth includes the full structure, it is not possible to independently determine the crystal quality of the upper and lower $YBa_2Cu_3O_{7-\delta}$ layers. However, it can be seen that the out-of-plane diffraction scans only yields $YBa_2Cu_3O_{7-\delta}$ peaks from the {010} family of planes, with no other visible $YBa_2Cu_3O_{7-\delta}$ diffraction peaks. Furthermore, in-plane ϕ-scans using the (113) $YBa_2Cu_3O_{7-\delta}$ Bragg reflection shows sharp peaks with ~90° spacing, indicating the presence of only small angle grain boundaries, an essential condition for high-quality electrical properties. These observations suggest that both layers are of high structural quality.

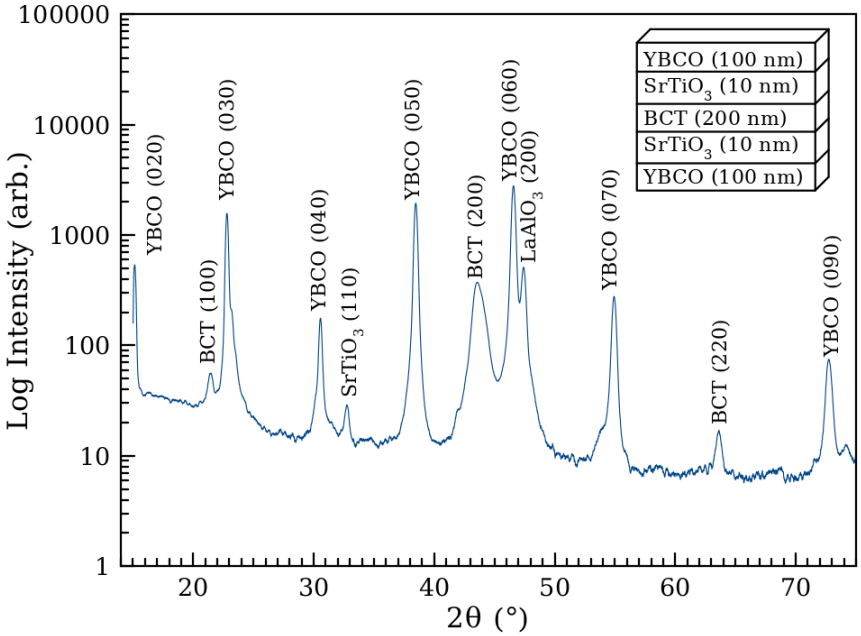

a.)

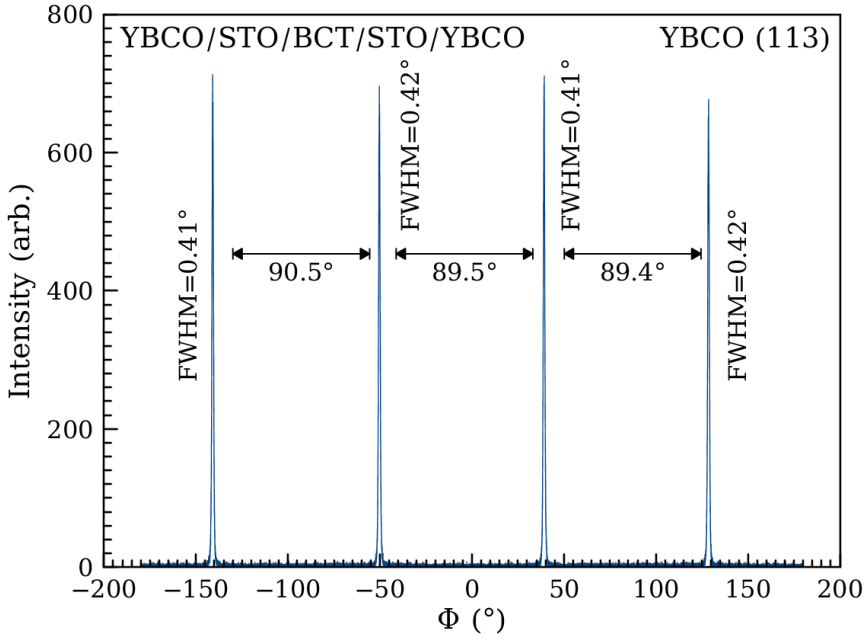

b.)

Figure 31: X-ray diffraction results for $YBa_2Cu_3O_{7-\delta}$ /STO/ $Ba(Cd_{1/3}Ta_{2/3})O_3$ /STO/ $YBa_2Cu_3O_{7-\delta}$ on $LaAlO_3$ substrates structures. (a) shows the θ-2θ out-of-plane scan. Note that the data only show the {010} family of $YBa_2Cu_3O_{7-\delta}$ planes, $Ba(Cd_{1/3}Ta_{2/3})O_3$ {100}, and $Ba(Cd_{1/3}Ta_{2/3})O_3$ (220) orientations. (b) shows the ϕ off-axis scan of the $YBa_2Cu_3O_{7-\delta}$ (113) Bragg peak with peak FWHMs between 0.41° and 0.42° and peak spacings of 90°±0.6°.

Low frequency (1 MHz) capacitance measurements were made to characterize the dielectric properties of the layers. For this experiment, indium electrodes are pressed onto dielectric layers deposited on $SrTiO_3$ (10 nm)/$YBa_2Cu_3O_{7-\delta}$ (200 nm)/$LaAlO_3$ substrates structures. The device is measured as two capacitors in series, i.e., one from first top contact, to the conductive bottom layer, and then other from the conductive bottom layer to the second top contact. For a 400 nm thick $Ba(Cd_{1/3}Ta_{2/3})O_3$ layer and low frequency, 300 pF capacitance is found at room temperature, corresponding to a relative dielectric constant, ε_r, for $Ba(Cd_{1/3}Ta_{2/3})O_3$ of 27.9, slightly lower than the bulk value of 32. For the $Ba(Zn_{1/3}Ta_{2/3})O_3$ 500 nm thick structure, the capacitance is 191 pF, corresponding to a relative dielectric constant of $\varepsilon_r(Ba(Zn_{1/3}Ta_{2/3})O_3)=29.7$, slightly lower than the literature reported bulk value of 30.

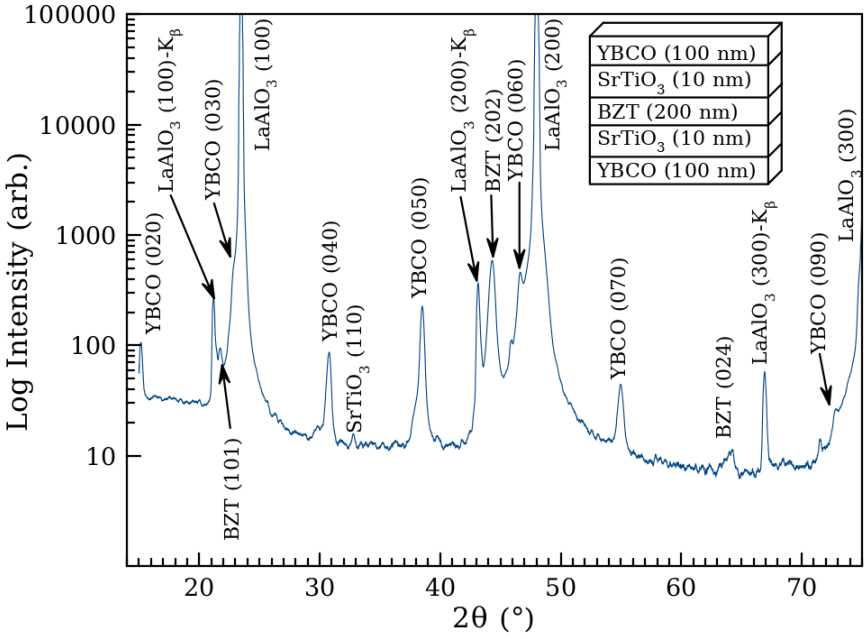

a)

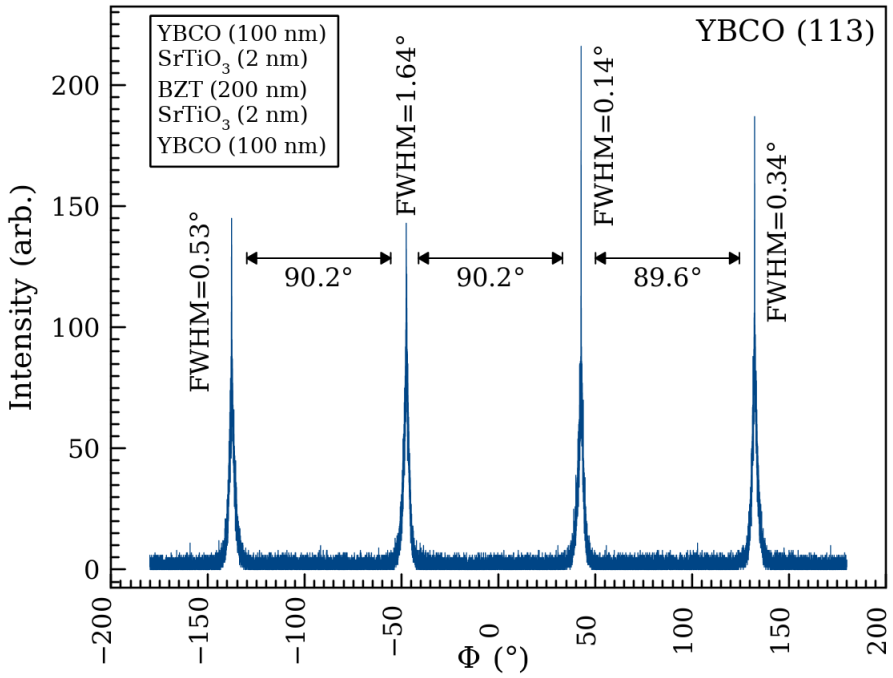

b)

Figure 32 X-ray diffraction of $YBa_2Cu_3O_{7-\delta}/SrTiO_3/Ba(Zn_{1/3}Ta_{2/3})O_3/SrTiO_3/YBa_2Cu_3O_{7-\delta}$ on a $LaAlO_3$ substrate. (a) shows the θ-2θ out-of-plane scan, with only the $YBa_2Cu_3O_{7-\delta}$ {010} family of planes, $Ba(Zn_{1/3}Ta_{2/3})O_3$ {101}, and $Ba(Zn_{1/3}Ta_{2/3})O_3$ (024) orientations. (b) shows the ϕ off-axis scan of the $YBa_2Cu_3O_{7-\delta}$ (113) Bragg peak with peak FWHM between 0.14° and 1.64°, and peak spacing of 90°±0.4°.

6.5 Conclusions

The introduction of $SrTiO_3$ buffer layers enables high-quality tri-layer structures consisting of $YBa_2Cu_3O_{7-\delta}$, electrodes, and either $Ba(Cd_{1/3}Ta_{2/3})O_3$ or $Ba(Zn_{1/3}Ta_{2/3})O_3$ high-κ dielectrics. These structures have single-phase $YBa_2Cu_3O_{7-\delta}$, with (200) textured $Ba(Cd_{1/3}Ta_{2/3})O_3$ and (202) textured $Ba(Zn_{1/3}Ta_{2/3})O_3$. Superconducting transition temperatures measurements performed on the top $YBa_2Cu_3O_{7-\delta}$ layer in a $YBa_2Cu_3O_{7-\delta}$ /buffer/dielectric/buffer/ $YBa_2Cu_3O_{7-\delta}$ structure find that the $YBa_2Cu_3O_{7-\delta}$ film on $Ba(Cd_{1/3}Ta_{2/3})O_3$ has T_{C90}=91.5 K and T_{C10}=89.0 K, while the $YBa_2Cu_3O_{7-\delta}$ film on $Ba(Zn_{1/3}Ta_{2/3})O_3$ structure exhibits a T_{C90}=89.5 K and T_{C10}=87.5 K. Capacitance measurements of the dielectric films find ε_r of $Ba(Cd_{1/3}Ta_{2/3})O_3$ to be 27.9, and ε_r of $Ba(Zn_{1/3}Ta_{2/3})O_3$ to be 29.7; both slightly lower than their stated bulk values.

REFERENCES

1. *Improved superconducting qubit coherence using titanium nitride.* Chang, Josephine B., et al. 1, s.l. : Applied Physics Letters, 2013, Vol. 103. DOI: 10.1063/1.4813269.

2. *Evidence for interacting two-level systems from the 1/f noise of a superconducting resonator.* Burnett, J., et al. s.l. : Nature Communications, 2014, Vol. 5. DOI: 10.1038/ncomms5119.

3. *Two-level states in glasses.* Phillips, W. A. 12, s.l. : Reports on Progress in Physics, 1987, Vol. 50. DOI: 10.1088/0034-4885/50/12/003.

4. *Anomalous low-temperature thermal properties of glasses and spin glasses.* Anderson, P. W., Halperin, B. I. and Varma, C. M. 1, s.l. : The Philosophical Magazine, 1972, Vol. 21. DOI: 10.1080/14786437208229210.

5. *Study of loss in superconducting coplanar waveguide resonators.* Sage, Jeremy M., et al. 6, s.l. : Journal of Applied Physics, Vol. 109. DOI: 10.1063/1.3552890.

6. *Single crystal silicon capacitors with low microwave loss in the single photon regime.* Weber, S. J., et al. 17, s.l. : Applied Physics Letters, 2011, Vol. 98. DOI: 10.1063/1.3583449.

7. *Decoherence in Josephson Qubits from Dielectric Loss.* Martinis, John M., et al. 210503, s.l. : Physical Review Letters, 2005, Vol. 95. DOI: 10.1103/PhysRevLett.95.210503.

8. *Improving the coherence time of superconducting coplanar resonators.* Wang, H., et al. 23, s.l. : Applied Physics Letters, 2009, Vol. 95. DOI: 10.1063/1.3273372.

9. *Surface loss simulations of superconducting coplanar waveguide.* J. Wenner, R. Barends, R. C. Bialczak, Yu Chen, J. Kelly, Erik Lucero, Matteo Mariantoni, A. Megrant, P. J. J. O'Malley, D. Sank, A. Vainsencher, H. Wang, T. C. Whit, Y. Yin, J. Zhao1, A. N. Cleland, John M. Martinis. 113513, s.l. : Applied Physics Letters, 2011, Vol. 99. doi:10.1063/1.3637047.

10. *Determining interface dielectric losses in superconducting coplanar waveguide resonators.* Woods, Wayne, et al. 1, s.l. : Physical Review Applied, 2019, Vol. 12. DOI: 10.1103/PhysRevApplied.12.014012.

11. *Metal-Insulator Transitions.* Mott, N. F. 401-413, s.l. : Contemporary Physics, 1973, Vol. 14:5. doi: 10.1080/00107517308210764.

12. Sebastian, Mailadil T. *Chapter 2: Measurement ofMicrowave Dielectric Properties and Factors Affecting Them.* s.l. : Elsevier, 2008. pp. 11-47. DOI: 10.1016/B978-0-08-045330-9.00002-9.

13. *Intrinsic dielectric loss in crystals: Low temperature.* Gurevic, V. L. and Tagantsev, A. K. 1, Leningrad : Sov. Phys. JETP, 1986, Vol. 64.

14. *In-situ electron paramagnetic resonance studies of paramagnetic point defects in superconducting microwave resonators.* Zhang, Shengke, et al. 122602, s.l. : Applied Physics Letters, 2016, Vol. 109. doi:10.1063/1.4962953.

15. *Defects in irradiated silicon. I. Electron spin resonance of the Si-A center.* Watkins, G. D. and Corbett, J. W. 4, s.l. : Physical Review, 1961, Vol. 121. DOI: 10.1103/PhysRev.121.1001.

16. *EPR of defects in semiconductors: Past, present, future.* Watkins, G. D. 5, s.l. : Physics of the Solid State, 1999, Vol. 41. DOI: 10.1134/1.1130862.

17. *Defects in Irradiated Silicon: Electron Paramagnetic Resonance of the Divacancy.* Watkins, G. D. and Corbett, J. W. 2A, s.l. : Physical Review, 1965, Vol. 138. DOI: 10.1103/PhysRev.138.A543.

18. *Intrinsic Defects in Silicon.* Watkins, G. D. 4, s.l. : Materials Science in Semiconductor Processing, 2000, Vol. 3. DOI: 10.1016/S1369-8001(00)00037-8.

19. Watkins, G. D. Intrinsic Point Defects in Semiconductors. [book auth.] K. A. Jackson and W. Schröter. *Handbook of Semiconductor Technology.* Weinheim : Wiley-VCH, 2000.

20. *Defects in irradiated silicon: Electron Paramagnetic Resonance and Electron-Nuclear Double Resonance of the Si-E center.* Watkins, G. D. and Corbett, J. W. 5, s.l. : Physical Review, 1964, Vol. 134. DOI: 10.1103/PhysRev.121.1001.

21. *Light-induced metastability in pure and hydrogenated amorphous silicon.* Queen, D. R., et al. 2, s.l. : Europhysics Letters, 2015, Vol. 112. DOI: 10.1209/0295-5075/112/26001.

22. Cannelli, G., et al. Tunneling of H and D in Metals and Semiconductors. [ed.] P. Esquinazi. *Tunneling Systems in Amorphous and Crystalline Solids.* Berlin : Springer, 1998.

23. *Energy Levels in Silicon.* Chen, J. W. and Milnes, A. G. 10, s.l. : Annual Review of Materials Science, 1980, Vol. 1. DOI: 10.1146/annurev.ms.10.080180.001105.

24. *Niobium Contamination in Silicon.* Polignano, M. L., et al. 11, s.l. : Electrochemical Society, 2010, ECS Transactions, Vol. 33. DOI: 10.1149/1.3485688 .

25. *Electrical and optical characterization of niobium-related centers in silicon.* Pettersson, H., et al. 1247, s.l. : Semiconductor Science and Technology, 1993, Vol. 8. DOI: 10.1088/0268-1242/8/7/011.

26. *A parallel plate resonator technique for microwave loss measurements on superconductors.* Taber, R. C. 8, s.l. : Review of Scientific Instruments, 1990, Vol. 61. DOI: 10.1063/1.1141389.

27. *Superconducting quantum bits.* Clarke, John and Wilhelm, Frank K. 7198, s.l. : Nature, 2008, Vol. 453. DOI: 10.1038/nature07128.

28. *Initial formation process of metal/silicon interfaces*. Hiraki, Akio. s.l. : Surface Science, 1986. DOI: 10.1016/0039-6028(86)90838-1.

29. Kaufman, L. Nb-Si phase diagram : Coupled phase diagrams and thermochemical data for transition metal binary systems - VI. *ASM Alloy Phase Diagram Database*. s.l. : CALPHAD: Comput. Coupling Phase Diagrams Thermochem., 1979. Diagram No. 906963.

30. *Silicidation of Niobium Deposited on Silicon by Physical Vapor Deposition*. Ndoye, Coumba, et al. 9, 2011, J. Electrochem. Soc., Vol. 158, pp. H897-H90. DOI: http://dx.doi.org/10.1149/1.3609845.

31. *Reactive Nb/Si(111) interfaces studied by electron spectroscopy*. Azizan, M., et al. 10, s.l. : Solid State Communications, 1985, Vol. 54. DOI: 10.1016/0038-1098(85)91165-2.

32. *Material reaction and silicide formation at the refractory metal/silicon interface*. Rubloff, G. W., Tromp, R. M. and van Loenen, E. J. 23, s.l. : Applied Physics Letters, 1986, Vol. 48. DOI: 10.1063/1.96829.

33. *Niobium, indium, and tin heterodiffusion during formation of two-layer systems on silicon single crystals*. Afonin, N. A., et al. 5, s.l. : Russian Journal of Inorganic Chemistry, 2011, Vol. 56. DOI: 10.1134/S0036023611050020.

34. *Vapor pressure data for the solid and liquid elements*. Honig, R. E. s.l. : RCA Review, 1969, RCA Review, Vol. 30, pp. 285-305.

35. *Experimental study of the kinetically-limited decomposition of ZnGeAs2 and its role in determining optimal conditions for thin film growth*. Vahidi, M., et al. 1, s.l. : Journal of Crystal Growth, 2012, Vol. 338. DOI: 10.1016/j.jcrysgro.2011.11.004.

36. Alford, T., Feldman, L. C. and Mayer, J. W. *Fundamentals of Nanoscale Film Analysis*. s.l. : Springer, 2007. p. 14. ISBN: 978-0-387-29260-1.

37. *Investigation of the effect of using verious optics configurations with proportional and position-sensitive detectors*. Kirkham, M. J., Speakman, S. A. and Rawn, C. J. s.l. : Advances in X-ray Analysis, ICDD, 2004, Vol. 47. ISSN 1097-0002.

38. Ziegler, James F. SRIM & TRIM. *Stopping and Range of Ions in Matter*. [Online] http://srim.org/.

39. Schroder, Dieter K. *Semiconductor Material and Device Characterization*. 3rd. s.l. : Wiley, 2006. ISBN: 978-0-471-73906-7.

40. Sze, Simon M. and Ng, Kwok K. *Physics of Semiconductor Devices, 3rd ed*. s.l. : Wiley, 2008. ISBN: 978-0-471-14323-9.

41. *Electrical study of Schottky barriers on atomically clean GaAs(110) surfaces*. Newman, N., et al. 2, s.l. : Physical Review B, 1985, Vol. 33. DOI: 10.1103/PhysRevB.33.1146.

42. *Microwave Dielectric Loss at Single Photon Energies and Millikelvin Temperatures.* Aaron D. O'Connell, M. Ansmann, R. C. Bialczak, M. Hofheinz, N. Katz, Erik Lucero,. 11, s.l. : Applied Physics Letters, 2011, Vol. 92. doi: 10.1063/1.2898887.

43. *UCSB final report for the CSQ program: Review of decoherence and materials physics for superconducting qubits.* Martinis, John M. and Megrant, A. s.l. : arxiv, 2014. eprint arXiv:1410.5793.

44. *Study of loss in superconducting coplanar waveguide resonators.* Sage, Jeremy M., et al. 063915, 2011, J. Appl. Phys., Vol. 109. DOI: http://dx.doi.org/10.1063/1.3552890.

45. *Decoherence in Josephson Phase Qubits from Junction Resonators.* Simmonds, R. W., et al. 7, s.l. : PHYSICAL REVIEW LETTERS, 2004, Vol. 93. DOI: 10.1103/PhysRevLett.93.077003.

46. *Decoherence in Josephson Qubits from Dielectric Loss.* Martinis, John M., et al. 21, s.l. : Physical Review Letters, 2005, Vol. 95. DOI: 10.1103/PhysRevLett.95.210503.

47. *Reducing quantum-regime dielectric loss of silicon nitride for superconducting quantum circuits.* Paik, Hanhee and Osborn, Kevin D. 7, s.l. : Applied Physics Letters, 2010, Vol. 96. DOI:10.1063/1.3309703.

48. *Surface loss simulations of superconducting coplanar waveguide.* Wenner, J., et al. 113513, s.l. : Applied Physics Letters, 2011, Vol. 99. doi:10.1063/1.3637047.

49. Wilkes, John G. Silicon Processing. [book auth.] K. A. Jackson and W. Schroter. *Handbook of Semiconductor Technology: Volume 2.* s.l. : Wiley-VCH, 1999, 1, pp. 46-48.

50. *Microwave Dielectric Loss at Single Photon Energies and Millikelvin Temperatures.* O'Connell, Aaron D., et al. 11, s.l. : Applied Physics Letters, 2008, Vol. 92. doi: 10.1063/1.2898887.

51. Parsey, John M. Jr. Compound Semiconductor Device Processing. [book auth.] K. A. Jackson and W. Schroter. *Handbook of Semiconductor Technology, vol. 2.* s.l. : Wiley-VCH, 2000.

52. *Germanium: From its discovery to SiGe devices.* Haller, E. E. 4, s.l. : Materials Science in Semiconductor Processing, 2006, Vol. 9. 10.1016/j.mssp.2006.08.063.

53. *Reducing intrinsic loss in superconducting resonators by surface treatment and deep etching of silicon substrates.* Bruno, A., et al. 18, s.l. : Applied Physics Letters, 2015, Vol. 106. DOI: 10.1063/1.4919761.

54. *Etch induced microwave losses in titanium nitride superconducting resonators.* Sandberg, Martin, et al. 26, s.l. : Applied Physics Letters, 2012, Vol. 100. DOI: 10.1063/1.4729623.

55. *Preparation of Atomically Clean Surafaces of Si and Ge by Heating in Vacuum.* Jona, F. 10, s.l. : Applied Physics Letters, 1965, Vol. 6. DOI: 10.1063/1.1754133.

56. *An analysis method for asymmetric resonator transmission applied to superconducting devices.* Khalil, M. S., et al. 5, s.l. : Journal of Applied Physics, 2012, Vol. 111. DOI: 10.1063/1.3692073.

57. *Saturation of the dielectric absorption of vitreous silica at low temperatures.* Von Schickfus, M. and Hunklinger, S. 1, s.l. : Physics Letters A, 1977, Vol. 64. DOI: 10.1016/0375-9601(77)90558-8.

58. *Raman scattering in amorphous Ge and III–V compounds.* Wihl, M., Cardona, M. and Tauc, J. s.l. : Journal of Non-Crystalline Solids, 1972, Vols. 8-10. DOI: 10.1016/0022-3093(72)90132-9.

59. *Amorphous Solid without Low Energy Excitations.* Liu, Xiao, et al. 23, s.l. : Physical Review Letters, 1997, Vol. 78. DOI: 10.1103/PhysRevLett.78.4418.

60. *Low-energy excitations in amorphous films of silicon and germanium.* Liu, Xiao and Pohl, R. O. 14, s.l. : Physical Review B, 1998, Vol. 58. DOI: 10.1103/PhysRevB.58.9067.

61. *Hydrogen-Free Amorphous Silicon with No Tunneling States.* Liu, Xiao, et al. 2, s.l. : Physical Review Letters, 2014, Vol. 113. DOI: 10.1103/PhysRevLett.113.025503.

62. *Excess Specific Heat in Evaporated Amorphous Silicon.* Queen, D. R., et al. 13, s.l. : Physical Review Letters, 2013, Vol. 110. DOI: 10.1103/PhysRevLett.110.135901.

63. *High purity isotopically enriched 70Ge and 74Ge single crystals: Isotope separation, growth, and properties.* Itoh, Kohei, et al. 6, s.l. : Journal of Materials Research, 1993, Vol. 8. DOI: 10.1557/JMR.1993.1341.

64. *Ge Films grown on Si substrates by molecular-beam epitaxy below 450 C.* Liu, J., et al. 1, s.l. : Journal of Applied Physics, 2004, Vol. 96. DOI: 10.1063/1.1738530.

65. *UCSB final report for the CSQ program: Review of decoherence and materials physics for superconducting qubits.* Martinis, John M. and Megrant, A. s.l. : arxiv, 2014. eprint arXiv:1410.5793.

66. *Study of loss in superconducting coplanar waveguide resonators.* Jeremy M. Sage, Vladimir Bolkhovsky, William D. Oliver, Benjamin Turek, and Paul B. Welander. 063915, s.l. : Journal of Applied Physics, 2011, Vol. 109. doi: 10.1063/1.3552890.

67. *Calculation of TC in a normal-superconductor bilayer using the microscopic-based Usadel theory.* Martinis, John M., et al. 1-2, s.l. : Nuclear Instruments and Methods in Physics Research Section A: Accelerators, Spectrometers, Detectors and Associated Equipment, 2000, Vol. 444. DOI: 10.1016/S0168-9002(99)01320-0.

68. *Niobium and Tantalum High Q Resonators for Photon Detectors.* Barends, R., et al. 2, s.l. : IEEE Transactions on Applied Superconductivity, 2007, Vol. 17. DOI: 10.1109/TASC.2007.898541.

69. *Comprehensive study of the Raman shifts of strained silicon and germanium.* Peng, C. Y., et al. 8, s.l. : Journal of Applied Physics, 2009, Vol. 105. DOI: 10.1063/1.3110184.

70. *Substrate surface engineering for high-quality silicon/aluminum superconducting resonators*. Earnest, C. T., et al. 12, s.l. : Superconductor Science and Technology, 2018, Vol. 31. DOI: 10.1088/1361-6668/aae548.

71. *Improving the Time Stability of Superconducting Planar Resonators*. Moeed, M. S., et al. 2019. arxiv:1905.00131.

72. *Characterization and reduction of microfabrication-induced decoherence in superconducting quantum circuits*. Quintana, C. M., et al. 6, s.l. : Applied Physics Letters, 2014, Vol. 105. DOI: 10.1063/1.4893297.

73. *The Evolution of Silicon Wafer Cleaning Technology*. Kern, Werner. 6, s.l. : Journal of The Electrochemical Society, 1990, Vol. 137. 10.1149/1.2086825.

74. Wilson, R. G., Stevie, F. A. and Magee, C. W. *Secondary ion mass spectrometry: a practical handbook for depth profiling and bulk impurity analysis*. s.l. : Wiley, 1989. ISBN: 978-0-471-51945-4.

75. *Mechanisms of transition-metal gettering in silicon*. Myers, S. M., Seibt, M. and Schröter, W. 7, s.l. : Journal of Applied Physics, 2000, Vol. 88. DOI: 10.1063/1.1289273.

76. *Improvement of minority carrier diffusion length in Si by Al gettering*. Joshi, Subhash M., Gösele, Ulrich M. and Tan, Teh Y. 8, s.l. : Journal of Applied Physics, 1995, Vol. 77. DOI: 10.1063/1.358563.

77. *The physics of Schottky barriers*. Rhoderick, E. H. 8, s.l. : Journal of Physics D: Applied Physics, 1970, Vol. 3. DOI: 10.1088/0022-3727/3/8/203.

78. *Capacitance Transient Spectroscopy of Trace Contamination in Silicon*. Benton, J. L. 9, s.l. : Journal of The Electrochemical Society, 1982, Vol. 129. DOI: 10.1149/1.2124387.

79. Sze, Simon M. and Ng, Kwok K. *Physics of Semiconductor Devices, 3rd ed*. s.l. : Wiley, 2008. ISBN: 978-0-471-14323-9.

80. *Statistics of the Recombinations of Holes and Electrons*. Shockley, W. and Read, W. T. 5, s.l. : Physical Review, 1952, Vol. 87. DOI: 10.1103/PhysRev.87.835.

81. *Electrical Characteristics of rf-Sputtered Single-Crystal Niobium Films*. Mayadas, A. F., Laibowitz, R. B. and Cuomo, J. J. 3, s.l. : Journal of Applied Physics, 1972, Vol. 43. DOI: 10.1063/1.1661258.

82. *High-Temperature SiO2 Decomposition at the SiO2/Si Interface*. Tromp, R., et al. 21, s.l. : Physical Review Letters, 1985, Vol. 55. DOI: 10.1103/PhysRevLett.55.2332.

83. *Critical-current measurements in epitaxial films of YBa2Cu3O7-x compound*. Chaudhari, P., et al. 25, s.l. : Physical Review Letters, 1987, Vol. 58. DOI: 10.1103/PhysRevLett.58.2684.

84. *Low-temperature critical field of YBCO*. Smith, J. L., et al. 2, s.l. : Journal of Superconductivity, 1994, Vol. 7. DOI:10.1007/BF00724550.

85. *YBa2Cu3O7–δ superconducting films with low microwave surface resistance over large areas*. Newman, N., et al. 5, s.l. : Applied Physics Letters, 1990, Vol. 57. 10.1063/1.104244.

86. *Resistive loss at 10 GHz in c-axis-aligned in-situ-grown YBa2Cu3O7 films*. Laderman, S. S., et al. 4, s.l. : Physical Review B, 1991, Vol. 43. DOI:10.1103/PhysRevB.43.2922.

87. *Orientation Dependence of Grain-Boundary Critical Currents in YBa2Cu3O7-δBicrystals*. Dimos, D., et al. 2, s.l. : Physical Review Letters, 1988, Vol. 61. 10.1103/PhysRevLett.61.219.

88. *Large-area YBa2Cu3O7–δ thin films on sapphire for microwave applications*. Cole, B. F., et al. 14, s.l. : Applied Physics Leters, 1992, Vol. 61. DOI:10.1063/1.108411.

89. *Microwave surface resistance of epitaxial YBa2Cu3O7 thin films on sapphire*. Char, K., et al. 4, s.l. : Applied Physics Letters, 1990, Vol. 57. DOI: 10.1063/1.103651.

90. *High critical current densities in epitaxial YBa2Cu3O7–δ thin films on silicon-on-sapphire*. Fork, D. K., et al. 21, s.l. : Applied Physics Letters, 1991, Vol. 58. DOI:10.1063/1.104864.

91. *Recent progress on the dielectric properties of dielectric resonator materials with their applications from microwave to optical frequencies*. Higuchi, Yukio and Tamura, Hiroshi. 14, s.l. : Journal of the European Ceramic Society, 2003, Vol. 23. DOI:10.1016/S0955-2219(03)00193-6.

92. *Microwave Dielectric Ceramics for Resonators and Filters in Mobile Phone Networks*. Reaney, Ian M. and Iddles, David. 7, s.l. : Journal of the American Ceramic Society, 2006, Vol. 89. DOI: 10.1111/j.1551-2916.2006.01025.x.

93. *Epitaxial bilayers and trilayers of superconducting and high K materials grown by PLD for microwave applications*. Delange, T., et al. s.l. : Thin Solid Films, 2004, Vols. 453-454, pp. 273-278. DOI: 10.1016/j.tsf.2003.11.283.

94. *High-temperature superconducting microwave devices: Fundamental issues in materials, physics, and engineering*. N. Newman, W. G. Lyons. 3, s.l. : Journal of Superconductivity, 1993, Vol. 6, pp. 119–160. DOI: 10.1007/BF00625741.

95. *Growth and characterization of Ba(Cd1/3Ta2/3)O3 thin films*. L.T.Liu, Cameron Kopas, R.K.Singh, R.M.Hanley, N.Newman. 19, s.l. : Thin Solid Films, 2012, Vol. 520. DOI: 10.1016/j.tsf.2012.06.034.

96. *Growth and characterization of epitaxial Ba(Zn1/3Ta2/3)O3 (100) thin films*. Tang, Z. Z., et al. 2, s.l. : Acta Materialia, 2009, Vol. 57. DOI: 10.1016/j.actamat.2008.09.038.

97. Newman, Nathan and Char, Kookrin. *Substrate heater utilizing protective heat sinking means*. *US5126533A* US, 1990.

98. *Anisotropic transport properties of in-plane-aligned a-axis YBa2Cu3O7 films*. Suzuki, Y., et al. 14, s.l. : Phys. Rev. B., 1993, Vol. 48. DOI: 10.1103/PhysRevB.48.10642.

99. PDF 00-017-0175. Newtown Square, PA : ICDD, 2015.

100. PDF 01-070-0197. Newtown Square, PA : ICDD, 2015.

101. *Niobium, indium, and tin heterodiffusion during formation of two-layer systems on silicon single crystals*. Afonin, N. A., et al. 5, s.l. : Russian Journal of Inorganic Chemistry, 2011, Vol. 56. DOI: 10.1134/S0036023611050020.

102. *X-ray diffraction topography for materials science*. Shul'pina, I. L. and Prokhorov, I. A. 5, s.l. : Crystallography Reports, 2012, Vol. 57. 10.1134/S106377451205015X.

103. Culbertson, Robert J. and Wilkens, Barry J. *Short Course on Ion Beam Analysis*. Tempe, AZ : IBeAM, LeRoy Eyring center for Solid State Science, 2011.

APPENDIX A

SIGNATURE PAGE

Synthesis, Characterization, and Optimization
of Superconductor-Dielectric Interfaces
by

Cameron Kopas

A Dissertation Presented in Partial Fulfillment
of the Requirements for the Degree
Doctor of Philosophy

ARIZONA STATE UNIVERSITY

Graduate Supervisory Committee:

Nathan Newman, Ph.D., Chair

Terry Alford, Ph.D.

Ray Carpenter, Ph.D.

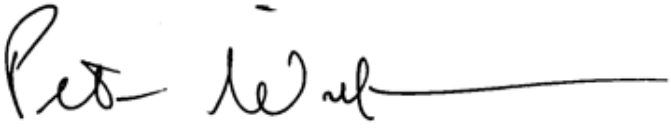

Peter Williams, Ph.D.

Approved April 2020